# Developing High-Efficiency Ternary Thermoelectric Phosphides in the Systems Ca-Ag-P and Ca-Cu-P

by

Melis Aktürk Aktaş

A Dissertation Submitted to the
Graduate School of Sciences and Engineering
in Partial Fulfillment of the Requirements for
the Degree of

Master of Science

in

Materials Science and Engineering


July, 2024

# Developing High-Efficiency Ternary Thermoelectric Phosphides in the Systems Ca-Ag-P and Ca-Cu-P

Koç University

Graduate School of Sciences and Engineering

This is to certify that I have examined this copy of a master's thesis by

**Melis Aktürk Aktaş**

and have found that it is complete and satisfactory in all respects,
and that any and all revisions required by the final
examining committee have been made.

Committee Members:

---

Assoc. Prof. Umut Aydemir (Advisor)

---

Assoc. Prof. Uğur Ünal

---

Assoc. Prof. Hyun-Sik Kim

Date: 08.07.2024

*To my lovely family…*

# ABSTRACT


**Developing High-Efficiency Ternary Thermoelectric Phosphides in the Systems Ca-Ag-P and Ca-Cu-P**

**Melis Aktürk Aktaş**

**Master of Science in Materials Science and Engineering**

**July , 2024**

Since the discovery of the thermoelectric (TE) effect by Seebeck, Peltier, and Thomson in the XIX$^{th}$ century, thermoelectricity has attracted significant attention for both fundamental science and industrial applications. Nowadays, this interest has been rejuvenated by the ever-growing worldwide energy demand and the concomitant environmental concerns tied to the emission of pernicious greenhouse gases. Among renewable energy sources, thermoelectricity stands out for not only waste-heat harvesting but also for being replaced by commercial refrigerators. Considering that about two-thirds of the energy produced is lost as waste heat, this versatile technology is quite useful as it converts heat into electricity and vice-versa. The thermoelectric efficiency of a given material is quantified through the dimensionless thermoelectric figure of merit, zT, defined as $zT = \alpha^2\sigma T/(\kappa_l + \kappa_e)$ where α, σ, $\kappa_l$, $\kappa_e$ and T correspond to the Seebeck coefficient, electrical conductivity, lattice thermal conductivity, electronic thermal conductivity, and temperature, respectively. The higher the zT value at a given temperature, the higher the thermoelectric efficiency of the module. The challenge to overcome in thermoelectricity is thus clearly material: a good thermoelectric material should possess low electrical resistivity to minimize heat losses through Joule effect, high thermopower to maximize the thermoelectric effect, and low thermal conductivity to maintain a temperature gradient large enough between either side of the thermocouple. Ternary phosphides (CaAgP and CaCuP) are stable and can exhibit promising thermoelectric properties. To date, these materials have remained largely unexplored, but recent theoretical studies demonstrate their high predicted thermoelectric efficiencies.

In this thesis study, the electrical and thermal transport properties of p-type CaAgP and CaCuP materials were investigated through Zn, Na, Sn, nano-boron (nB), and La doping. CaAgP and CaCuP powders have been synthesized by high-energy ball milling and were sintered by spark plasma sintering technique. The dopants were introduced to the materials by applying the same synthesis processes. Additionally, annealing procedures were performed on certain samples following the sintering process. Detailed chemical characterization of these polycrystalline materials has been carried out. Thermoelectric examinations of the materials obtained in the desired purity and composition have been completed. The mechanical properties of thermoelectrically promising samples were measured. The measurements of the dielectric constant of CaAgP and CaCuP, and thermoelectric modeling were also conducted by the Korean partner.

The intrinsically doped $CaAg_{0.90}P$ sample achieved the highest zT value of approximately 0.33 at 823 K, with additional dopants failing to further enhance zT values in the CaAgP compound. Notably, the sample doped with 0.05 at.% nano boron demonstrated the maximum hardness within the Ca-Ag-P system. In the CaCuP system, the zT value improved significantly, increasing from 0.37 to 0.45 at 823 K for the Zn-doped and annealed $Ca_{1.05}Cu_{0.95}P$-$Zn_{0.05}$ sample. Additionally, the inclusion of nano boron and zinc not only enhanced zT values but also improved the mechanical properties of the CaCuP and $CaAg_{0.90}P$ microstructures. These findings underscore the importance of detailed experimental and computational studies on ternary phosphides, which can substantially contribute to the development of new thermoelectric materials and their applications.

# ÖZETÇE


**Ca-Ag-P ve Ca-Cu-P Sistemlerinde Yüksek Verimli Üçlü Termoelektrik Fosfitlerin Geliştirilmesi**

**Melis Aktürk Aktaş**

**Malzeme Bilimi ve Mühendisliği, Yüksek Lisans**

**Temmuz, 2024**

XIX. yüzyılda Seebeck, Peltier ve Thomson tarafından termoelektrik (TE) etkisinin keşfedilmesinden bu yana, termoelektrik hem temel bilim hem de endüstriyel nedenlerden dolayı büyük ilgi görmüştür. Günümüzde bu ilgi, dünya çapında giderek artan enerji talebi ve buna eşlik eden, zararlı sera gazlarının emisyonuna bağlı çevresel kaygılar nedeniyle yeniden canlanmıştır. Yenilenebilir enerji kaynakları arasında termoelektrik, yalnızca atık ısının toplanmasıyla değil, aynı zamanda ticari buzdolapların yerini almasıyla da öne çıkıyor. Üretilen enerjinin yaklaşık üçte ikisinin atık ısı olarak kaybolduğu göz önüne alındığında, bu çok yönlü teknoloji, ısıyı elektriğe veya elektriği ısıya dönüştürdüğü için oldukça kullanışlıdır. Belirli bir malzemenin termoelektrik verimliliği, α, σ, κl, κe ve T'nin Seebeck katsayısına, elektriksel iletkenliğe, kafes termal iletkenliğine, elektronik termal iletkenliğe ve sıcaklığa karşılık geldiği $zT = \alpha^2\sigma T/(\kappa_l + \kappa_e)$ olarak tanımlanan boyutsuz termoelektrik değer $zT$ aracılığıyla ölçülür. Belirli bir sıcaklıkta zT değeri ne kadar yüksek olursa modülün termoelektrik verimliliği de o kadar yüksek olur. Dolayısıyla termoelektrikte aşılması gereken zorluk açıkça malzemedir: iyi bir termoelektrik malzeme, Joule etkisi yoluyla ısı kayıplarını en aza indirmek için düşük elektrik direncine, termoelektrik etkiyi maksimuma çıkarmak için yüksek termo güce ve termokapılın her iki taraf arasında yeterince büyük bir sıcaklık gradyanını korumak için düşük termal iletkenliğe sahip olmalıdır. Üçlü fosfitler (CaAgP ve CaCuP) stabildir ve umut verici termoelektrik özellikler sergileyebilir. Bugüne kadar bu malzemeler büyük ölçüde keşfedilmemiştir, ancak son teorik çalışmalar bunların yüksek termoelektrik verimlilikleri olabileceğini ortaya koymaktadır.

Bu tez çalışmasında, p-tipi CaAgP ve CaCuP malzemelerin elektriksel ve termal taşınım özellikleri Zn, Na, Sn, nano-bor (nB) ve La katkılaması yoluyla araştırılmıştır. CaAgP ve CaCuP tozları yüksek enerjili bilyalı öğütme yoluyla sentezlenmiş ve kıvılcım plazma sinterleme tekniği ile sinterlenmiştir. Katkı maddeleri aynı sentez işlemleri uygulanarak malzemelere dahil edilmiştir. Ayrıca sinterleme işleminin ardından belirli numunelere tavlama işlemleri de yapılmıştır. Bu çok kristalli malzemelerin detaylı kimyasal karakterizasyonu gerçekleştirilmiştir. İstenilen saflık ve bileşimde elde edilen malzemelerin termoelektrik incelemeleri tamamlanmıştır. Termoelektrik açıdan umut vaat eden numunelerin mekanik özellikleri ölçülmüştür. CaAgP ve CaCuP'nin dielektrik sabitinin ölçümleri ve termoelektrik modelleme de Kore'de ki çalışma partnerlerimiz tarafından gerçekleştirildi.

Kendinden katkılı $CaAg_{0.90}P$ numunesi, 823 K'de yaklaşık 0,33'lük en yüksek zT değerine ulaşmıştır; ilave katkılama deneyleri CaAgP bileşiğindeki zT değerlerini daha da arttırmakta başarısız olmuştur. Dikkat çekici bir şekilde, %0.05 atomik nano bor katkılı

numune, Ca-Ag-P sistemi içindeki maksimum sertliği göstermiştir. CaCuP sisteminde zT değeri önemli ölçüde iyileşmiş ve Zn katkılı ve tavlanmış $Ca_{1.05}Cu_{0.95}P$-$Zn_{0.05}$ malzemesi için zT, 823 K'de 0,37'den 0,45'e yükselmiştir. Ek olarak, nano bor ve çinkonun dahil edilmesi yalnızca zT değerlerini arttırmakla kalmamış, aynı zamanda CaCuP ve $CaAg_{0.90}P$ mikro yapılarının mekanik özelliklerini de geliştirmiştir. Bu bulgular, yeni termoelektrik malzemelerin geliştirilmesi ve uygulamalarına önemli ölçüde katkıda bulunacak üçlü fosfitler üzerinde ayrıntılı deneysel ve hesaplamalı çalışmaların önemini vurgulamaktadır.

# ACKNOWLEDGMENTS

I would like to express my gratitude to everyone who has supported, motivated, and believed in me during my academic studies. I would like to express my appreciation for the financial assistance provided by TÜBİTAK under grant number 221N045.

Firstly, I would like to thank my advisor, Assoc. Prof. Umut Aydemir for his guidance and support during my studies. This master's degree and thesis work would not have been possible without his leadership.

I would also like to thank Assoc. Prof. Dr. Uğur Ünal for being my thesis committee member and for his valuable comments. I express my sincere gratitude to Dr. Barış Yağcı for their significant help and guidance during the SEM processes.

I would like to express my sincere appreciation to all my group members and friends at Koç University Boron and Advanced Materials Application and Research Center (KUBAM) for their valuable contributions and support during the research process, which brought me great satisfaction. Special thanks to İlayda Terzi and Müjde Yahyaoğlu, who patiently and devotedly shared all their knowledge about thermoelectric materials with me, also my thanks go to Tuğser Yılmaz, Saba Sepahban Shahgoli, and Verda Berşan Genceli who always kindly helped me when I asked for their support during my experiments.

I want to thank Prof Hyun-Sik Kim for allowing me to visit the University of Seoul and supporting me in using such advanced research facilities. I would also like to thank graduate student Minsu Heo, who provided his support in SPB calculations and contributed to the completion of my thesis. Their hospitality and generosity have left me with unforgettable memories during my time in South Korea.

Last but not least, I would like to express my appreciation to Filiz and Tayfun Aktürk, my parents, for their continuous encouragement and unconditional love during my studies and my whole life.

Finally, I will always be grateful to Alican, my life partner, for his unending love, patience, and support.

# TABLE OF CONTENTS

# LIST OF TABLES

# LIST OF FIGURES

# ABBREVIATIONS

| | |
|---|---|
| B | Thermoelectric Quality Factor |
| DOS | Density of States |
| EDX | Energy Dispersive X-Ray Spectroscophy |
| HV | Hardness Value |
| LFA | Laser Flash Analysis |
| PF | Power Factor |
| TE | Thermoelectric |
| SPB | Single Parabolic Band |
| SEM | Scanning Electron Microscopy |
| SPS | Spark Plasma Sintering |
| VBM | Valence Band Maximum |
| XRD | X-Ray Diffraction |
| zT | Thermoelectric Figure of Merit |

# Chapter 1:
# INTRODUCTION

Every day, the negative effects of the climate crisis on human life and all living beings grow more dangerous. Some of the answers to global environmental challenges include reducing fossil fuel consumption and greenhouse gas emissions, mitigating ozone depletion, and providing clean energy. The solution to the current energy dilemma rests on a concerted effort to broaden our renewable energy resources (wind, biomass, geothermal, solar PV, solar thermal, etc.) and increase our energy efficiency. Since almost two-thirds of the energy consumed worldwide is lost as waste heat, recovering even a small fraction of this lost energy would significantly impact global energy use [1].

Several research studies have revealed that a significant proportion, approximately 70%, of energy is lost as heat during industrial processes on an annual basis [2]. As a result, considerable effort has been invested in enhancing the performance of renewable energy sources such as solar, wind, and naturally abundant hydropower. Recovering energy from industrial waste heat is another sustainable method for meeting future energy demands [3]. Thermoelectric technology is the only sustainable method that directly turns waste heat into electricity [4]. Thermoelectrics provide a simple and environmentally favorable option for direct heat to electricity conversion. The application of electrical current to a temperature gradient between two ends of the TE material produces power, while the application of a temperature gradient between two ends of the TE material produces cooling or heating [5].

Figure 1.1 illustrates the potential waste heat capacity of several industrial processes as a function of temperature. By analyzing the distribution of waste heat capacity, it is evident that waste heat occurs over a wide range of temperatures, ranging from 100°C to 1000°C [6]. Consequently, each needs various recovery systems that generate a specific quantity of energy based on the operational temperature. Thermoelectric technology allows for the efficient utilization of waste heat at different temperatures through alternative thermoelectric materials.

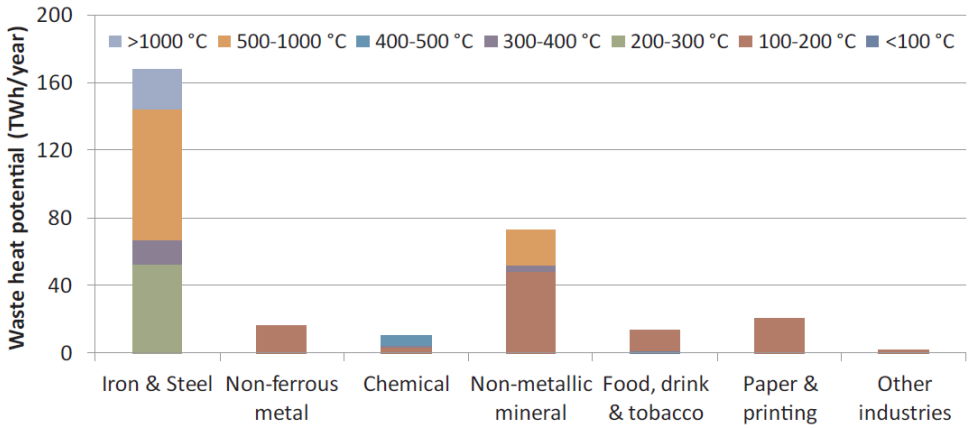


Figure 1.1: Waste heat potential for the industrial sector and temperature level [6].

Figure 1.2 illustrates the numerous types of thermoelectric materials available in thermoelectric technology, specifically n-type and p-type, which are suitable for different temperature ranges. Hence, an appropriate thermoelectric material can be chosen based on the processes by which waste heat is generated and emitted.

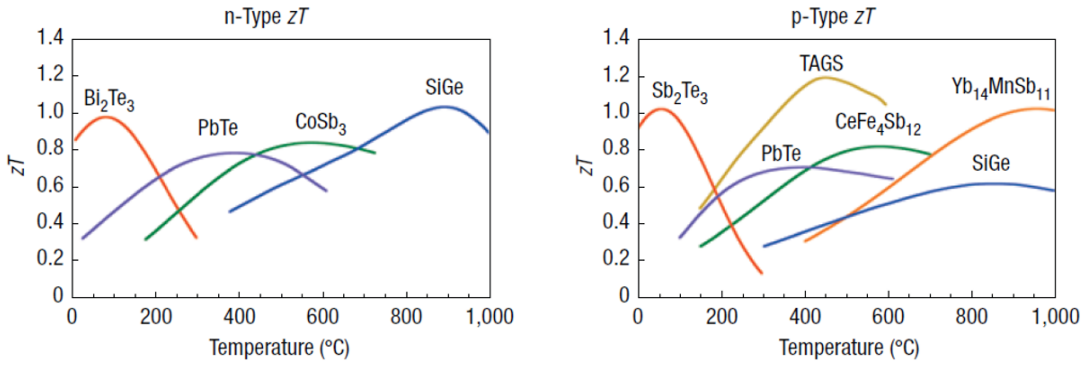


Figure 1.2: The zT figure of merit for both the p-type and n-type materials utilized in a certain temperature range [7].

The most suitable thermoelectric (TE) materials utilized in devices have a zT value of 1. Thermoelectric materials such as PbTe, $Bi_2Te_3$, $CoSb_3$, and Si-based alloys are suitable for achieving this specific zT value. The majority of them exhibit optimal performance at low and intermediate operating temperatures. However, they are not suitable for waste heat recovery applications because of having several disadvantages such as degradation and breakdown at temperatures above 500–600 C, thermal and/or chemical instability, expensive, poisonous, and/or scarce ingredients. Their usage is limited in some applications [8].

This thesis will evaluate promising ternary phosphides thermoelectric material with promising zT values at medium-to-high temperature range corresponding to 500-600°C. The first chapter will focus on general thermoelectric theory and then a review of the literature on thermoelectric ternary phosphide, CaCuP, and CaAgP-based materials. The following chapters will describe experimental methods and characterization techniques in depth. Then, the sections that follow will clarify the main results and discussions relating to these studies. A conclusion section will be included at the end summarizing my research results.

# Chapter 2:
# THERMOELECTRIC THEORY AND LITERATURE REVIEW

The increasing demand for energy and human consumption behaviors have generated interest in alternative energy sources and innovative technologies that may improve the energy efficiency of traditional fuel combustion methods. In this situation, thermoelectricity presents as a feasible alternative with a positive outlook, since it combines a renewable energy source with the potential to enhance global energy efficiency. Thermoelectricity is the generation of electrical energy by applying a temperature difference between two sides of a material. Conversely, it may also include the generation of a temperature differential between a material by conducting an electric current through it. These properties are crucial in the operation of energy generation or cooling systems that do not involve the burning of fuel or the use of moving parts [1].

## *2.1 Thermoelectric Effects*

The Seebeck effect, Peltier effect, and Thomson effect are three significant transport phenomena that were identified over 150 years ago and are the basis of thermoelectricity. The early stage of the thermoelectric effect, which involves the conversion of heat into electricity, was first observed in 1821 by Thomas Johann Seebeck, a scientist from Estonia. This phenomenon was further investigated by Jean Peltier, a physicist from France, and is known as the Peltier-Seebeck effect. The Seebeck effect may convert heat directly to electricity, whereas the Peltier effect can be used for thermoelectric (TE) cooling. Both effects require a connection between two different materials: n-type (electrons) and p-type semiconductors (holes) [9].

The occurrence of a temperature difference between two locations in a conductor or semiconductor results in the generation of a voltage difference. In other words, a temperature gradient in a conductor or semiconductor enables an electric field to occur. The Seebeck effect is the name of this phenomenon. The Seebeck coefficient ($\alpha$) value, often known as thermopower, is the thermoelectric voltage generated per unit temperature difference ($\Delta V/\Delta T$ )in a conductor [10]. Figure 2.1 can be useful in explaining the movement of the carriers and the developed electric field related to the Seebeck effect.

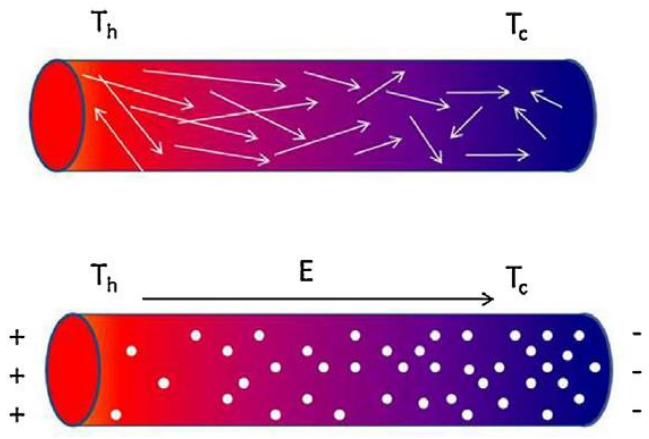


Figure 2.1: Electrons, which are negatively charged carriers, move from the hot side ($T_h$) to the cold side ($T_c$) as a result of the temperature difference, producing an electric field [11].

Figure 2.1 indicates that the electrons on the hot side ($T_h$) of the compound, which have higher energy, exhibit a longer mean free path (shown by longer arrows) compared to the electrons on the cool side ($T_c$). Following that, the higher-energy electrons (shown as white dots) move towards the colder side, so altering the charge distribution on the material. The change in charge distribution on the material results in a potential difference. An electric field (E) is formed to prevent more diffusion as a result of the presence of potential difference [11].

The Peltier effect is another fundamental thermoelectric principle. This phenomenon explains that when an electrical current flows through the junction of two dissimilar materials, heat is created or absorbed, depending on the direction of the current. The cause of this effect is related to the difference in the Fermi energy of the two materials [12].

To understand the inverse correlation between the Seebeck and Peltier effects, it is helpful to analyze them together, as represented in Figure 2.2. The thermoelectric theory is implemented for heat recovery and cooling purposes by using thermoelectric devices, which can operate in either energy generation (Fig. 2.2a) or cooling (Fig. 2.2b) mode. The first figure displays a current that happens when the two sides of a TE couple are subjected to a temperature gradient. The second image indicates what happens when a voltage is given to a TE couple and charge carriers preserve the electrical balance by absorbing thermal energy at one end. Materials with significant thermoelectric (TE)

characteristics are becoming increasingly attractive because of these two phenomena [11].

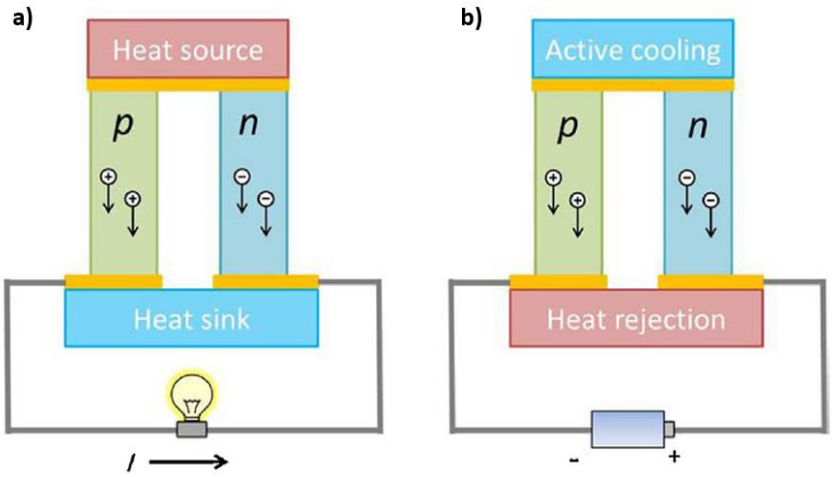


Figure 2.2: Schematic diagrams of thermoelectric modules; a) Seebeck effect, where a temperature difference provided to the material allows charge carriers (either electrons or holes) to disperse from the hotter side to the colder side, b) Peltier effect, when a current flows through the circuit, heat is absorbed at the top junction and discharged at the lower junction [11].

## *2.2 Dimensionless Figure of Merit*

Altenkirch developed the thermoelectric efficiency, often known as the thermoelectric figure of merit, in 1911. The conversion efficiency of thermoelectric materials is calculated using the dimensionless figure of merit formula, represented as zT [10]. The equation is defined by

$$zT = \frac{\alpha^2 \sigma T}{\kappa} \tag{2.1}$$

where $\alpha$ the Seebeck coefficient, σ the electrical conductivity, T is the temperature, and κ the thermal conductivity. The thermal conductivity, defined by the symbol $\kappa$, can be examined in two different types: lattice thermal conductivity ($\kappa_{lat}$) and electronic thermal conductivity ($\kappa_e$). To obtain a high figure of merit value, the Seebeck coefficient and electrical conductivity should achieve maximum values, while the thermal conductivity should reach a minimum value, following the relationship in the equation. ZT optimization is quite complex because of the interdependent coefficients (α, σ, κ). The electronic and phonon transport processes affect the variables that control ZT. The power

factor ($\alpha^2\sigma$) on the ZT equation is related to the electronic transport. Nevertheless, due to two transport parameters, α and σ have opposing trends as a mechanism of carrier concentration, obtaining high α and σ simultaneously is difficult. High carrier densities are required for big electrical conductivity, whereas low carrier densities are necessary for large Seebeck coefficients. The relation between these parameters is indicated in Figure 2.3 [7].

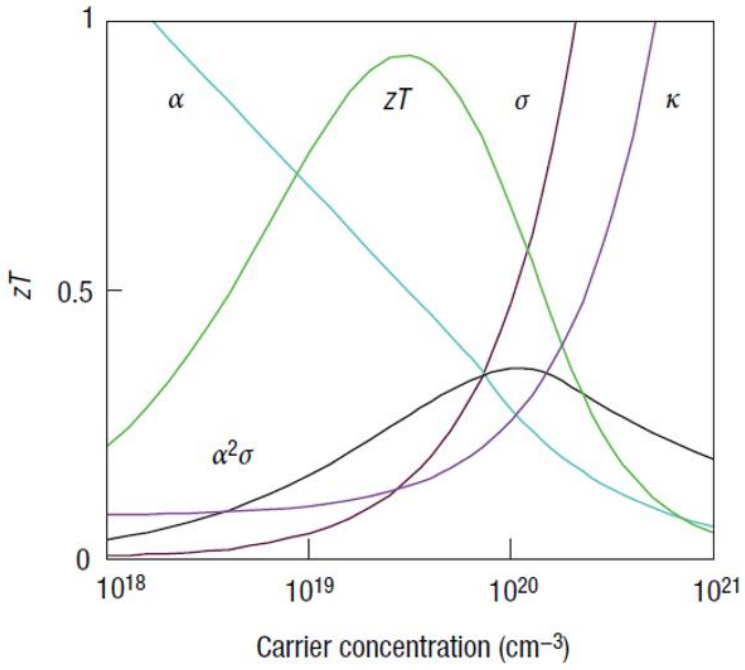


Figure 2.3: The relation between ZT, Seebeck coefficient (α), thermal conductivity (κ) with electrical conductivity (σ) [7].

In another case, a high TE figure of merit necessitates the lowest feasible heat conductivity, and increasing the electrical conductivity (σ) implies the enhancement on electronic thermal conductivity ($\kappa_e$). The relationship between these parameters is defined according to the Wiedemann-Franz law, as indicated below;

$$\kappa_e = L\sigma T \tag{2.2}$$

where L is the Lorenz number and its value is 2.44 x $10^{-8}$ W.σ/$K^2$ (degenerate limit). The Wiedemann-Franz law indicates that the electronic thermal conductivity ($\kappa_e$) is directly proportional to the electrical conductivity [9].

Carrier concentration affects both the Seebeck coefficient and the electrical conductivity. According to Figure 2.4, when electrical conductivity increases, the Seebeck coefficient decreases with carrier concentration. In low-carrier concentration semiconductors or insulator materials, a high Seebeck coefficient is necessary for getting a high ZT value. Also, for high carrier concentration metals, high electrical conductivity should exist to reach a high ZT value. As seen in Figure 2.4 the thermoelectric power factor ($\alpha^2\sigma$) has a peak value between carrier concentrations of semiconductors and metals. As a result, the development of high-performance materials needs the control of three variables that are difficult to manage individually. Thus, the attention of thermoelectric material research is also on narrow bandgap semiconductors with charge-carrier densities in $10^{19}$-$10^{21}$ $cm^{-3}$ to achieve good thermoelectric materials. Hence, heavily doped semiconducting materials are preferred over metals and insulating materials for thermoelectric applications [13].

There are some approaches to improve the ZT value of thermoelectric materials. The first one that decreasing the lattice thermal conductivity via alloy scattering or rattling atoms. The other one is the nanostructuring of thermoelectric materials, implying that nanoscale or nanostructured morphologies can also be used to develop ZT [13][14].

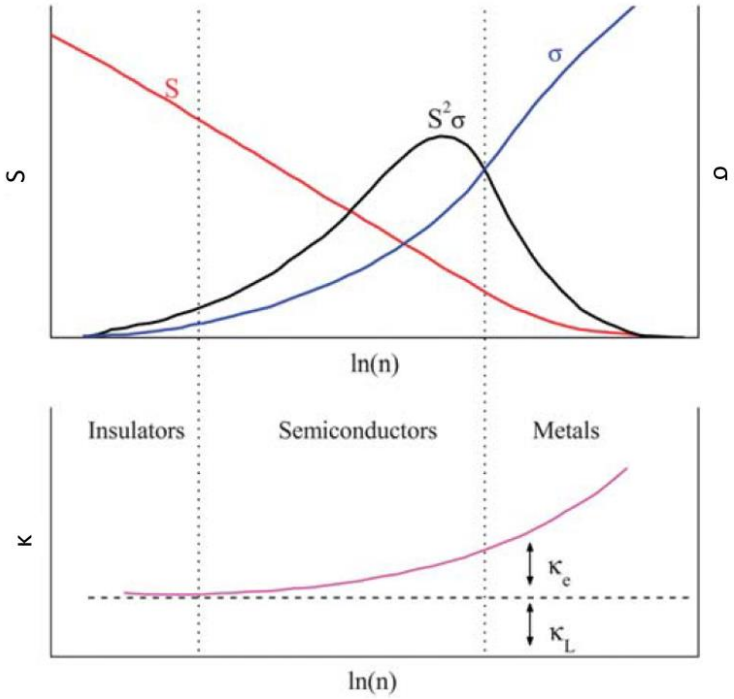


Figure 2.4: Relation of the Seebeck coefficient (S), electrical conductivity (σ), and electronic ($\kappa_e$) and lattice ($\kappa_L$) effects to thermal conductivity with the charge carrier concentration n [14].

## *2.3 Thermoelectric Device and Efficiencies*

In a conventional thermoelectric device, a junction is comprised of two different conducting materials that involve positive charge carriers, such as holes, and negative charge carriers, such as electrons. Charges, both positive and negative move away from the junction and convey heat while an electric current is sent across the junction. This leads to cooling the junction. On the other hand, existing the heat source at the junction drives that carrier to flow away from the junction, producing an electrical generator [15].

When an n-type doped material is electrically linked in series and thermally linked in parallel to a p-type doped material throughout a temperature differential, current flows between the two materials, generating a thermoelectric device. The development of a thermoelectric device begins with a thermoelectric couple, which is made up of n- and p-type materials. In Figure 2.5(a), an example of the thermoelectric couple can be seen clearly. A thermoelectric module is formed when multiple couplings are joined electrically in series and thermally in parallel, indicated as in Figure 2.5(b). A

thermoelectric generator is made up of many modules connected by heat exchangers to a heat source and a heat sink, as shown in Figure 2.5(c) [16].

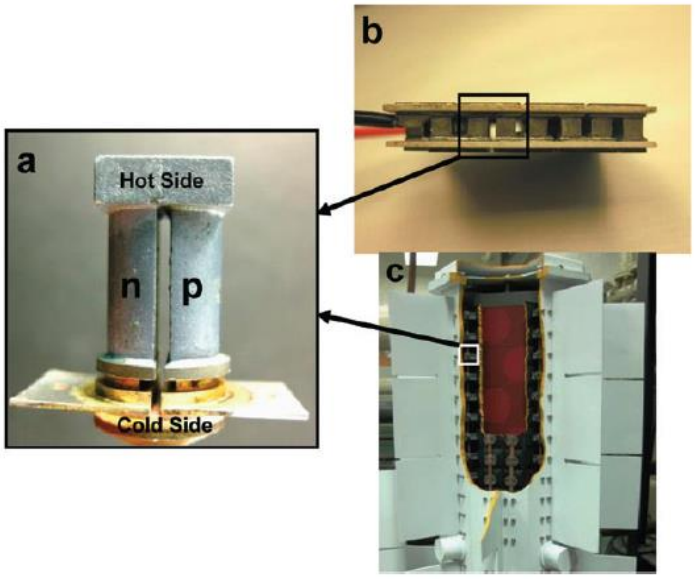


Figure 2.5: Example of (a) a typical thermoelectric couple, (b) a thermoelectric module, and (c) a thermoelectric generator [16].

The efficiency of thermoelectric materials mostly relies on the zT and thermoelectric quality factor. The formula for the maximum efficiency of TE power generation, represented as η, is as follows:

$$\eta_{max} = \frac{T_{Hot}-T_{cold}}{T_{Hot}} \cdot \frac{\sqrt{1+ZT_m}-1}{\sqrt{1+ZT_m}+T_C/T_h} \tag{2.3}$$

The expression ($T_H$–$T_C$/$T_H$) refers to the Carnot efficiency, while $ZT_m$ represents the average ZT value between the hot and cold temperatures [17]. The Carnot efficiency refers to the highest possible efficiency that a device can achieve, according to theoretical limits. However, most TE devices are limited to a conversion efficiency of 10% relative to the maximum Carnot efficiency [18].

Furthermore, the maximum value of the figure of merit for a specific material, assuming the carrier concentration n is properly optimized, relies on its thermoelectric quality factor, B, in the following approach;

$$B = \left(\frac{k_B}{e}\right)^2 \cdot \frac{8\pi e(2m_e k_B)^{3/2}}{h^3} \cdot \frac{\mu_W T^{5/2}}{\kappa_{lat}} \tag{2.4}$$

$k_B$, e, $m_e$, $\mu_w$, h, and $\kappa_{lat}$ represent the Boltzmann constant, electron charge, free electron mass, weighted mobility, Planck's constant, and lattice thermal conductivity, respectively. This equation indicates that B can be evaluated based on two parameters. The first parameter refers to the electronic characteristics of materials, specifically the $\mu_w$ value. The second parameter regards the thermal properties of materials, specifically the $\kappa_{lat}$ value. The quality factor, *B*, is also expressed in a simplified form as $B = \frac{B_E.T}{\kappa_{lat}}$, where $B_E$ represents the electrical quality factor. The independence of $B_E$ from temperature and doping allows a change in its value concerning temperature to indicate band convergence, additional charge scattering, and bipolar conduction [19]. Both values *B* and $B_E$ have an important effect on describing the highest zT value of a material of interest. The weighted mobility, $\mu_w$, is a function that is defined in an obvious way using the Seebeck coefficient and electrical conductivity. It provides information about the electronic structure and scattering mechanisms within materials. The thermoelectric quality factor (*B*), directly proportional to the ratio of weighted mobility ($\mu_w$) to lattice thermal conductivity ($\kappa_L$), determines the highest figure of merit (zT) that an ideally doped material may achieve. Therefore, any approach aimed at enhancing the thermoelectric properties of a material by reducing its thermal conductivity ($\kappa_L$) must also consider the impact on $\mu_w$ [20, 21].

Figure 2.6 illustrates the power generation efficiencies of various systems using different ZT values and Carnot efficiency. The graphic demonstrates that thermoelectrics' efficiency is lower than that of other energy-conversion technologies due to the low performance of TE material. It can be seen that the thermoelectric (TE) materials should have a ZT value of at least 3 to ensure that the device's conversion efficiency is comparable to that of conventional power generators, which can achieve up to 40% Carnot efficiency [5, 22]. Hence, the main objective is to enhance the ZT value of TE materials. Nevertheless, the thermoelectric effect has a wide range of uses today. Some of its uses include microcooling, microheating, powering light sources, and recycling wasted thermal energy from solar cells, motors, factories, or other high-temperature devices. Additionally, industries such as space power generation and various cooling systems widely use thermoelectrics due to their excellent reliability and simplicity [23, 24].

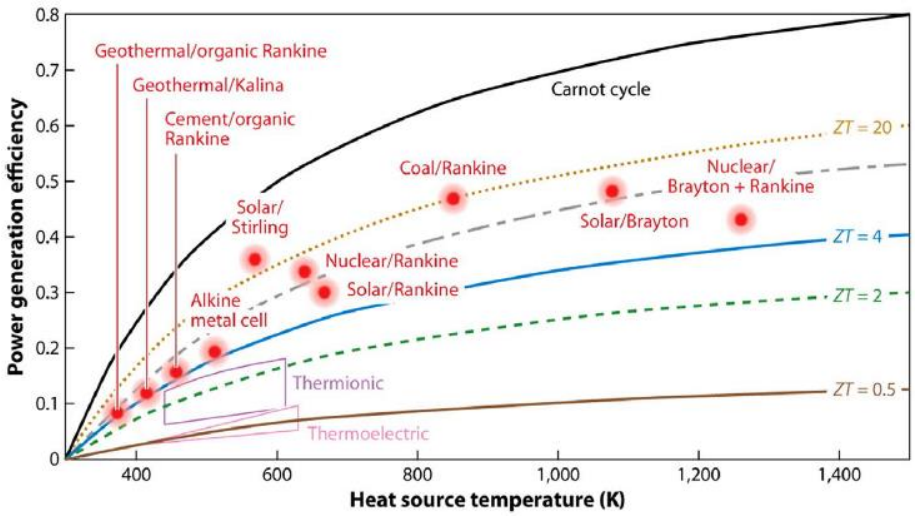


Figure 2.6: Thermoelectric material efficiency as a function of zT and comparison with different heat engine systems [5].

Several methods can be implemented to achieve improved zT values for thermoelectric materials. An increase in the power factor or a decrease in the thermal conductivity is used to achieve thermoelectric materials with a high ZT. The goal is to achieve optimal electrical and thermal transport properties. This requires high electrical conductivity similar to that of a crystalline material while providing low thermal conductivity comparable to that of an amorphous or glass-like material. To get the high power factors (PFs) and Seebeck coefficients, thermoelectric (TE) materials need to have a lot of valleys at the Fermi level and a high band degeneracy. The materials should have a narrow bandgap and high-mobility carriers, while the thermal conductivity has to be low. The bandgap width has a direct influence on electronic properties, specifically the density of states around the Fermi level, which then affects the thermoelectric performance. Compounds should consist of elements with higher atomic masses, as increased phonon scattering causes a decrease in lattice thermal conductivity. The complex distribution of heavy elements in the crystal structure might result in a reduced phonon mean-free path, causing a decrease in lattice thermal conductivity. All of these strategies aim to keep a high power factor and/or reduce lattice thermal conductivities [9, 12, 25].

## *2.4 Thermoelectric Transport Properties*

### *2.4.1 Seebeck Coefficient*

The Seebeck coefficient (α), also known as the thermopower, is defined as the ratio of the thermoelectric voltage generated in a material to the temperature differential across that material. The Seebeck coefficient of a thermoelectric material, namely a degenerate and heavily doped semiconductor, often occurs within several hundred μV/K range. This value can be calculated using a specific equation (Mott formula).

$$\alpha = \frac{8\pi^2.k_B^2.T}{3e.h^2} m * T \left(\frac{\pi}{3n}\right)^{2/3} = \left[\frac{\pi^2.k^2.T}{3e}.\frac{dln\sigma(E)}{dE}\right] \quad (2.5)$$

where $k_B$, $m^*$, $n$, $e$, $h$ and $\sigma(E)$ refer to the Boltzmann constant, density of states effective mass, carrier concentration, electron charge, Planck's constant, and the electronic conductivity as a function of Fermi energy, respectively. The equation indicates that the Seebeck coefficient is directly proportional to the effective mass and inversely proportional to the carrier concentration at a specific temperature. Thus, in order to achieve a high Seebeck coefficient, the material should have a high effective mass and a low carrier concentration. As a result, semiconductors have significantly higher Seebeck coefficients than metals [23].

The electronic conductivity, $\sigma(E)$, is calculated as a function of the band filling or Fermi energy, $E_F$. If electronic scattering indicates energy independence, the function $\sigma(E)$ is directly proportional to the density of states (DOS) at energy E. The α in the Mott equation represents the degree of variation in $\sigma(E)$, both above and below the Fermi surface. The thermopower of a material quantifies the degree of asymmetry in its electronic structure and scattering rates in the region of the Fermi level. As a result, the aim is to create complexity within a small energy interval near $E_F$ in either the electronic structure or scattering rates. Compounds having complex structures and compositions are likely to demonstrate complex electronic structures. Composite materials can provide excellent examples of appearing electronic structures with significant complexity.

Figure 2.7 presents schematic representations of two semiconductors, one with a basic electrical structure and one with a more complex electronic structure.

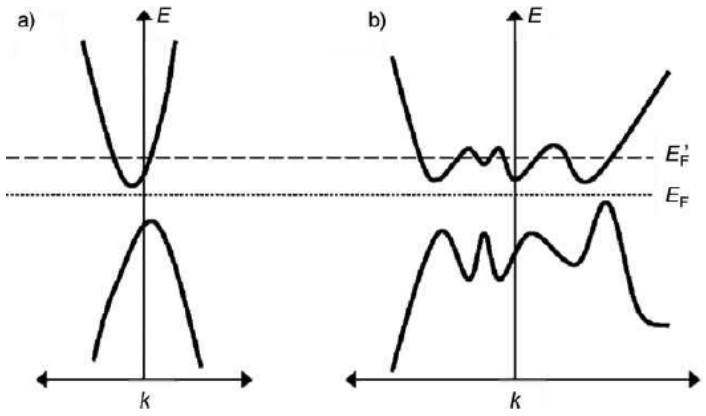


Figure 2.7: Illustration of two semiconductors: (a) with a simple electronic structure, (b) with a complex electronic structure [26].

The band structure shown in Figure 2.7(a) has a basic configuration, containing one band valley in both the valence and conduction bands. In contrast, the band structure shown in Figure 2.7(b) is more complex, displaying several band valleys in both the valence and conduction bands. Therefore, complex structures typically have a higher power factor and Seebeck coefficient than simple structures with similar carrier concentrations [26].

In order to maximize the Seebeck coefficient, it is important to have only one type of carrier (n-type or p-type) present. The presence of mixed n-type and p-type charge carriers would result in the opposite Seebeck effect, decreasing thermopower. To achieve a uniform type of carrier, it is important to carefully choose materials that possess suitable energy bandgaps and proper doping, which allows for the effective separation of n-type and p-type carriers. As a result, thermoelectric materials must be heavily doped semiconductors with an energy bandgap of less than 1 eV to be efficient. This allows them to have one type of charge carrier and a properly high carrier mobility [27].

### *2.4.2 Electrical Conductivity*

The capacity of a substance to carry electrical current is measured by its electrical conductivity. Electrical resistivity (ρ) is inversely proportional to electrical conductivity. According to Ohm's law, the electrical conductivity can be represented as;

$$\frac{V}{l}\sigma = \frac{I}{A} \tag{2.6}$$

where $\sigma$ is electrical conductivity and the *A, I, V* and *l* correspond to the cross-section of the conductor, current, voltage, and length, respectively. The division of voltage to the length of the conductor *(V/l)* is referred to as the electrical field, *E*, while the ratio of current to the cross-section of the conductor *(I/A)* can be termed as current density, *J*. The expression of current density can also be stated as;

$$J = n.q.v_d \tag{2.7}$$

The variables n, q, and $v_d$ represent the number of charge carriers, the charge of the carrier, and the drift velocity, respectively. By integrating the two equations provided above, the expression for electrical conductivity can be redefined;

$$\sigma = \frac{n.q.v_d}{E} \tag{2.8}$$

Equation 2.8 relates electrical conductivity to carrier mobility ($v/E$) (electrons or holes), expressed as $\mu$. The mobility of metals corresponds to electrons, whereas it is related to both electrons and holes in semiconductors. Equation 2.9 represents electrical conductivity by utilizing the mobility parameter.

$$\sigma = \frac{1}{\rho} = n.q.\mu \tag{2.9}$$

In addition, $\mu$ is defined as the mobility of charge carriers, achieved from the equation below;

$$\mu = \frac{e\tau}{m^*} \tag{2.10}$$

where $\tau$ is the average time between two collisions of electrons as they move through the material (relaxation time) and $m^*$ refers to effective mass. Therefore, we can express electrical conductivity as follows by combining the above equations:

$$\sigma = \frac{n.e^2.\tau}{m_e} \tag{2.11}$$

Any change from a perfectly periodic lattice, like impurities, lattice defects, dislocations, grain boundaries, or vacancies, will usually cause the charge carriers to scatter. This is true whether the carriers are in a metal or a semiconductor. Both scattering

methods increase the material's overall resistivity by decreasing the average relaxation time. Consequently, the charge carriers, the effective mass of charges, and the scattering process inside the material determine the electrical conductivity of the material [23, 28].

### *2.4.3 Thermal Conductivity*

The capacity of a material to transport heat under the influence of a temperature gradient between its points is known as thermal conductivity. The thermal conductivity is associated with the transport of heat via the electron or the vibrations of the lattice, which are defined as phonons. The equation of this is indicated as;

$$\kappa = \kappa e + \kappa l \tag{2.12}$$

where $\kappa_e$ and $\kappa_l$ are the electronic and lattice parts, respectively. While the electronic part consists of charge carriers that also transport and transmit heat through the material as a result of their movement, the phonons relate to the lattice part. Since conduction electrons enable heat transfer, metals generally exhibit greater thermal conductivity than non-metal materials. Thus, the thermal conductivity coefficient, $\kappa_e$, is more efficient than the phonon thermal conductivity for conductive materials. Conversely, in the case of an insulator, phonon movement is the main factor contributing to thermal conductivity.

Electrons' ability to move freely through a material determines electronic thermal conductivity, so the value of $\kappa_e$ depends on mobility and the number of charge carriers. If electrons can't easily flow through the crystal lattice without scattering, they can't easily conduct heat. As a result, the heat conductivity and electrical conductivity are linked. The thermal conductivity of the electronic part is defined by Wiedemann–Franz equation;

$$\kappa_e = L.\sigma.T \tag{2.13}$$

where $T$ is the temperature and $L$ is the constant named Lorent'z number with a value of $2.45 \times 10^{-8}\ \Omega\ K^{-2}$. The Lorentz number can be calculated by Equation 2.14 below.

$$L = \frac{\pi^2.k_B^2}{3e^2} \tag{2.14}$$

where $e$ is the electron charge, $k_B$ is Boltzmann's constant and $L$ is the Sommerfeld value, respectively [12]. Enhancing the electrical conductivity leads to a rise in the

electronic thermal conductivity while typically causing a decrease in the thermopower. Consequently, achieving optimal ZT becomes a challenging task [10]. Thus, the purpose of reducing thermal conductivity is to decrease the $\kappa_{lat}$ value while maintaining the $\kappa_e$ value to maintain good electrical conduction properties.

Phonons also transfer heat across the crystal lattice. The lattice conductivity equation is indicated as below;

$$\kappa_{lat} = \frac{1}{3} . C. v. l \tag{2.15}$$

where $C$ is the heat capacity, $v$ is the average phonon velocity and $l$ is the mean free path of phonons. Equation (2.15) can be expanded and simplified into;

$$\kappa_{lat} = \frac{\pi^2 . n . k_B^2 . T . \tau}{3 . m_e} \tag{2.16}$$

Changing the concentration of charge carriers in the material can potentially enhance the power factor. However, reducing $\kappa$ and $\kappa_l$ presents greater challenges, particularly for $\kappa_l$. This parameter is influenced by the lattice's structure, rigidity, atomic masses, and other features. Therefore, in order to decrease the thermal conductivity of the lattice, the main objective is to decrease the average distance traveled by phonons by increasing the amount of phonon scattering. Phonons can undergo scattering due to several factors, such as boundaries between crystals, defects in atomic points, resonant modes in enclosed structures, and interfaces in materials with low dimensions [9]. Figure 2.8 illustrates the potential routes for phonon scattering. To scatter phonons with mid- and long-wavelengths, it is necessary to have larger defects such as grain boundaries, nanoparticles that are embedded, and interfaces. Atomic defects exhibit a high ability to disperse phonons of short wavelengths [27].

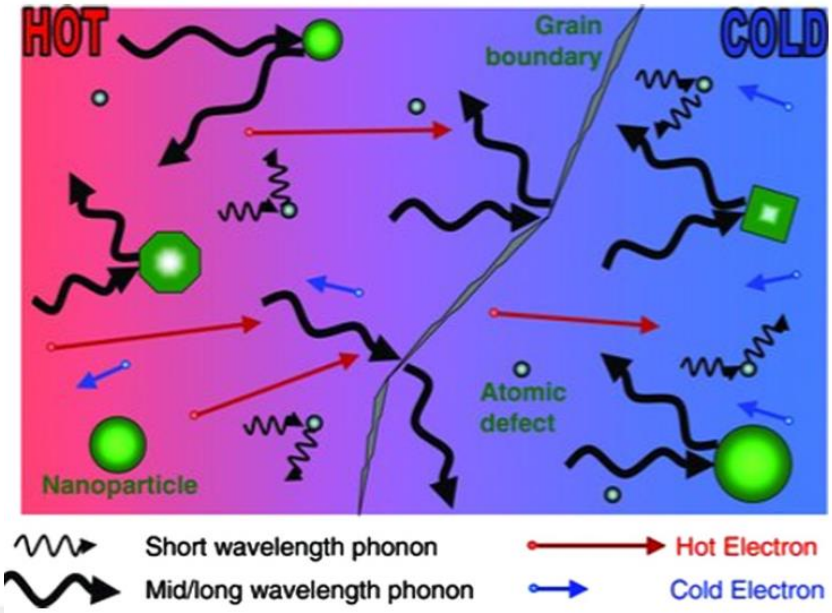


Figure 2.8: Schematic illustration of different phonon scattering processes within the thermoelectric material combined with hot and cold electron movement [27].

# Chapter 3:
# LITERATURE REVIEW FOR TERNARY THERMOELECTRIC PHOSPHIDES

## *3.1 Introduction to Thermoelectric Metal Phosphides*

Phosphides are a class of chemical compounds in which elemental phosphorus is the main component, coupled with one or more less electronegative elements, typically metals. Peltier initiated the study of metal phosphides in 1789, and in 1832, the first Metallophosphorus complex was reported. The rapid development of metallophosphorus chemistry began in the field of organometallic chemistry throughout the 1930s. Almost all metals can form phosphides, and over 200 different binary compounds have already been identified. Furthermore, other ternary compounds consisting of mixed metals and phosphides have been identified, including phosphide borides, phosphide nitrides, phosphide oxides, phosphide halides, phosphide sulfides, and phosphide selenides. These compounds exhibit a variety of crystal forms and can differ significantly in their physical and chemical properties. It is challenging to establish a strict categorization of metal phosphides.

The nature of bond type is frequently unclear, and in some cases, the determination of structure might be viewed as either covalent or ionic bonding. The determination of bond type is not always possible just based on physical features or experimental bond lengths [29].

The aim of improving thermoelectric materials has been driven by the need to solve sustainability concerns and enhance energy security. Innovative design concepts such as phonon-glass electron-crystal, nanostructuring, electronic bandstructure engineering, and enhanced experimental characterization of electrical and heat transport have driven advancements in this field. The electronic properties are directly dependent on the carrier concentration and the electronic band structure. To improve the performance of thermoelectric (TE) devices, it is necessary to have numerous valley degeneracy in the electronic band structure and to optimize the carrier concentration. Furthermore, in order to optimize the electrical properties, it is necessary to reduce $\kappa_l$. Despite the potential application of various methods such as nanostructuring, point defect scattering, and alloy scattering to decrease that, the material's amorphous structure restricts its thermal

conductivity. Increased scattering from external factors typically leads to a decrease in $\kappa_l$, increasing $\rho$. Therefore, low intrinsic heat conductivity is desirable for thermoelectric (TE) applications [30, 31].

Metal phosphides have attracted limited attention as thermoelectrics but they are a group of materials with high potential [30]. The presence of intricate structures frequently results in inherently poor lattice thermal conductivities, hence creating a foundation for potentially high zT values. Indeed, the main goal for many studied materials is to enhance their electrical properties and the value of $S^2\alpha$ [31]. The relation between metal phosphide thermoelectrics and white phosphorus caused small historical interest in this sector. This material consists of weakly linked $P_4$ molecules and is highly pyrophoric, reacting violently with oxygen to form $P_2O_5$ and further with water to form $H_3PO_4$. The formation of highly toxic $PH_3$ gas is also a concern in synthesis involving phosphorus. Nevertheless, red phosphorus, which mainly consists of $(P_4)_n$ oligomers, has better stability and is often used in synthesis [32]. Metal phosphides have the potential to demonstrate remarkable stability upon formation, especially when the presence of electropositive alkali and alkaline earth elements is minimized [33]. The wide variety of available oxidation states of phosphorus from anionic states enables the formation of various structural types and chemical bonds. This causes phosphides to exhibit an important ability for strong covalent bonding and the formation of polyanions, leading to the appearance of complex chemical structures. The complex structures result in a decrease in thermal conductivity inside the lattice, while the relatively light mass of the phosphorus atom contributes to a high zT value. Phosphorus possesses not just a wide range of chemical capabilities but also a high level of abundance and a comparatively inexpensive cost. All these properties of metal phosphides, as well as the fact that they also contain several unique structures with semiconductor or semimetallic band structures, have attracted the attention of thermoelectric research [31].

While metal phosphides are well-known for their stability and remarkable electronic properties, making them appealing for PV/optoelectronics applications, their potential as thermoelectrics is often overlooked due to their expected high thermal conductivity. For example, phosphide skutterudites, such as $CeFe_4P_{12}$, have significant experimental power factors. However, their thermoelectric performance is limited because of their high thermal conductivity [34-37]. Similar behavior was observed in a theoretical investigation

of two-dimensional black phosphorous, which exhibits a significantly higher thermal conductivity, resulting in a reduced zT value [38]. On the other hand, some metal phosphides, such as Zintl phases, have low measured thermal conductivity but have high resistivity, which restricts their zT value [39]. Phosphide clathrates have been found to have a lower electrical resistivity, which can be attributed to the presence of guest atoms that display rattling mechanisms and consequently result in poor thermal conductivities [40, 41]. A recent study examined the thermoelectric properties of $Ag_6Ge_{10}P_{12}$ and found a relatively high zT value of 0.6. $Ag_6Ge_{10}P_{12}$ exhibits low thermal conductivity due to its complex crystal structure and improved electronic properties, which implies that phosphides may demonstrate promising thermoelectric capabilities [42].

The family of phosphides, especially XYP compounds have superior calculated electrical and thermal properties, which make them attractive as thermoelectric materials. The higher electrical conductivity of XYP compounds is attributed to parabolic conduction bands, which also result in high n-type power factors. Multiple band degeneracy of such compounds contributes to a higher Seebeck coefficient. The conduction band is more significantly influenced by the metal orbitals than the valence band, according to the Zintl perspective on chemical bonding. The majority of metal-phosphides exhibit p-type behavior, which is attributed to the presence of modest cation deficiencies. This results in a lack of electrons that fill the conduction band derived from anions, forming holes and enabling p-type conduction [31].

## *3.2 Ternary Ca-Ag-P Materials as Thermoelectrics*

Semimetals have recently become an important topic of current study in the field of thermoelectrics. The stoichiometric compound CaAgP has attracted significant attention because of its band structure [43]. The material was first produced in 1979 by Mewis and forms crystals in space group number 189. It lacks inversion centers but includes mirror planes instead [44]. In 2016, it was documented that the polycrystalline samples of CaAgP exhibit characteristics similar to those of an ideal line-node Dirac semimetal [45]. However, in 2018, ARPES experiments demonstrated that single crystals of CaAgP include a bulk band gap and surface states characterized by a wide bandwidth that is topologically trivial [46]. Rather, it was discovered that CaAgP is a small direct bandgap semiconductor, with the Γ-point gap being approximately 0.15 eV [43]. In addition, as shown in Figure 3.1, some theoretical studies calculated the electronic band structure and

the density of states (DOS), which are important for evaluating the transport properties. Setting the Fermi level ($E_F$) to zero displays the atom-resolved DOS and the atom-resolved band structure along the H–K–Γ–M–L line [47].

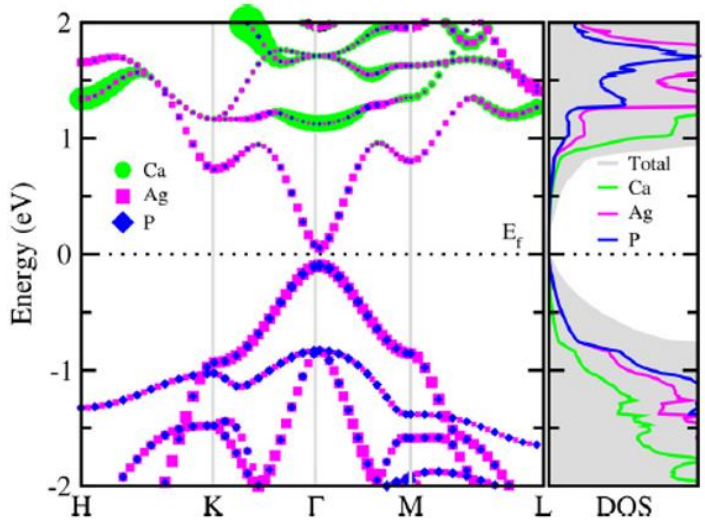


Figure 3.1: The atom-resolved electronic band structure and partial density of states (DOS) [47].

The crystal lattice of CaAgP exhibits hexagonal symmetry, including a network of $AgP_4$ tetrahedra that share corners and edges. With lattice parameters a = b = 7.05 Å and c = 4.19 Å, CaAgP crystallizes in the ZrNiAl-type hexagonal structure (space group $P\bar{6}2m$ (No. 189)), as illustrated in Figure 3.2. The edge-sharing results in forming triangular Ag clusters, where the distance between Ag atoms is 3.06 Å. This distance is slightly larger than the distance observed in elemental Ag, which is 2.9 Å. The Ag atoms are linked together through tetrahedral corners, with a distance of 4.2 Å in the c-direction and 4.7 Å in the ab-plane. The $Ag_3$ clusters are positioned around the P1 site, which is represented by the red P atoms in Figure 3.2 (a). This arrangement results in the formation of "$Ag_3P$" chains along the c-axis. Thus, the electrical band structure of $CaAg_{1-x}P$ exhibits significant anisotropy in its crystal structure [43, 48].

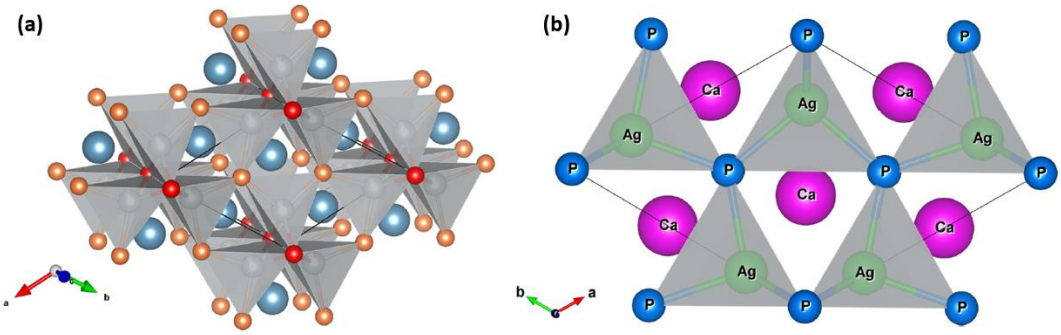


Figure 3.2: (a) Illustration of the atomic arrangement in the crystal lattice of $CaAg_{1-x}P$. Ca, blue; Ag, silver; P at site-1 in red color, and P at site-2 in orange color. (b) The crystal structure of CaAgP in $P\bar{6}2m$ symmetry appears from a top view [43, 48].

Experimental research regarding the thermoelectric properties of CaAgP is limited. Nevertheless, the material is attractive because of its unique electronic band structure and recent studies indicating promising results in metal phosphides. In a recent study, polycrystalline $CaAg_{1-x}P$ material was prepared using the solid-state method followed by hot pressing to obtain dense pellets. As a result of this study, Ag-deficient $CaAg_{0.9}P$ reached zT 0.43 at 660 K with a low lattice thermal conductivity, yielding a promising thermoelectric value [43]. It is important to note that this molecule is composed of widely available and cost-effective components, hence resulting in a decrease in the overall expenses associated with its manufacture. As it can be seen experimental synthesis and thermoelectric measurements of the CaAgP material are very limited, and its development by alloying or doping has not yet been implemented.

## *3.3 Ternary Ca-Cu-P Materials as Thermoelectrics*

The CaCuP material is another thermoelectrically promising ternary phosphide with limited experimental investigation. This material exhibits favorable performance characteristics, is composed of numerous components, possesses low gravimetric densities, and demonstrates excellent stability whether preserved at ambient temperature or subjected to changing temperatures in an inert atmosphere. CaCuP was initially synthesized in the 1970s, but, its characteristics have not been thoroughly explored [49]. CaCuP has a layered hexagonal structure (space group $P6_3/mmc$) consisting of $[CuP]^{2-}$ graphene-like layers separated by $Ca^{2+}$ cations and the lattice parameters of a = 4.070(1)Å and c = 7.826(2)Å [49, 50]. The crystal structure of the material is indicated in Figure 3.3.

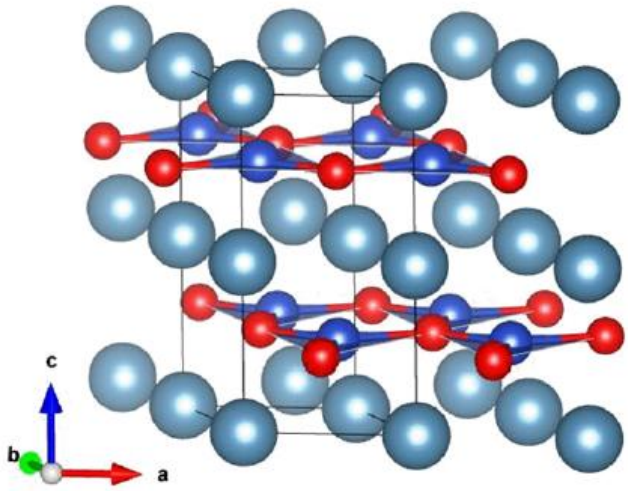


Figure 3.3: Crystal structure of CaCuP, Ca atoms are metallic blue, Cu atoms are blue, and P atoms are red [33].

Electronic structure computations reveal the existence of dispersive bands within the $[CuP]^{2-}$ planes, but the bands that control transport across the $Ca^{2+}$ layers are very flat. Moreover, the calculated indirect electronic bandgaps are reported as $E_g$ = 1.1–1.2 eV, and the direct band gap at Γ is 2.17. The band structure of CaCuP is illustrated in Figure 3.4. The valence band maximum (VBM) is located near the Γ point, and low effective masses of holes are seen in the Γ−M and Γ−K directions. At the Γ point, two degenerate bands exist that result in extremely light and heavier effective masses.

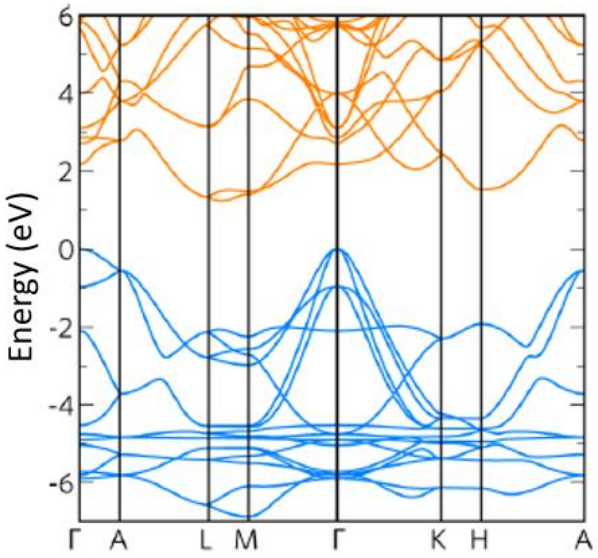


Figure 3.4: The band structure of CaCuP, The filled valence band is colored blue, and the unfilled conduction band is colored orange [50].

The most recent study recorded a maximum zT value of 0.5 at a temperature of 792 K for compound CaCuP [33]. In another study conducted after this study, thermoelectric investigations were carried out by doping As element, but no improvement in the zT value was obtained. Additionally, in this study, the highest zT value was obtained by changing intrinsic doping elements as 0.6 at 873 K, and the best compound was found as $CaCu_{1.02}P$ [51]. The electrical performance of CaCuP is attributed to its favorable balance between the state effective mass density ($m^*_{DoS}$), which controls the mobility of carriers (S), and the high carrier mobilities ($\mu$), which primarily dominate $\rho$. CaCuP exhibits the highest documented $S^2/\rho$ among all phosphides (Except for the exceptional values that come from the quantum thermoelectric Hall effect in TaP) [52]. To conclude, research on the CaCuP material is currently limited, and studies using doped or alloyed materials with other elements have not been carried out yet. Performing these studies is important to make a valuable contribution to thermoelectric applications.

## *3.4 Research Summary*

The objective of this thesis is to explore ternary thermoelectric phosphides, which have been limited research in comparison to other thermoelectric materials. The existence of structural complexity contributes to the achievement of low thermal conductivities, even when the average atomic mass is low. Additionally, the numerous bonding of phosphorus provides the potential to enhance the power factor [31]. By applying new design concepts such as the phonon-glass electron-crystal, nanostructuring, and electronic bandstructure engineering, and by improving the experimental characterization of electrical and heat transport, it is possible to develop CaAgP and CaCuP compounds with p-type ternary state-of-the-art thermoelectrics.

The computed electrical and thermal properties revealed that several metal phosphides can display high thermoelectric performance. Specifically, XYP compounds, depending on the thermal conductivity model applied to compute the thermoelectric performance, have low thermal conductivities with high predicted power factors. The highly anisotropic conduction of XYP compounds, particularly at valence band maxima, which provides relatively high shown p-PFs, is one of their most attractive properties [30]. This thesis will conduct experimental research on CaCuP and CaAgP materials, which are ternary phosphide compounds, to examine their thermoelectric capacities following theoretical understanding. Furthermore, this study will investigate the effects

of doping with various elements on these materials' transport and mechanical characteristics.

# Chapter 4:
# EXPERIMENTAL AND CHARACTERIZATION METHODS

For this study, some initial materials were identified as reactive to air. As a result, the process of weighing and preparing the raw materials was carried out inside a glove box (MBraun) filled with inert argon gas to prevent any reaction with the air. A high-energy ball mill (SPEX8000D) was applied to decrease the initial elements' particle size and synthesize the main products. The compounds were produced by a mechanical alloying method. Once the desired compositions were obtained in the form of a fine powder, spark plasma sintering equipment was employed to carry out the consolidation process. After the synthesis process was completed, annealing was performed on some samples, followed by chemical and thermoelectric characterizations using the techniques discussed in the next sections.

## *4.1 Materials*

Table 4.1 provides the initial chemicals used in this experiment together with their various properties. The elements that are part of the composition are directly placed into the stainless-steel vial in a glove box with argon gas.

Table 4.1 Starting Materials.

| Chemical | Formula | Physical State | Melting Point | Purity (%) | Company |
|---|---|---|---|---|---|
| Calcium | Ca | Pieces | 842 °C | 99.999 | Sigma Aldrich |
| Copper | Cu | Powder | 1083 °C | 99.99 | Nanografi |
| Lanthanum | La | Pieces | 920°C | 99.9 | Sigma Aldrich |
| Nano-Boron | nB | Powder | 2076 °C | 98.5 | Pavezyum |

| | | | | | |
|---|---|---|---|---|---|
| Red Phosphorus | P | Powder | 590 °C | 98.00 | Sigma Aldrich |
| Silver | Ag | Powder | 960 °C | 99.99 | Sigma Aldrich |
| Sodium | Na | Rod | 97.8 °C | 99.99 | Sigma Aldrich |
| Tin | Sn | Powder | 232 °C | 99.995 | Chempur |
| Zinc | Zn | Powder | 420 °C | 99.99 | Sigma Aldrich |
| $Cu_{2.9}Te_2$ | - | Powder | - | - | Lab Scale |

## *4.2 Sample Preparation and Methods*

### *4.2.1 Mechanical Alloying*

To produce compounds by mechanical alloying, a high energy ball mill device (SPEX 8000D) was used to reduce the particle size of the initial materials. Two grinding vials could be positioned between the clamps of the SPEX8000 Miller. The vials were shaken in a rotational motion with short lateral movements, generating G-forces on the vials. During the synthesis, the initial elements reacted with each other, forming a uniform powder. This process is known as mechanical alloying. Figure 4.1 presents the schematic illustration of the SPEX800D.

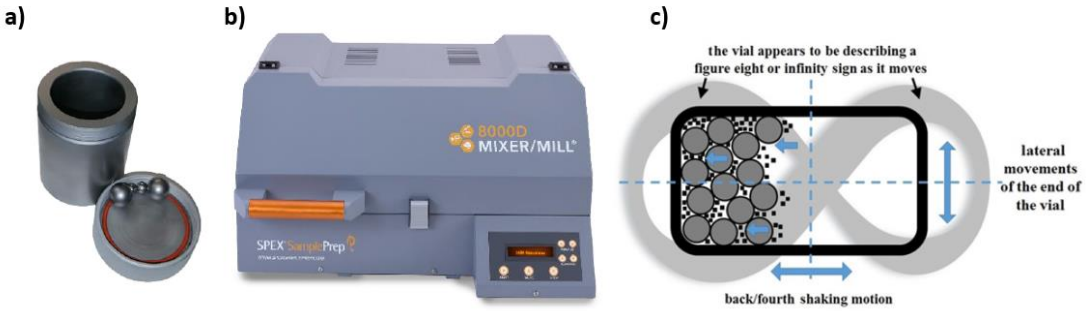


Figure 4.1: a) Grinding vial with stainless steel balls, b) high energy ball milling device, c) working principle of high energy ball mill [53].

This study used high-energy ball milling to synthesize ternary phosphides (CaCuP and CaAgP) and their doping compounds. The required amounts of the initial materials (calcium pieces, silver pieces, powdered phosphorus, powdered copper, lanthanum pieces, nano-boron powder, sodium pieces, powdered zinc, powdered tin, and $Cu_{2.9}Te_2$ powder) were weighed and placed into the high-energy ball mill vial along with two half-inch stainless steel balls, depending on the specific composition. In order to prevent oxidation, the process of weighing and sealing was carried out within a glove box filled with argon gas. Mechanical alloying was applied for two hours at 1200 rpm. Afterward, some unreacted Ca pieces were observed, so powder and Ca pieces were scratched and high energy ball milling technique was applied for another 2 h. Following that, the vial was put back into the glove box, and the final black powder was extracted from the vial for characterization and SPS processes.

### *4.2.2 Spark Plasma Sintering*

The spark plasma sintering technique was applied to make more dense and compact fine powder samples following mechanical alloying, utilizing an SPS (AGUS-PECS SPS-320Sx from SUGA Co., Ltd.). Spark plasma sintering is a method of sintering and synthesis that involves the use of low voltage, direct current (DC) pulsed current, and pressure assist. SPS and hot pressing (HP) are similar in their purpose of sintering materials, but they differ in the method of producing heat and transmission. This technique offers several benefits, such as reduced processing time and improved particle contact. It may change the quantity and shape of particle contacts, enhance existing densification mechanisms found in regular sintering (such as grain boundary diffusion, lattice diffusion, and viscous flow), and activate additional mechanisms like plastic

deformation or grain boundary sliding [54]. Figure 4.2 shows the SPS system. The SPS system includes a vacuum chamber that generates a specific atmospheric condition, a sintering machine that applies vertical forces along a single axis using electrode punches, a DC pulse power supply that controls the sintering processes, and a thermocouple that measures the temperature of the sintering environment.

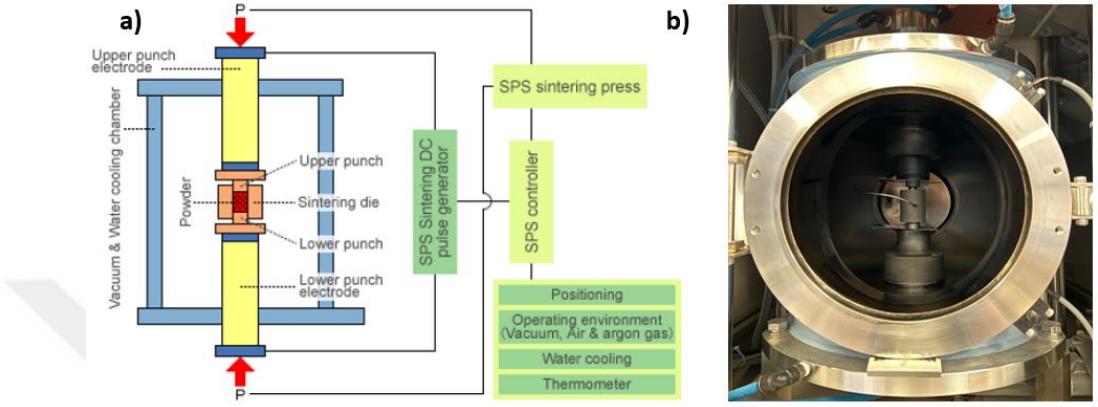


Figure 4.2: a) Schematic representation of Spark Plasma Sintering system [55], b) the image of the vacuum chamber.

Typically, spark plasma sintering occurs through four main stages. The initial step involves the removal of gases and the establishment of a vacuum. Applying pressure in the second stage is followed by the application of resistance heating in the third stage, and finally, the process of cooling in the fourth step. The powder sample is directly inserted in a mold without any prior treatment. An electric current with high intensity and low voltage is applied directly to the powder inside the mold. The hydraulic system applies pressure along the Z-axis. The punches serve as electrodes that facilitate the conduction of the electrical current. The hydraulic pistons are equipped with a water-cooling system to minimize the risk of overheating. The DC pulse generator manages the pressure level during the sintering process to avoid excessive pressure. A thermocouple is employed as a temperature-regulating device, based on the target maximum temperature for the sintering process.

Compared to traditional methods, the SPS technology uses pulsed direct currents to heat the sample both outside and inside by passing them through the graphite dies and the sample itself. Applying an electrical potential to the sample causes sparks to be formed at the contact points between the particles, resulting in the flow of electrons and the

discharge of plasma. The sparks rapidly increase the surrounding temperature to several thousand degrees Celsius. Due to Joule heating, the surfaces of the particles undergo evaporation and melting, resulting in a rapid formation of necks. In the end, the application of pressure facilitates the densification process by supporting additional mechanisms such as plastic deformation, dislocation, and diffusional creep, which provides the elimination of isolated pores. The various mechanisms involved in SPS are shown in Figure 4.3 [55, 56].

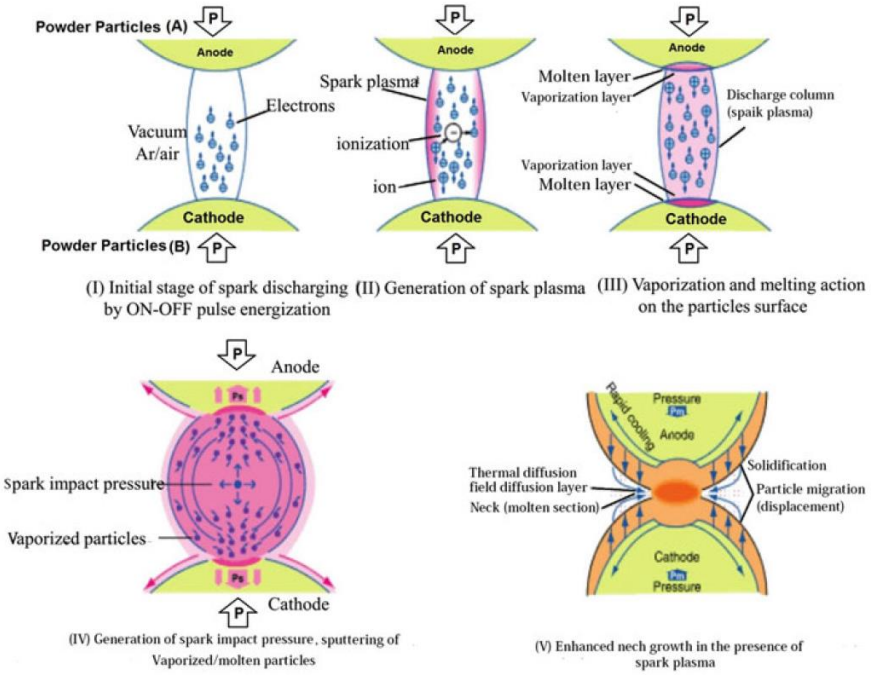


Figure 4.3: Mechanism of spark plasma sintering neck formation [56].

For sintering by spark plasma sintering, powders were loaded into a graphite die with a 10 mm inner diameter that was covered in graphite foils in a glove box. To optimize the sintering temperature and pressure, different temperature and holding time parameters were applied to the materials at separate times. The obtained powder samples were sintered at optimum parameters of 800°C and under 50 MPa pressure for 10 minutes and turned into pellets. Finally, the pressure was relieved, and the chamber was cooled to room temperature.

### *4.2.3 Diamond Wire Saw Cutting*

To prepare samples for LFA and ZEM-3 measurements, all pellet shapes need to be cut both horizontally and vertically. Diamond wire saws were used to cut the samples into the right shapes for this reason. Accurate values for LFA measurements require cylindrical samples with a thickness of 1.5 mm to 2 mm. The sample from SPS was polished and attached to the sample holder horizontally in order to cut it to that thickness. Following the LFA sample's cutting, the remaining sample was stuck to the sample holder vertically. Bar samples were cut with dimensions of 2x2x6 mm for the ZEM-3 analysis. Water worked as a coolant, and a lubricant was added to the water to prevent corrosion and enhance cutting performance throughout all cutting stages. To obtain a uniform and polished shape for future measurements, the samples are carefully sanded using SiC paper. Figure 4.4 illustrates the setup and directions of the cutting process.

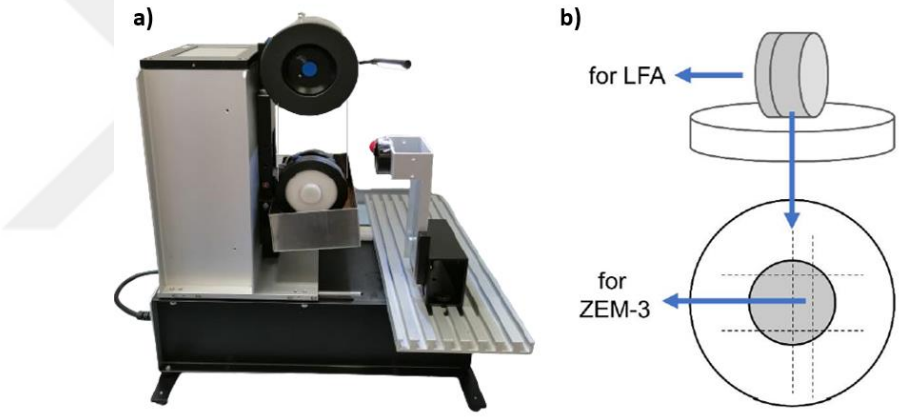


Figure 4.4: a) Diamond Wire Saw instrument, b) cutting positions of every specimen.

## *4.3 Material Characterization Techniques*

### *4.3.1 X-Ray Diffraction*

X-ray diffraction (XRD) is a non-destructive method used to analyze materials. It is beneficial for determining the crystal structures and phase purity of samples and providing information about lattice parameters and grain sizes of the phases.

The constructive interference of the X-rays and the crystalline sample generates X-ray diffraction. X-rays are produced in a cathode ray tube through the bombardment of the target material (Cu, Fe, Mo, Ag, or Cr) by electrons. These X-rays are collimated and

filtered to produce monochromatic energy. Following that, to generate interference, a beam of monochromatic X-rays is targeted at the sample. When the periodic lattice of the samples scatters the collimated X-ray beams, constructive and destructive interference occurs only if Bragg's law is satisfied. This law may be expressed by the following equation. The result of constructive interference is a diffraction pattern [57].

$$n\lambda = 2dsin\theta \quad (4.1)$$

The variables d, θ, n, and λ represent the perpendicular distance between neighboring planes, the angle of incidence, the order of diffraction, and the wavelength of the X-ray, respectively. By comparing the findings of each unique diffraction pattern to a database, the chemical composition of the material can be identified [57].

Cu Kα (λ=1.540598 Å) radiation, a 40 kV voltage, and a 20 mA current were applied by the Rigaku Miniflex XRD equipment in this work to analyze both powder and bulk samples. Using crystallographic data from the ICSD database, STOE WinXPOW software analyzed each X-ray powder diagram.

### *4.3.2 Scanning Electron Microscopy*

A scanning electron microscope is an electron microscope that creates images by scanning the surface of the specimen using a focused electron beam. Scanning Electron Microscopy (SEM) may provide data regarding the surface topography, crystalline structure, chemical composition, and electrical characteristics.

A scanning electron microscope (SEM) consists of an electron gun, condenser lenses, electron detectors, an objective lens, and a vacuum system. At first, electrons are produced in an electron gun, then accelerated downwards and directed through several lenses and apertures to create a focused electron beam that impacts the surface of the sample. To minimize electron scattering by air, these processes are carried out in a high vacuum environment. As the electrons arrive at the sample, incident electrons saturate it, causing an excitation that produces a variety of signals. Different types of signals, including secondary electrons, backscattered electrons, auger electrons, distinctive X-rays, and cathodoluminescence, can be produced depending on the characteristics of the interaction between the sample and the electron beam [58, 59].

The main electrons interact with the sample, producing ionization of atoms and generating the secondary electron signal. This signal is widely used in scanning electron microscopy (SEM). Secondary electrons are produced through various inelastic scattering mechanisms that occur in the surface or nearby regions of the sample. The secondary electrons have a relatively low energy level of approximately 5 electron volts (eV) and provide important insights into the topography of specimens. This allows the visualization and analysis of surface patterns with a resolution as fine as 10 nanometers (nm). Electrons that strike an atom's nucleus and approach it closely enough to scatter across a wide angle and resurface from the surface are known as backscattered electrons. They are created when electrons and atoms collide elastically. Although they are less abundant than secondary electrons, they have higher amounts of energy. For the most part, they provide compositional data—higher atomic mass elements produce a stronger contrast. Since electron channeling takes place, backscattered electrons can also contribute crystallographic information [58-60]. The elemental composition and distribution of each element in the material are analyzed using Energy Dispersive X-ray Spectroscopy (EDS) together with Scanning Electron Microscopy (SEM) to produce elemental maps.

SEM measurements were carried out in this study using a Zeiss Ultra Plus Field Emission Scanning Electron Microscope located in the KUYTAM laboratory. After mounting the samples using the Citopress 30 Struers mounting press, the bulk samples were highly polished using the Tegramin 30 Struers automatic sample polisher system with a diamond solution. Following the preparation process, the samples were carefully positioned on a carbon tape, and the measurements were effectively obtained.

## *4.4 Transport Property Measurements*

### *4.4.1 Thermal Diffusivity and Thermal Conductivity*

The thermal diffusivity values of the synthesized samples are measured using the laser flash method. The NETZSCH LFA 467 HT Hyper Flash device given in Figure 4.5a is used in this thesis to determine diffusivity values. Thermal diffusivity is a material-specific property for characterizing unsteady heat conduction. This value indicates how quickly a material responds to temperature changes. Applying the laser flash method, a short energy light pulse from the Xenon lamp heats the sample's lower surface. The temperature change on the top of the sample is then measured using an infrared detector,

producing a signal. The device calculates and displays the diffusivity by taking into account the thickness of the sample and the time value at half signal height. Before loading the samples into the device, a small layer of graphite is applied to the samples. This decreases reflection and provides better absorption and emission properties, thereby enhancing the signal-to-noise ratio. This step is necessary because LFA is an optical method.

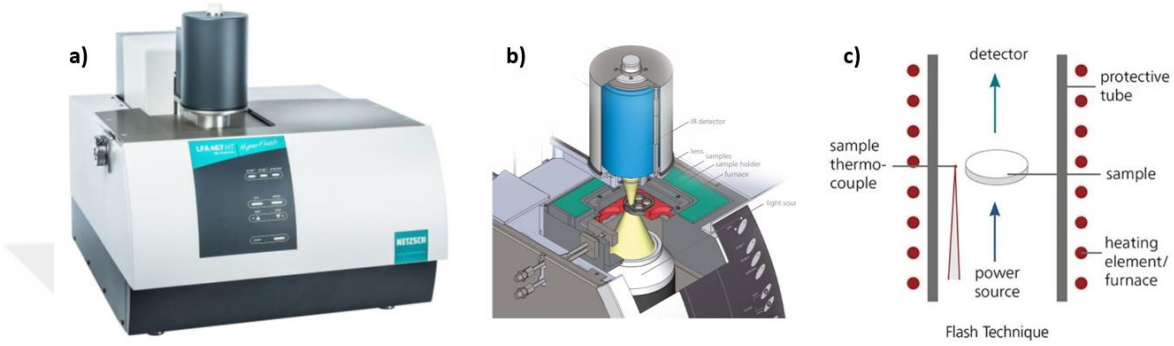


Figure 4.5: a) Laser flash analysis (LFA 467 HyperFlash) device, b) the schematic representation of the instruments part, c) illustration of laser flash technique.

Equation 4.2 defines the thermal diffusivity ($a$) value, which depends on the material thickness ($d$) and half-time at half-signal height ($t_{1/2}$).

$$\alpha = 0.1388.\frac{d^2}{t_{1/2}} \qquad (4.2)$$

By using thermal diffusivity values, the thermal conductivity of samples at specific temperatures is calculated shown below;

$$\kappa(T) = d(T).\ C_p(T).\ \alpha(T) \qquad (4.3)$$

where $\kappa$, $d$, $C_p$, and $\alpha$ correspond to the thermal conductivity (W/m·K), density (g/cm$^3$), specific heat (J/g·K), and thermal diffusivity (mm$^2$/s), respectively. The density of the samples was calculated using the Archimedes method with ethyl alcohol at room temperature. Dulong Petit method was used to calculate $C_p$ values. All analyses were performed on 10 mm disc-shaped pellets positioned in 12.7 mm round holders. All analyses were carried out under an argon atmosphere, from 50 °C to a maximum of 550 °C.

### *4.4.2 Heat Capacity ($C_p$)*

The Dulong-Petit law can be used to determine the heat capacity ($C_p$) by considering the vibrational degrees of freedom of the atoms. Because each atom vibrates in three dimensions, the energy of an atom is $3k_BT$, which is equivalent to $3k_BTN_A$ for a mole of the atom by multiplying the number of atoms in one mole. Thus, the specific heat, $C_p$, can be calculated using the following formula:

$$C_p = \frac{3NR}{\mathrm{M}} \tag{4.4}$$

$N$, $R$, and M represent the total number of atoms in a chemical formula, the constant equivalent to $k_BN_A$, and the molar mass of the material, respectively.

### *4.4.3 Electrical Resistivity and Seebeck Coefficient*

The ULVAC ZEM-3 equipment, as indicated in Figure 4.6, was used to conduct simultaneous measurements of electrical resistivity and Seebeck coefficient.


Figure 4.6: Electrical resistivity and Seebeck coefficient measurement system.

The samples used for measurements are cut into rectangular rods with dimensions of approximately 2 mm in wide and 6 mm in high. Graphite sheets are placed between all four probes and between the contacting surfaces of the samples to avoid contamination and enable the protection of the probes. A rectangular-shaped material is placed vertically between the top and lower electrodes and heated to the required measurement temperatures. To eliminate oxygen, it is removed and then refilled with helium (He) three

times in a 15-minute cycle. Additionally, a small quantity of He is injected into the chamber to maintain an environment conductive. A heater in the lower block generates a temperature gradient on the sample. A constant current flows through the electrodes during the measurement. Measurements were carried out at elevated temperatures using temperature variations of 10, 20, and 30 K. A thermocouple is used to measure the temperature difference and the electromotive force, *dE*. The following formula is utilized to compute the Seebeck coefficients (S) using the DC method:

$$s = \frac{\Delta V}{\Delta T} \tag{4.5}$$

where $\Delta V$ and $\Delta T$ are the voltage difference and temperature difference, respectively. The electrical resistivity (or electrical conductivity) can be measured using the four-terminal method, which involves determining voltage changes between thermocouples when current flows through upper and lower electrodes. The following calculation determines the electrical resistivity;

$$R = \frac{V}{l}\frac{A}{d} \tag{4.6}$$

The variables $\rho$, $A$, $I$, and $d$ represent the resistivity, cross-sectional area, applied current, and distance between the thermocouple probes, respectively. Figure 4.7 provides a schematic representation of the Seebeck and electrical resistivity measurements.

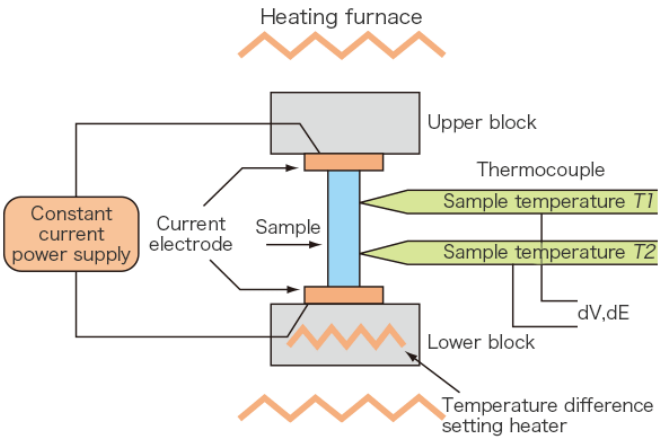


Figure 4.7: Illustration of the electrical resistivity and Seebeck coefficient measurement system.

### *4.4.4 Vickers Hardness Test*

Shimadzu HMV-G Series Micro Vickers Hardness Tester is used to determine the microhardness of the materials. To determine the surface hardness, it is necessary to flatten the surface of the specimen initially. During the analysis, a load of 0.01HV (98.07 mN) and 0.025HV (245.2 mN) are applied to the materials to find the appropriate load.

Typically, a diamond indenter with a pyramidal form is used to apply and load a force on the surface for 10-15 seconds, ensuring stability without any vibrations or strikes. Afterward, the indenter is raised from the surface, and the diagonals of the mark on the surface are measured to determine the Vickers hardness. The Vickers hardness is calculated using the following equation.

$$HV = \frac{0.1891 * F}{d^2} \tag{4.7}$$

where F is the load applied and d is the average of the two diagonals in millimeters.

# Chapter 5:
# RESULTS AND DISCUSSION

This section will examine the results of the ternary phosphides CaAgP and CaCuP and the effects of various doping elements.

## *5.1 Results of CaAgP Ternary Phosphide Phase*

### *5.1.1 Preparation*

The elements and dopants used to prepare the CaAgP compound are given in Chapter 4. CaAgP in powder form was prepared by mixing the initial pieces of calcium, and powder of silver and red phosphorus in different stoichiometries. In addition, nano Bor, the rod of sodium, powders of zinc, pieces of lanthanum, and powders of tin elements were used to make doping compositions. Zinc, lanthanum, tin, sodium, and nano boron at 0.05 at.%, 0.075 at.%, and 0.1 at.% were prepared separately, mixed with other starting elements, and then synthesized using a high-energy ball mill. Besides these elemental dopings, 0.05% by weight of $Cu_{2.9}Te_2$ compound was added externally to all starting (Ca, Ag, and P) materials, and the new sample was prepared according to stoichiometric calculations. All different compounds were prepared by changing the Ag and Ca content. Due to the air sensitivity of red phosphorus and the increased reactivity of elements from high-energy ball milling, we weighted all the precursors under an Argon atmosphere according to stoichiometry. Separately prepared powders were placed into the stainless-steel vial with two half-inch stainless-steel balls in a glove box with argon gas and high-energy ball milling was applied for 2 h at 1200 rpm. Afterward, some unreacted Ca pieces were observed, so powder and Ca pieces were scratched and high energy ball milling technique was applied for another 2 h. The final black powder was removed from the vial within the glovebox. After that, the powder was sintered on spark plasma sintering (SPS) to form dense bulk materials.

For sintering by spark plasma sintering, powders were loaded into a graphite die with a 10 mm inner diameter covered in graphite foils and into the graphite die between the graphite punches. It was slightly cold-pressed before placing the graphite mold into the SPS to obtain a more compact material. Graphite dies with powder samples were positioned between punch electrodes within the vacuum chamber. Once a vacuum

atmosphere was achieved, the sintering process started. The obtained powder samples were sintered at 800°C under 50 MPa pressure for 10 minutes by using the spark plasma sintering method to form pellets. After these processes, the pellets were removed from the graphite die and polished with 600, 800, 1000, and 1200 grit $SiO_2$ sandpapers.

After SPS, some polished samples were placed in glass and quartz tubes and then were put into furnaces for heat treatment as shown in Figure 5.1. To prevent the tube from breaking during the operation, quartz wools were placed inside the alumina crucible. Heat treatment was carried out by keeping the pellets at different temperatures and at different times. The purpose of this process is to lower the electrical resistivity by increasing the grain size and decreasing the grain boundary densities. When the heat treatment period was over, the quartz/glass tubes were taken out of the furnace, and pellets were sanded again with sandpaper.


Figure 5.1: a) The material placed in the thin quartz/glass tube, b) The image of the alumina crucible in the furnace, c) The image of the material after annealing.

The preparation conditions for all CaAgP samples, both doped and undoped, including SPS and annealing procedures, are summarized in Table 5.1. The contributions of doping with different elements, internal doping methods, annealing temperatures, and times to the thermoelectric properties of CaAgP ternary phosphide were examined.

Table 5.1 Preparation conditions of CaAgP ternary phosphide samples.

| Sample Name | Composition | Excess Addition | Ball Milling Time | SPS Temperature (°C) | Sps Time (minute) | Heat Treatment Temperature (°C) | Heat Treatment Duration (day) | Density ($g/cm^3$) |
|---|---|---|---|---|---|---|---|---|
| MA09 | $CaAg_{0.85}P$ | - | 4h | 800 | 10 | - | - | 4.61 |
| MA07 | $CaAg_{0.90}P$ | - | 4h | 800 | 10 | - | - | 4.69 |
| MA10 | $CaAg_{0.95}P$ | - | 4h | 800 | 10 | - | - | 4.64 |
| MA04 | CaAgP | - | 4h | 800 | 10 | - | - | 4.83 |
| MA17 | $Ca_{0.95}Ag_{0.90}P$ | - | 4h | 800 | 10 | - | - | 4.77 |
| MA20 | $CaAg_{0.90}P$ Annealing | - | 4h | 800 | 10 | 450 | 3 | 4.60 |
| MA19 | $Ca_{0.95}Ag_{0.90}P$-$B_{0.05}$ | 0.05 at. % nB | 4h | 800 | 10 | - | - | 4.64 |
| MA21 | $CaAg_{0.90}P$-$B_{0.1}$ | 0.1 at. % nB | 4h | 800 | 10 | - | - | 4.61 |
| MA23 | $CaAg_{0.90}P$-$B_{0.05}$ | 0.05 at. % nB | 4h | 800 | 10 | - | - | 4.63 |
| MA25 | $Ca_{0.95}Ag_{0.90}P$-$Na_{0.05}$ | 0.05 at. % Na | 4h | 800 | 10 | - | - | 4.64 |
| MA35 | $CaAg_{0.90}P$-$Zn_{0.1}$ | 0.1 at. % Zn | 4h | 800 | 10 | - | - | 4.70 |
| MA37 | $CaAg_{0.90}P$-$Zn_{0.1}$ Annealing | 0.1 at. % Zn | 4h | 800 | 10 | 600 | 2 | 4.70 |

| | | | | | | | | |
|---|---|---|---|---|---|---|---|---|
| MA30 | $(CaAg_{0.90}P)_{0.95}$ -$(Cu_{2.9}Te_2)_{0.05}$ | 0.05 at. % $Cu_{2.9}Te_2$ | 4h | 800 | 10 | - | - | 4.71 |
| MA36 | $Ca_{0.95}Ag_{0.90}P$-$La_{0.05}$ | 0.05 at. % La | 4h | 800 | 10 | - | - | 4.72 |
| MA43 | $Ca_{0.95}Ag_{0.90}P$-$La_{0.05}$ Annealing | 0.05 at. % La | 4h | 800 | 10 | 600 | 4 | 4.73 |
| MA41 | $Ca_{0.95}Ag_{0.90}P$-$La_{0.075}$ | 0.075 at. % La | 4h | 800 | 10 | - | - | 4.74 |
| MA40 | $CaAg_{0.925}P$-$Zn_{0.1}$ | 0.1 at. % Zn | 4h | 800 | 10 | - | - | 4.72 |
| MA42 | $CaAg_{0.925}P$-$Zn_{0.1}$ Annealing | 0.1 at. % Zn | 4h | 800 | 10 | 600 | 4 | 4.71 |
| MA44 | $CaAg_{0.90}P$-$Sn_{0.05}$ | 0.05 at. % Sn | 4h | 800 | 10 | - | - | 4.66 |
| MA45 | $CaAg_{0.90}P$-$Sn_{0.1}$ | 0.1 at. % Sn | 4h | 800 | 10 | - | - | 4.70 |

### *5.1.2 Crystal Structure Characterization*

All samples were analyzed using XRD with a Cu-$K_\alpha$ source ($\lambda$=1.5406 Å) to determine their phase purities and crystal structures. XRD analysis of all powders with different Ag content was applied as can be seen in Figure 5.2. All doped powder samples performed X-ray diffraction examination and were then displayed on a graph (Figure 5.3). The samples were successfully synthesized in accordance with the theoretical peaks, as shown in the graphs. All the main peaks from the hexagonal CaAgP ($P\bar{6}2m$ space group) matched the synthesized powder samples' XRD patterns well.

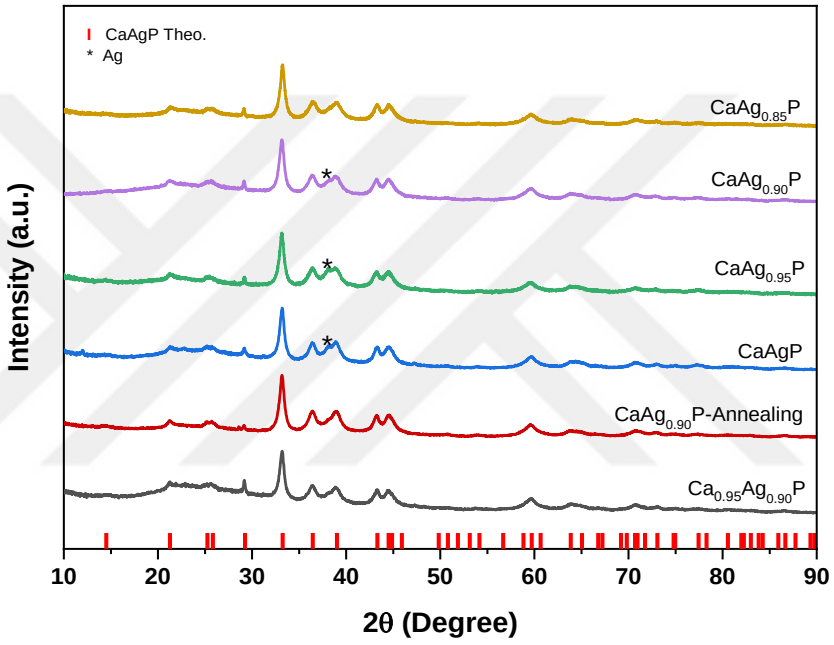


Figure 5.2: XRD patterns of CaAgP powders in different compositions. The red lines show the theoretical peak positions of CaAgP.

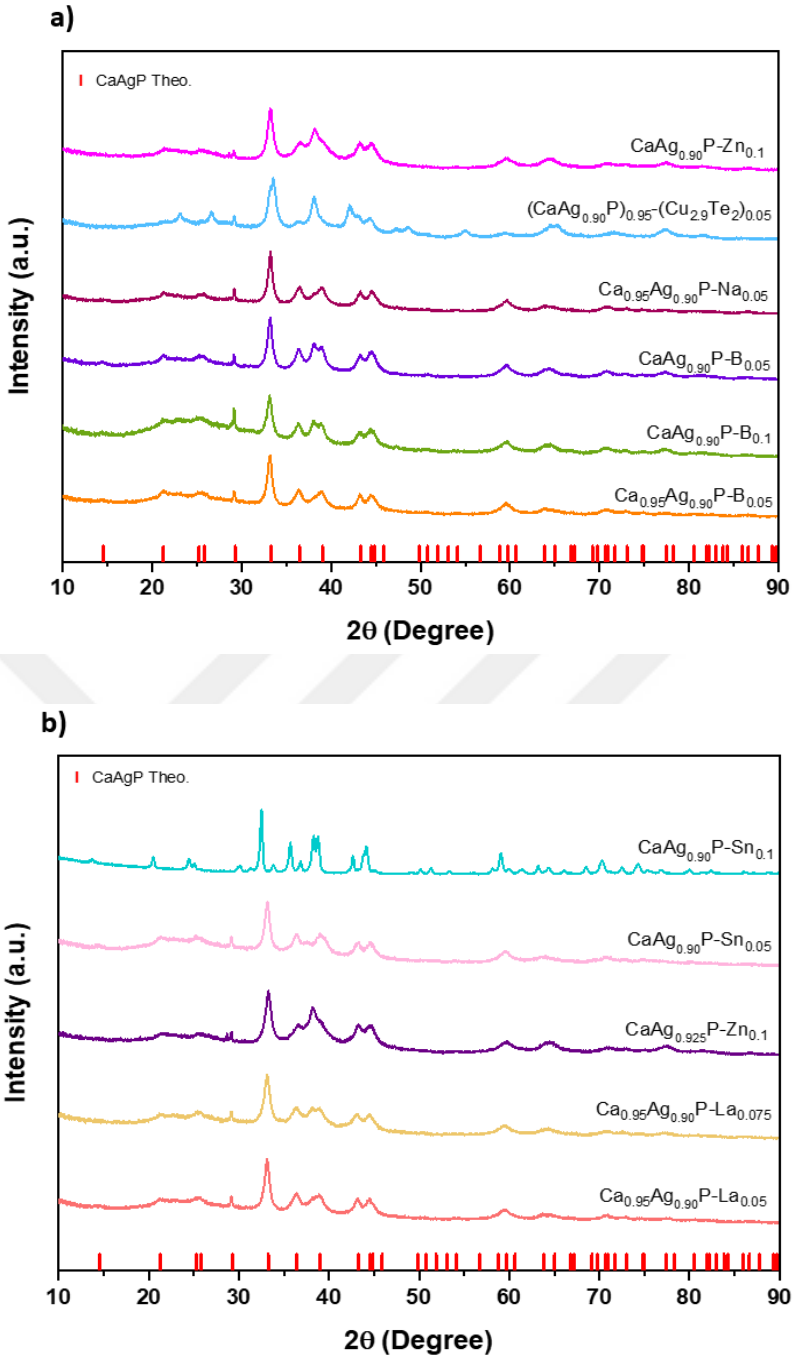


Figure 5.3: (a-b) XRD patterns of CaAgP powders with different dopants.

Graph 5.4 shows the XRD patterns of undoped and intrinsically doped pellets sintered under the same conditions. The XRD patterns of samples of CaAgP, $CaAg_{0.95}P$, and $Ca_{0.95}Ag_{0.90}P$ show some excess Ag content, but the XRD patterns of the two samples with lower Ag content contain secondary phases, CaO. The peaks of all samples matched the theoretical peaks despite the secondary phase and excess Ag.

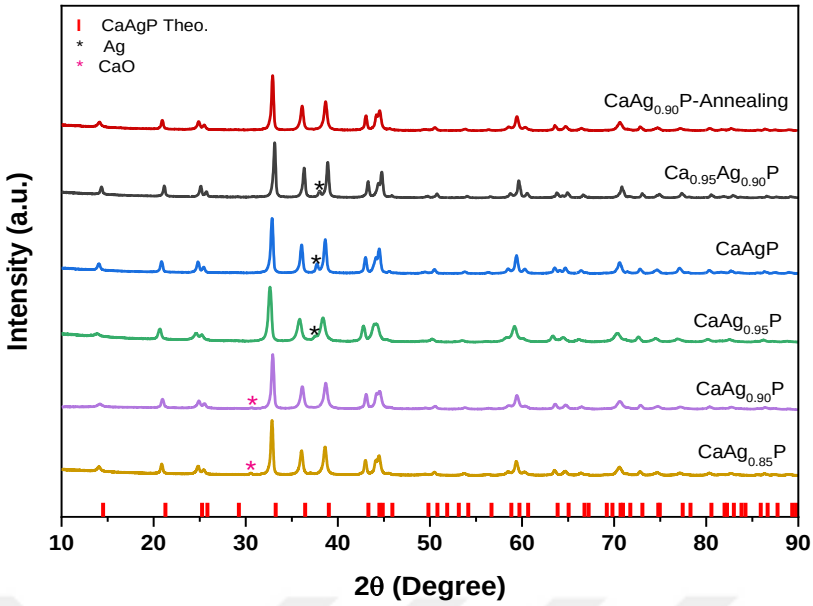


Figure 5.4: XRD patterns of undoped and intrinsically doped CaAgP pellets in different compositions.

The XRD patterns of doped pellets sintered under the same conditions are given in Figure 5.5. All samples match exactly with the hexagonal CaAgP crystal structure, although some doping samples have secondary phases and excess elements. Four different compounds, respectively $Ag_2Te$, CuTe, $Ag_{0.97}Cu_{0.03}$, and CaTe, were observed in the $(CaAg_{0.90}P)_{0.95}$-$(Cu_{2.9}Te_2)_{0.05}$ sample synthesized to make a composite. In addition, excess Ag element was detected in 0.05 nano boron-doped $Ca_{0.95}Ag_{0.90}P$ sample. The excess Ag and Ca elements were detected in Zn-doped samples. As the Zn-doped samples were compared, the heat treatment caused some shift in the peaks of the annealing sample. Two different compounds, LaP and AgLa were observed in the $Ca_{0.95}Ag_{0.90}P$-$La_{0.075}$ and $Ca_{0.95}Ag_{0.90}P$-$La_{0.05}$ samples synthesized by extrinsic doping method. In Sn-doped samples, excess Sn, Ca, and P elements were observed. The annealed sample peaks only slightly shifted as a result of heat treatment in comparison to La-doped samples.

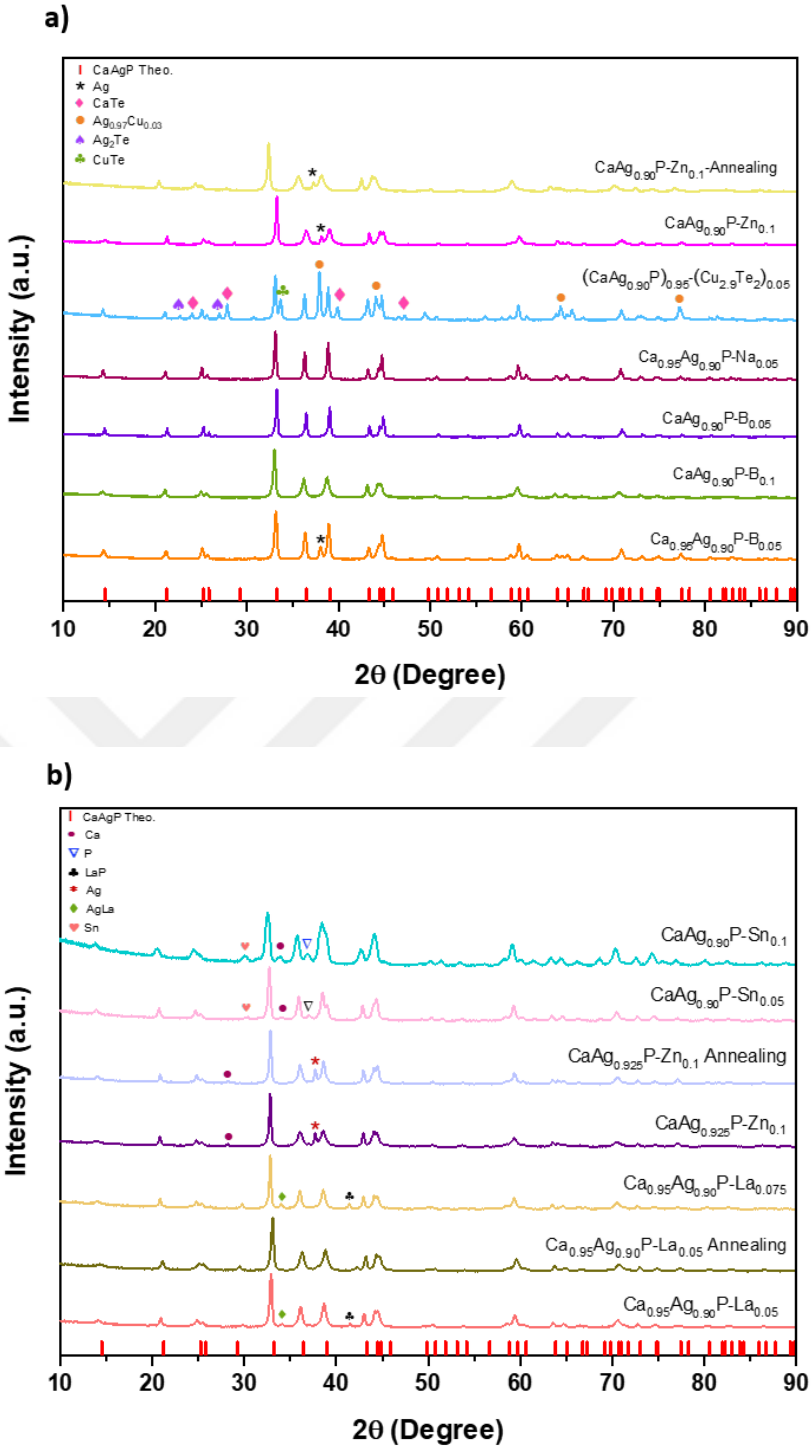


Figure 5.5: (a-b) XRD patterns of CaAgP pellets after the sintering process with different dopants.

### *5.1.3 Chemical and Microstructure Characterization*

SEM and EDS analyses of promising samples regarding thermoelectric performance were performed. SEM and EDX analyses were conducted selectively on the doped

materials because these analyses were performed after evaluating the thermoelectric performance. Figure 5.6 shows the SEM images of the pellets with different Ag content. The surfaces of the samples of CaAgP and $CaAg_{0.95}P$ have some Ag on them, which appear as white regions in the images. Dark regions were observed on the surfaces of the two samples with lower silver content, implying the surface porosities.

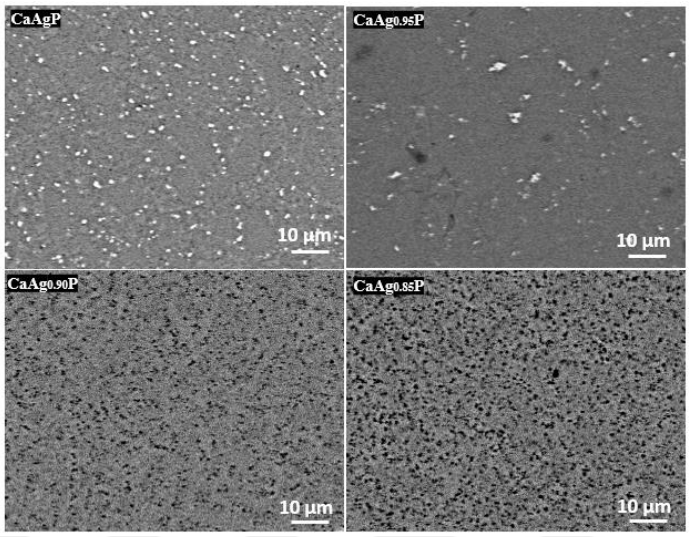


Figure 5.6: SEM images of CaAgP samples with different Ag contents.

Figure 5.7 indicates the results of the EDX analysis performed on pellet samples to check the homogeneity of the material. As can be seen from the EDS elemental mapping, phosphorus, silver, and calcium are distributed homogeneously. Also, excess Ag can be detected in the bright region. As a result of the analysis, characteristic peaks are observed in the energy levels of Ca, Ag, and P elements.

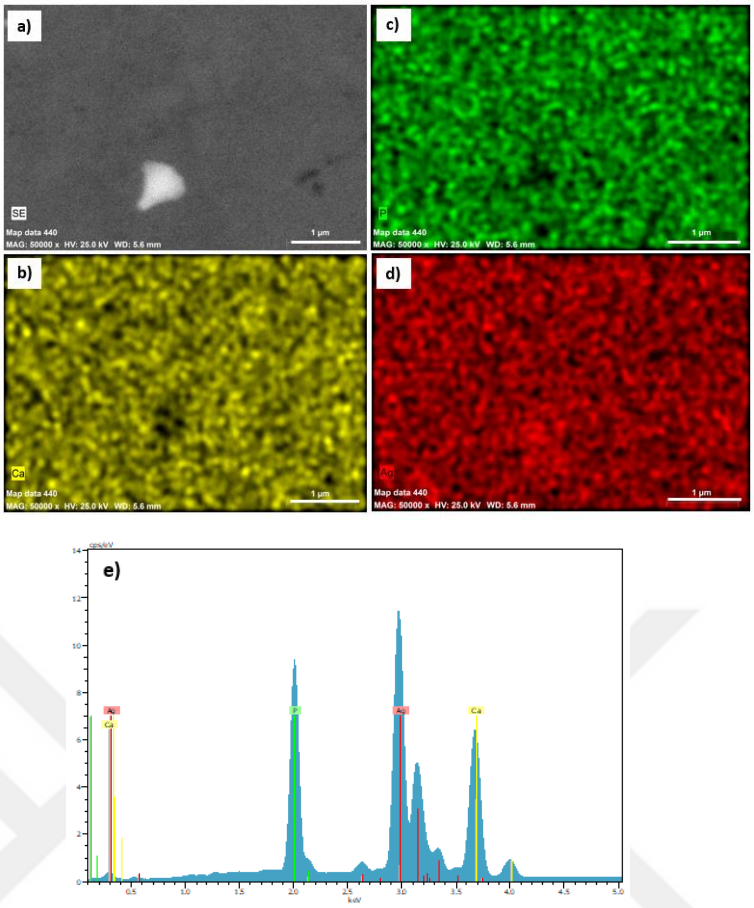


Figure 5.7: a) SEM image of sample $CaAg_{0.95}P$, elemental mapping of b) Ca , c) P , d) Ag , and e) EDS spectra of $CaAg_{0.95}P$.

In Figure 5.8, SEM images of the undoped sample of $Ca_{0.95}Ag_{0.90}P$ and the annealing sample of $CaAg_{0.90}P$ are given. A more homogeneously dispersed porous structure was observed in $CaAg_{0.90}P$-Annealing with the effect of high temperature and long time. Large-scale porous or cracks were not seen in the samples that were obtained. The brighter regions are found to have slightly high Ag content. This is the case in almost all samples in the ternary Ca-Ag-P system.

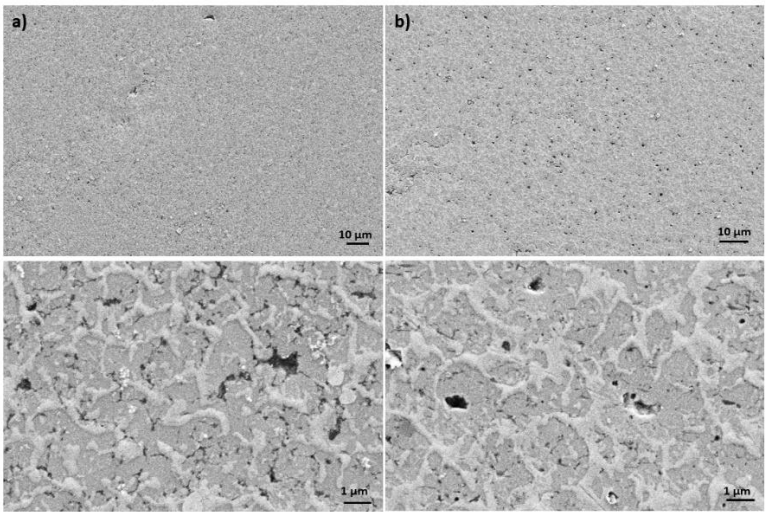


Figure 5.8: SEM images of (a) undoped $Ca_{0.95}Ag_{0.90}P$ sample with a magnified image given below, (b) SEM images of $CaAg_{0.90}P$-Annealing sample with a magnified image given below.

Figures 5.9 and 5.10 display the results of the EDX analysis performed on pellet samples to check the homogeneity of the materials. As can be seen from the EDS element map, phosphorus, silver, and calcium were homogeneously distributed in both pure samples. As a result of the analysis, characteristic peaks are observed in the energy levels of Ca, Ag, and P elements.

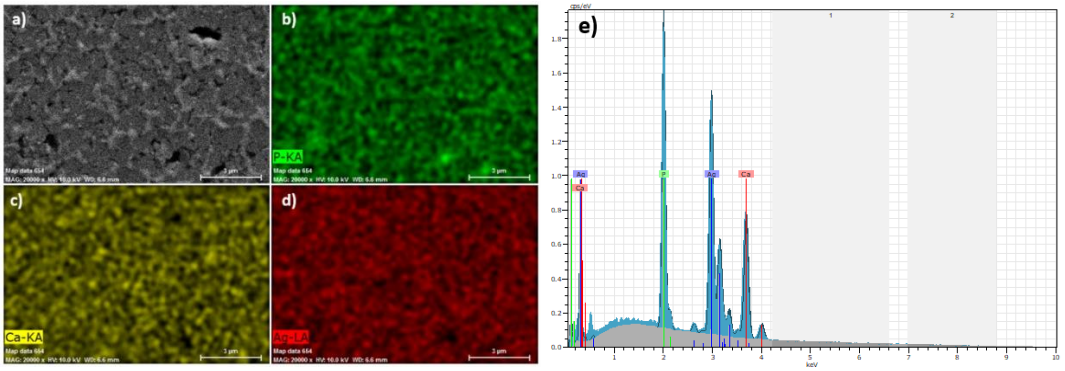


Figure 5.9: a) SEM image of sample $Ca_{0.95}$ $Ag_{0.90}P$, elemental mapping of b) P, c) Ca , d) Ag , and e) EDS spectra of $Ca_{0.95}$ $Ag_{0.90}P$.

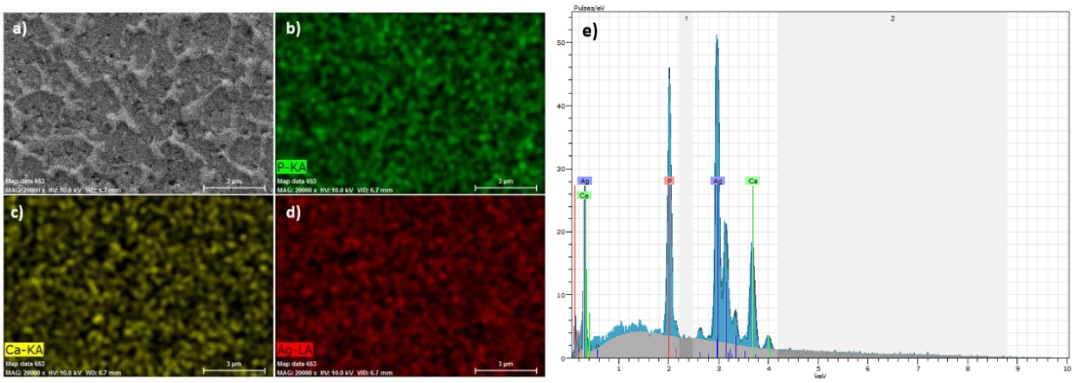


Figure 5.10: a) SEM image of sample $CaAg_{0.90}P$-Annealing, elemental mapping of b) P, c) Ca , d) Ag , and e) EDS spectra of $CaAg_{0.90}P$-Annealing.

SEM images of nano boron doped samples are shown in Figure 5.11. While the SEM pictures of all three samples are similar, $Ca_{0.95}Ag_{0.90}P\text{-}B_{0.05}$ and $CaAg_{0.90}P\text{-}B_{0.1}$ have bigger pores in the structures. When the nano boron doped materials are analyzed using EDX, homogeneously distributed Ca, Ag, and P elements are seen, whereas the energy level of the doped B element does not exhibit a peak. Since it is a very light element, the EDS peak does not appear. All EDS and elemental image analyses of the samples are shown in Figure 5.12, Figure 5.13, and Figure 5.14, respectively.

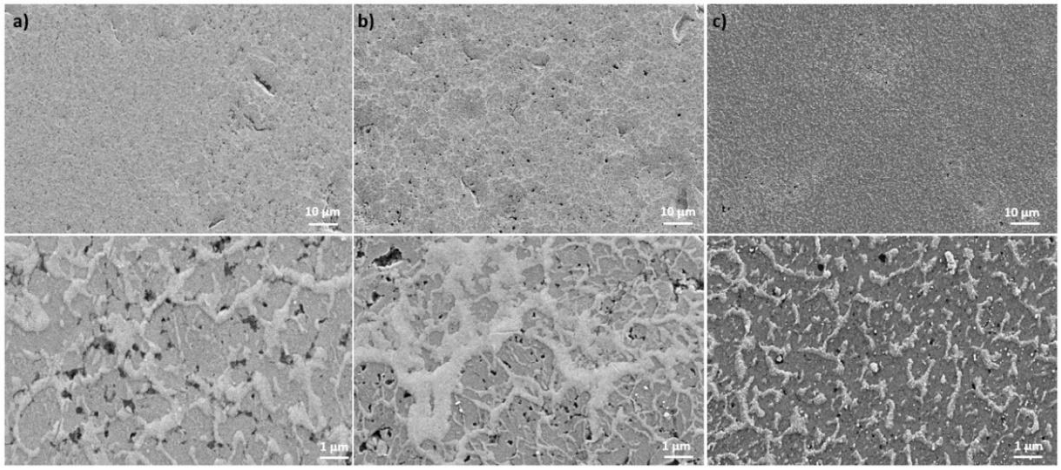


Figure 5.11: SEM images of nano boron doping samples (a) $Ca_{0.95}Ag_{0.90}P\text{-}B_{0.05}$, (b) $CaAg_{0.90}P\text{-}B_{0.1}$, (c) $CaAg_{0.90}P\text{-}B_{0.05}$.

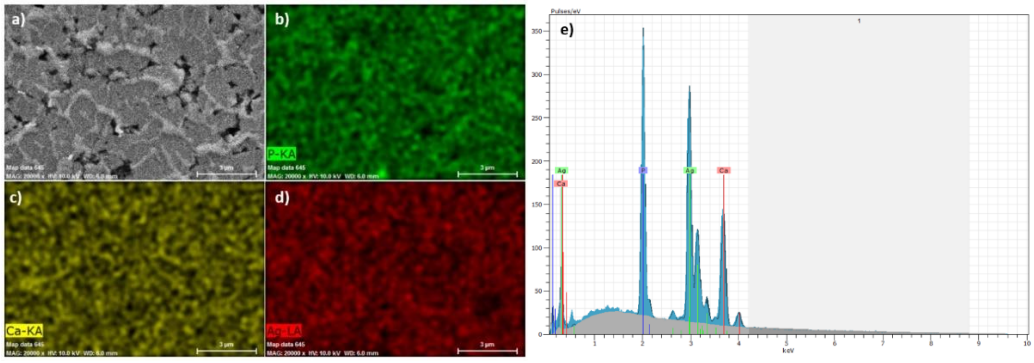


Figure 5.12: a) SEM image of nano boron doping sample $Ca_{0.95}Ag_{0.90}P\text{-}B_{0.05}$, elemental mapping of b) P, c) Ca , d) Ag , and e) EDS spectra of $Ca_{0.95}Ag_{0.90}P\text{-}B_{0.05}$.

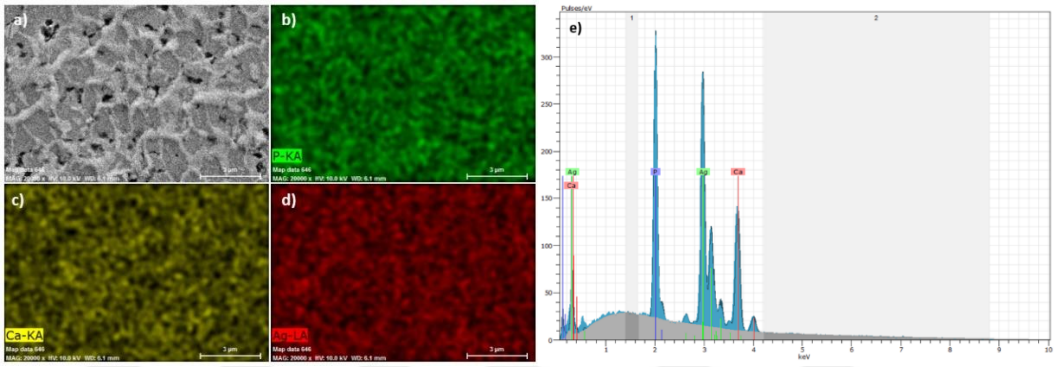


Figure 5.13: a) SEM image of nano boron doping sample $CaAg_{0.90}P\text{-}B_{0.1}$, elemental mapping of b) P, c) Ca , d) Ag , and e) EDS spectra of $CaAg_{0.90}P\text{-}B_{0.1}$.

When the EDS images (Fig. 5.14) of the 0.05 nano boron doped material by atomic weight were examined, it was determined that the silver density was high in the bright regions. Apart from this, there is a homogeneous distribution throughout the structure.

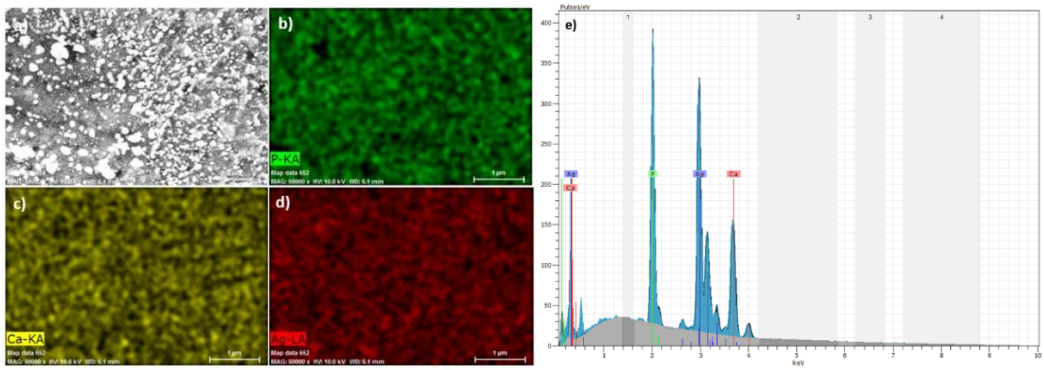


Figure 5.14: a) SEM image of nano boron doping sample $CaAg_{0.90}P\text{-}B_{0.05}$, elemental mapping of b) P, c) Ca , d) Ag , and e) EDS spectra of $CaAg_{0.90}P\text{-}B_{0.05}$.

SEM images of Na doped sample are shown in Figure 5.15. The porous microstructure is apparent in the black regions of the SEM pictures. Figure 5.16 illustrates the results of EDX study performed on Na doped sample to ensure material homogeneity. Phosphorus, silver, and calcium are spread uniformly, as evidenced by the EDS elemental mapping. As a result of the EDS analysis, in addition to the Ca, Ag, and P elements, a peak in the energy level of the Na element is noticed, and it is found that it is distributed throughout the microstructure (Figure 5.16).

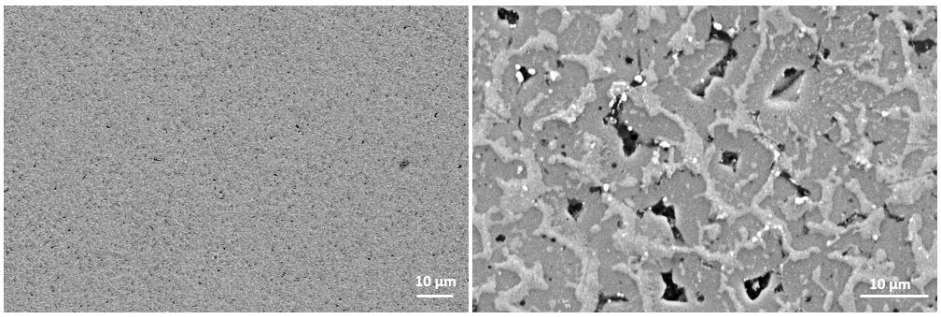


Figure 5.15: SEM images of $Ca_{0.95}Ag_{0.90}P\text{-}Na_{0.05}$ sample in different magnifications.

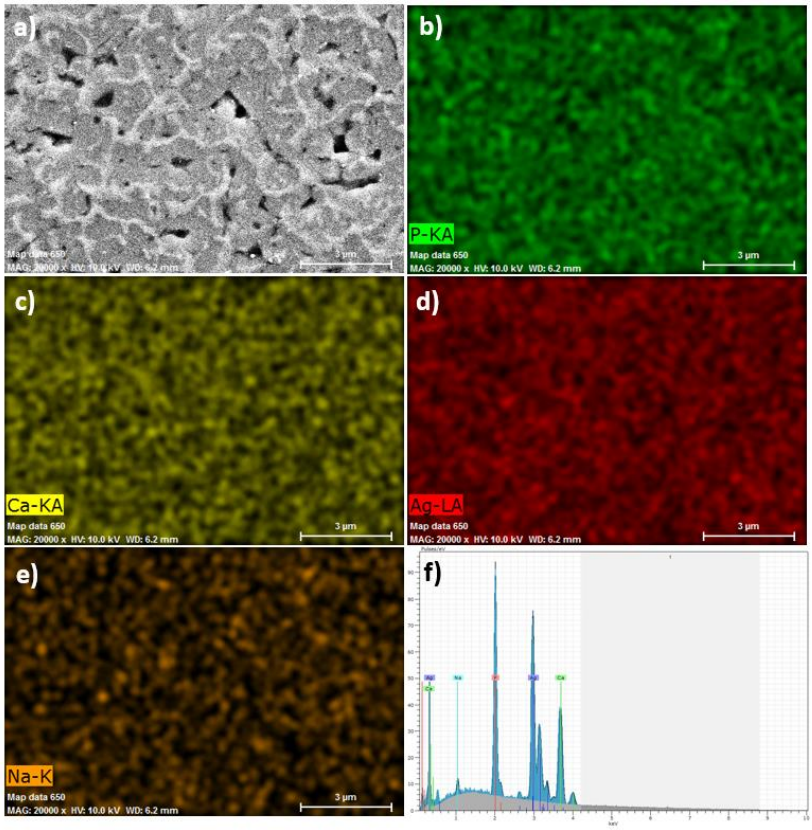


Figure 5.16: a) SEM image of Na doping sample $Ca_{0.95}$ $Ag_{0.90}P\text{-}Na_{0.05}$, elemental mapping of b) P, c) Ca ,d) Ag , e) Na, and f) EDS spectra of $Ca_{0.95}$ $Ag_{0.90}P\text{-}Na_{0.05}$.

SEM images of $CaAgP_{0.90}$-$Zn_{0.1}$ and $CaAgP_{0.90}$-$Zn_{0.1}$-Annealing samples are given in Figure 5.17. $CaAgP_{0.90}$-$Zn_{0.1}$-Annealing has a more uniformly dispersed porous structure due to the combination of high temperature and long time.

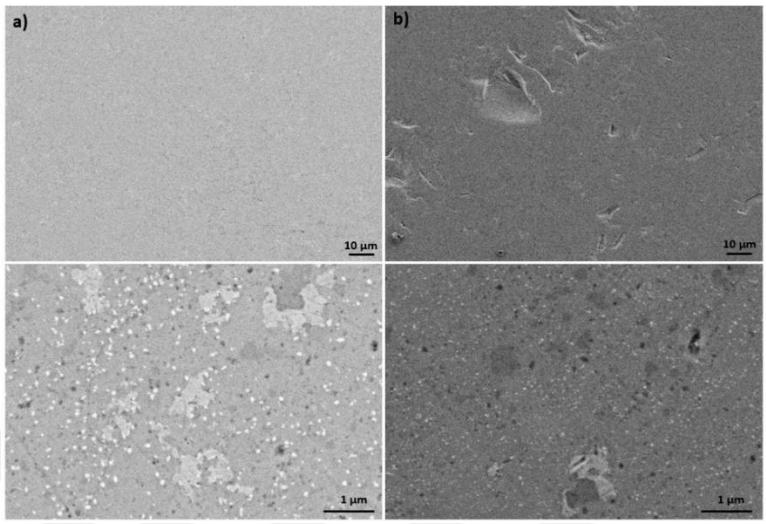


Figure 5.17: SEM images of (a) $CaAg_{0.90}P$-$Zn_{0.1}$ sample with a magnified image given below, (b) SEM images of $CaAg_{0.90}P$-$Zn_{0.1}$ Annealing sample with a magnified image given below.

Figure 5.18 indicates the SEM images of the $CaAgP_{0.90}$-$Zn_{0.1}$ sample and the energy levels of the elements. While the bright phases seen in Figure 5.18b indicate the peak in the energy level of the element Ag, the darker regions seen in Figure 5.18c represent the peaks in the energy level of the element Zn. Calcium and phosphorus elements are uniformly distributed throughout the structure. When the EDS images (Figure 5.19) of the 0.1 zinc doped with annealing material by atomic weight, it was seen that the bright areas exhibited high silver density. EDS elemental mapping shows a homogeneous distribution of phosphorus and calcium. According to EDS analysis, it is observed that the element Zn spreads throughout the microstructure and exhibits a peak in energy level in addition to the elements Ca, Ag, and P.

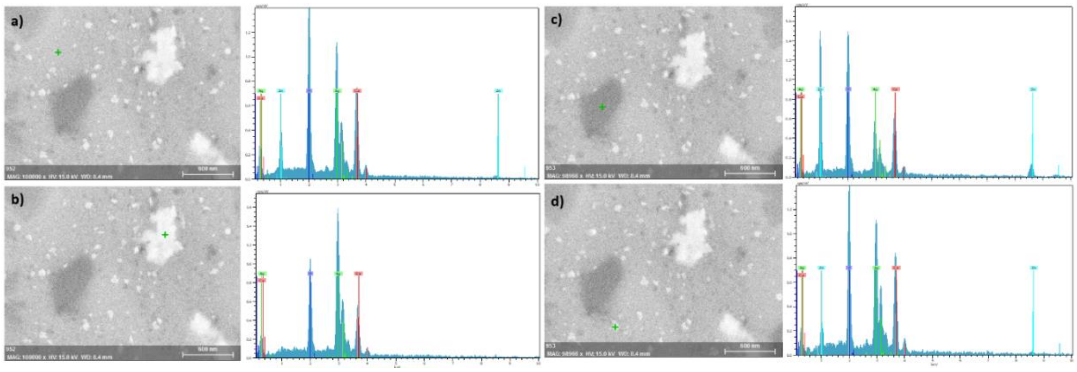


Figure 5.18: SEM image and EDS spectra of sample $CaAg_{0.90}P\text{-}Zn_{0.1}$ for each element.

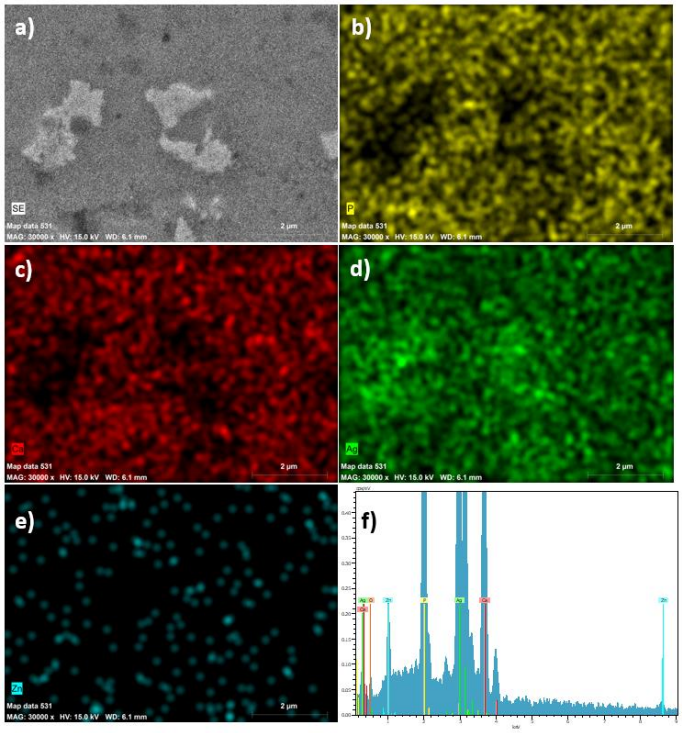


Figure 5.19: a) SEM image of Zn doping sample $CaAg_{0.90}P\text{-}Zn_{0.1}$ Annealing, elemental mapping of b) P, c) Ca , d) Ag , e) Zn, and f) EDS spectra of $CaAg_{0.90}P\text{-}Zn_{0.1}$ Annealing.

SEM images of the $Ca_{0.95}Ag_{0.90}P\text{-}La_{0.05}$ sample after SPS and annealing are illustrated in Figure 5.20. When comparing the two samples, it was noticed that the pores decreased after annealing. Upon examining the EDS data, the presence of the La element is not detected in the sample following SPS. This suggests that calcium was replaced with the element La through effective doping (Figure 5.21). However, when EDS was examined after annealing, La element was found in the microstructure. Moreover, it was observed

that silver elements precipitated in some bright areas and created inhomogeneous regions in the annealing sample (Figure 5.22d).

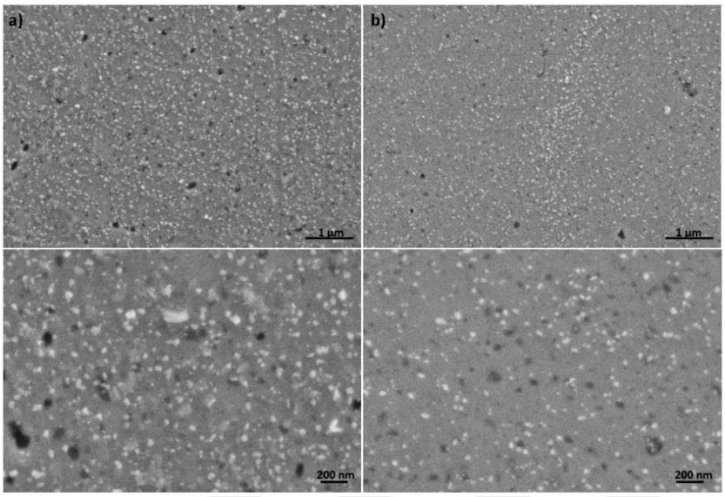


Figure 5.20: SEM images of (a) $Ca_{0.95}Ag_{0.90}P\text{-}La_{0.05}$ sample with a magnified image, (b) SEM images of $Ca_{0.95}Ag_{0.90}P\text{-}La_{0.05}$ Annealing sample with a magnified image.

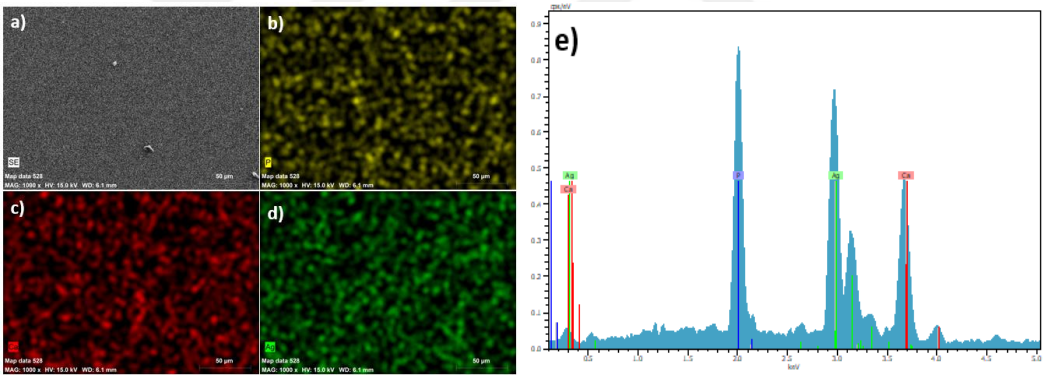


Figure 5.21: a) SEM image of La doping sample $Ca_{0.95}Ag_{0.90}P\text{-}La_{0.05}$, elemental mapping of b) P, c) Ca , d) Ag , e) EDS spectra of $Ca_{0.95}Ag_{0.90}P\text{-}La_{0.05}$.

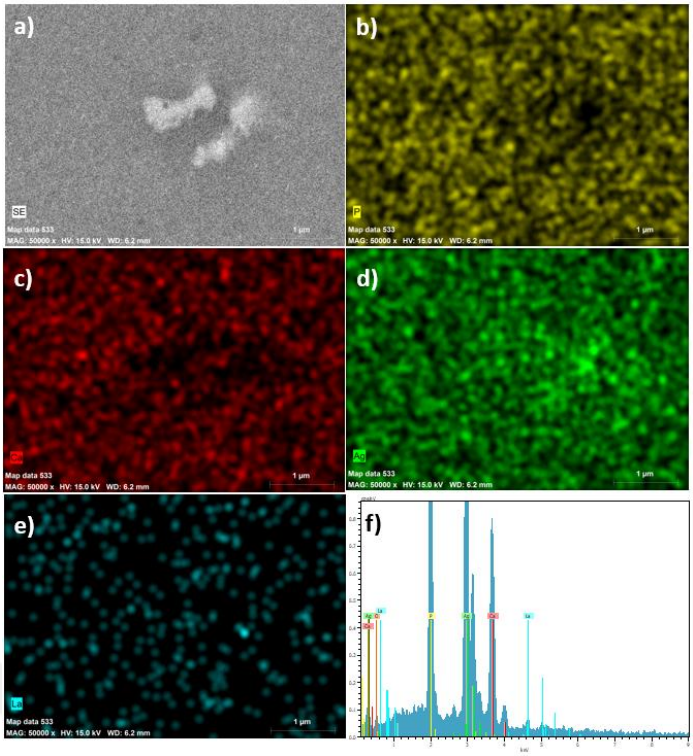


Figure 5.22: a) SEM image of La doping sample $Ca_{0.95}Ag_{0.90}P\text{-}La_{0.05}$-Annealing, elemental mapping of b) P, c) Ca , d) Ag , e) EDS spectra of $Ca_{0.95}Ag_{0.90}P\text{-}La_{0.05}$-Annealing.

Figure 5.23 displays SEM pictures of the Sn-doped sample. The porous microstructure is visible in the dark areas of the SEM images. Figure 5.24 illustrates the findings of an EDX analysis conducted on a tin-doped sample to verify material uniformity. Phosphorus, silver, and calcium elements are uniform in the sample, with peaks indicating their energy levels. The energy levels of the tin element are detected in the light-colored areas (Figure 5.24b).

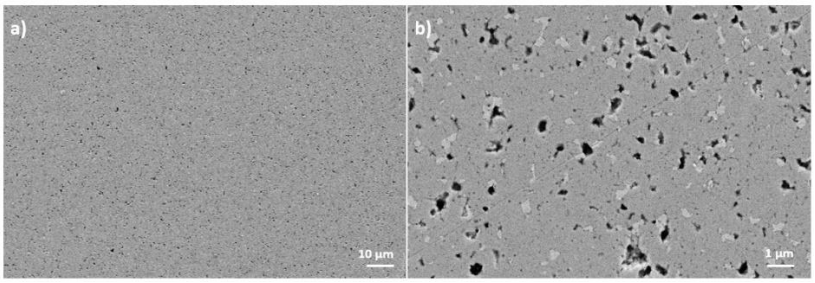


Figure 5.23: SEM images of $CaAg_{0.90}P\text{-}Sn_{0.05}$ sample in different magnifications.

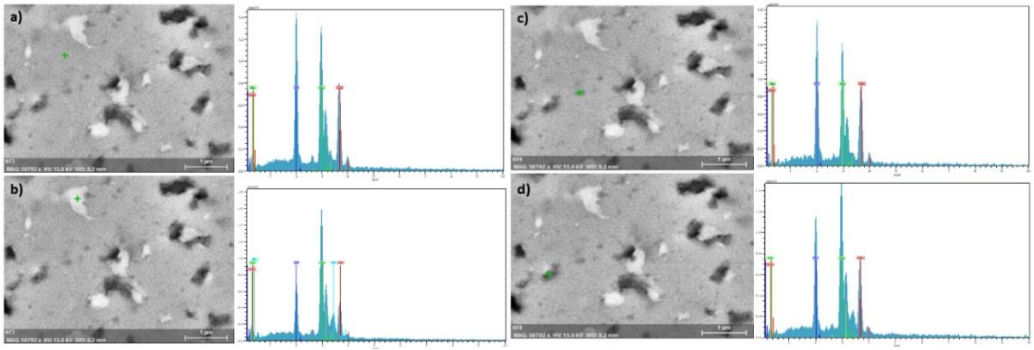


Figure 5.24: SEM image and EDS spectra of sample $CaAg_{0.90}P\text{-}Sn_{0.05}$ for each element.

### *5.1.4 Transport Property Analysis*

An in-depth examination of thermoelectric efficiency was carried out on samples produced by the high-energy ball-mill process and pressed using the SPS method. Measurements of all thermoelectric parameters were made up to 823 K. The methodology for all sample preparations and measurement processes is detailed in Chapter 4. All measurements were consistently done following these descriptions.

The thermoelectric results for undoped and intrinsic doping CaAgP compound samples were given in the same figure. Figure 5.25a shows that the electrical resistivity of all samples increases slightly with increasing temperature up to 823 K. This indicates that the materials are heavily doped semiconductors. The $CaAg_{0.90}P$ sample exhibits the highest electrical resistivity and the lowest thermal conductivity. In addition to this, a reduction in electrical conductivity will also result in a decrease in the electronic component of heat conductivity. Therefore, the decrease in thermal conductivity is due to the decrease in electronic thermal conductivity rather than lattice thermal conductivity. This is a compelling example of how the interdependence of transport characteristics presents a challenge to optimize the figure of merit (zT). Compared with the $CaAg_{0.90}P$ sample, an improvement in the resistivity value of the other intrinsic doping samples was observed. The expected decrease in electrical resistance after heat treatment was achieved for sample $CaAg_{0.90}P$-Annealing. Since the Seebeck coefficients of all samples increase with temperature and the Seebeck coefficients of the samples are quite high, they can be considered to have heavily doped semiconductor behavior. All samples have an almost linearly increasing *S(T)* up to 800K, which is expected for highly doped semiconductors. For samples $CaAg_{0.90}P$-Annealing (MA20) and $CaAg_{0.95}P$ (MA10), *S(T)* approaches a

plateau above this temperature, indicating the beginning of minority carrier conduction. Furthermore, the Seebeck values are positive, indicating that all samples are p-type materials. The value of both Seebeck and electrical resistivity are higher in $CaAg_{0.90}P$, indicating that this sample is less p-type doped, despite the main phase having the same composition in all samples. Thermal conductivity for all samples decreases with increasing temperature because of the phonon-phonon scattering (Umklapp scattering) [42]. There may be an excessive number of phonons produced as the temperature increases, and these phonons may interact with each other. Since their movement and heat transfer are prevented, their thermal conductivity decreases. The phonon mean free path is inversely related to temperature, and as temperatures increase, the Umklapp process becomes more dominant since it depends on the number of phonons [61]. As a result of examining all thermal and electrical conduction properties of these materials, the values in Figure (5.25d) were found by calculating the thermoelectric efficiency zT. The thermoelectric coefficient of performance of the material is calculated using equation 2.1 as mentioned in the previous chapter. Thanks to the relatively higher increase in the absolute value of the Seebeck coefficient and the relatively lower values in the thermal conductivity, the zT value of the $CaAg_{0.90}P$ material, which contains 90% silver by mass, was calculated as 0.33 at 823 Kelvin. This value is considered promising for phosphide thermoelectric materials. When the zT results for undoped and intrinsic doped specimens are evaluated, it is observed that $CaAg_{0.90}P$ has the highest zT value among these samples.

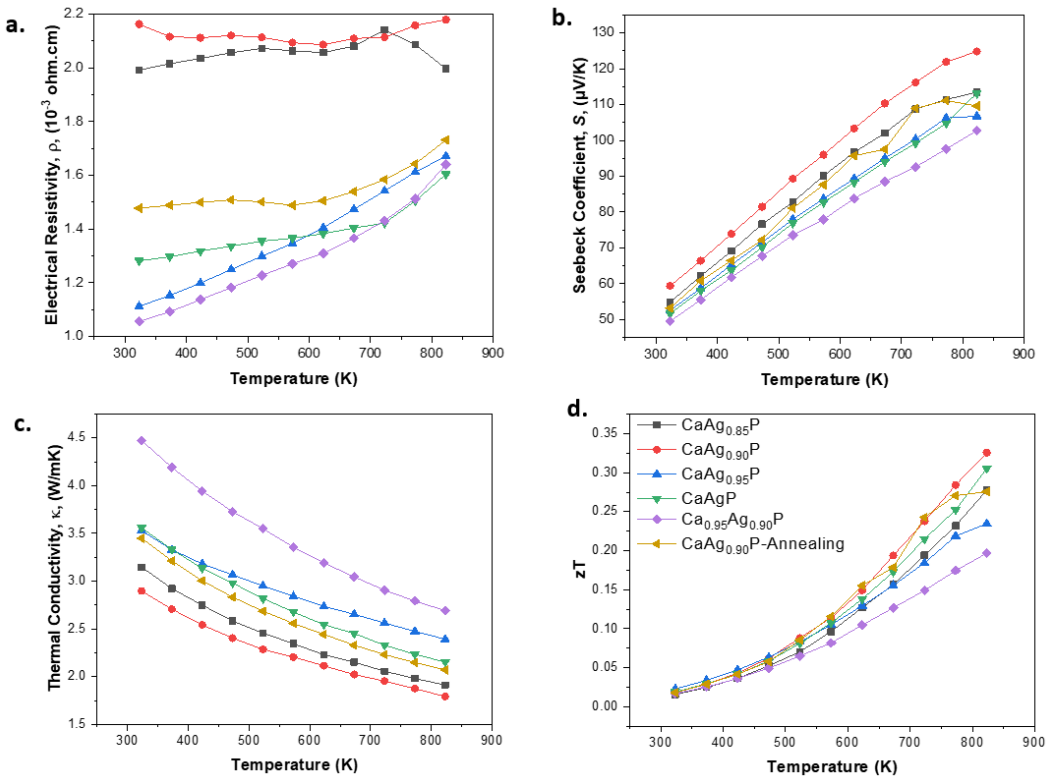


Figure 5.25: a) Electrical Resistivity, b) Seebeck coefficient, c) Thermal conductivity, d) zT values of CaAgP, $CaAg_{0.95}P$, $CaAg_{0.90}P$, $CaAg_{0.85}P$, $Ca_{0.95}Ag_{0.90}P$, $CaAg_{0.90}P$-Annealing.

Figure 5.26 shows the thermoelectric graphs of the samples synthesized with doped elements. According to the graph, there was no noticeable decrease in the electrical resistivity values of the doping elements compared to the undoped compounds. Even the resistivity values of Zn-doped and La-doped samples increased significantly. Although the expected results were not achieved in electrical resistivity measurements, the values of the Zn-doped and La-doped samples improved after annealing displaying degenerate semiconductor behavior. Also, samples with Sn doping showed the same trend as the undoped sample. La-doped materials exhibit a decrease in resistivity with increasing temperature. This suggests the samples have characteristics of semiconductors. All Seebeck values are positive, indicating a p-type character, and show an increasing trend with temperature. However, for samples $Ca_{0.95}Ag_{0.90}P$-$La_{0.05}$ and $Ca_{0.95}Ag_{0.90}P$-$La_{0.75}$, there was a decline within a certain temperature range. Compared to the undoped sample, there was a significant increase in the Seebeck values of the 0.1 at.% nano boron-doped, Zn-doped, and La-doped samples. This should be related to decreased p-type (hole) carrier concentration upon adding excess electrons due to such dopants. In addition,

Equation 2.5 explains how the inclusion of doping elements and decreased carrier concentration resulting from secondary phase development and interfaces enhance the Seebeck coefficient [62]. The thermal conductivity graph indicates a decreasing behavior with temperature, as in the undoped and intrinsic doped samples. A promising trend was seen in the B-, Zn, and La-doped samples displaying distinctly lower thermal conductivity than the pristine sample. After annealing, grain growth and reduction in grain boundaries occur. Increasing grain sizes also causes an increase in thermal conductivity, as it reduces mechanisms such as phonon scattering [63]. Therefore, it can be observed that the thermal conductivity values of annealed samples are slightly higher than those of unannealed samples. Among the compounds of doped elements, the $Ca_{0.95}Ag_{0.90}P$-$La_{0.05}$ annealing sample indicated the highest zT value of 0.27 at a temperature of 773 Kelvin. While the La-doped sample exceeded the undoped sample in zT values at a large temperature range, the intrinsically doped $CaAg_{0.90}P$ sample had the highest zT value of around 0.33 at 823 K. As seen in Figure 5.26, different dopants added to the CaAgP compound did not increase the zT values. Even though there was an increase in the Seebeck coefficient in the doped samples due to no significant decreases in the thermal conductivity and electrical resistivity values, these results were more dominant and there was no improvement in the zT value. Upon comparing the zT results with previous experimental research, it was found that our study yielded a lower zT value than prior studies. In one of these studies, CaAgP peaked at zT 0.32 at 800K, while $CaAg_{0.90}P$ peaked at zT 0.43 at 660K and with zT=0.38 at 800K [43]. The $CaAg_{0.90}P$ material obtained in this study also has values that are very close to this and is promising for its development in future studies.

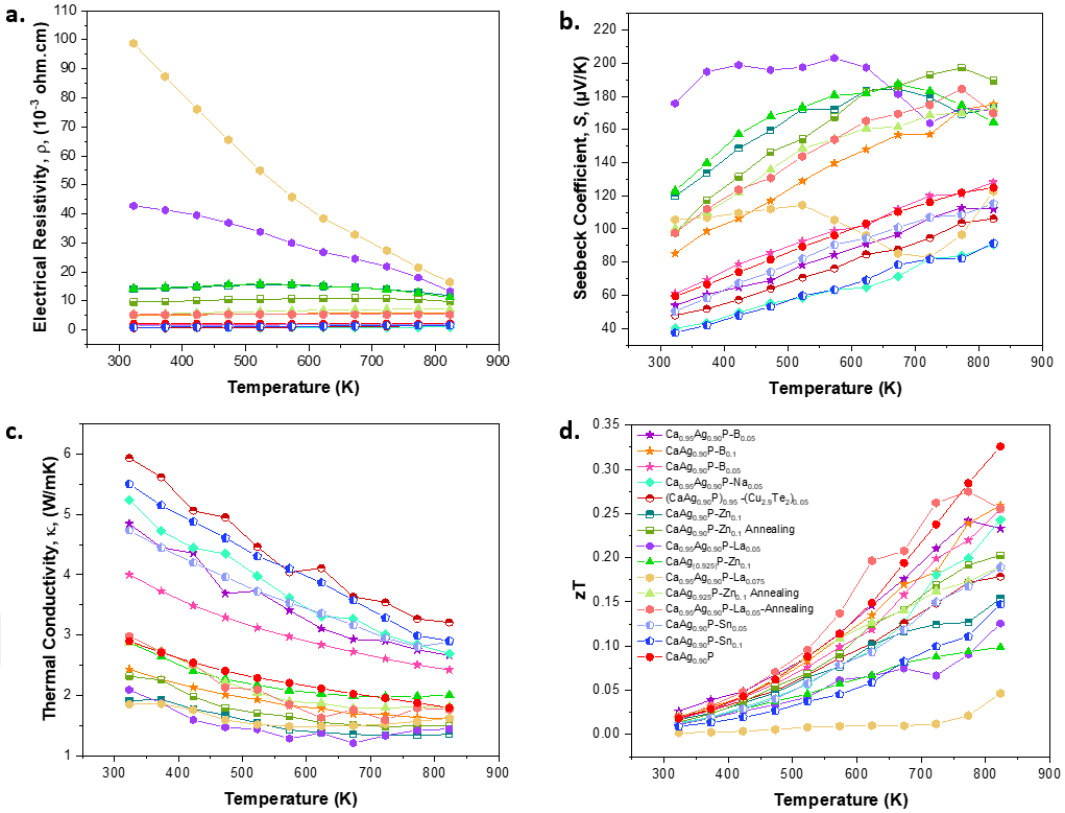


Figure 5.26: a) Electrical Resistivity, b) Seebeck coefficient, c) Thermal conductivity, d) zT values of different dopants of CaAgP samples.

### *5.1.5 Mechanical Property Measurements*

Shimadzu HMV-G Series Micro Vickers Hardness Tester was used to measure the hardness of the materials. During the analysis, a load of 0.01HV (98.07 mN) and 0.025HV (245.2 mN) were applied to the materials. To calculate the hardness of the materials, measurements were made at 10 different points from all surfaces, and the arithmetic average of these values was taken. Figures 5.27, 5.28, and 5.29 indicate the marks and diagonals left by the applied loads on the surface of the samples. In Figure 5.30, each sample's average of the Vickers hardness values is given.

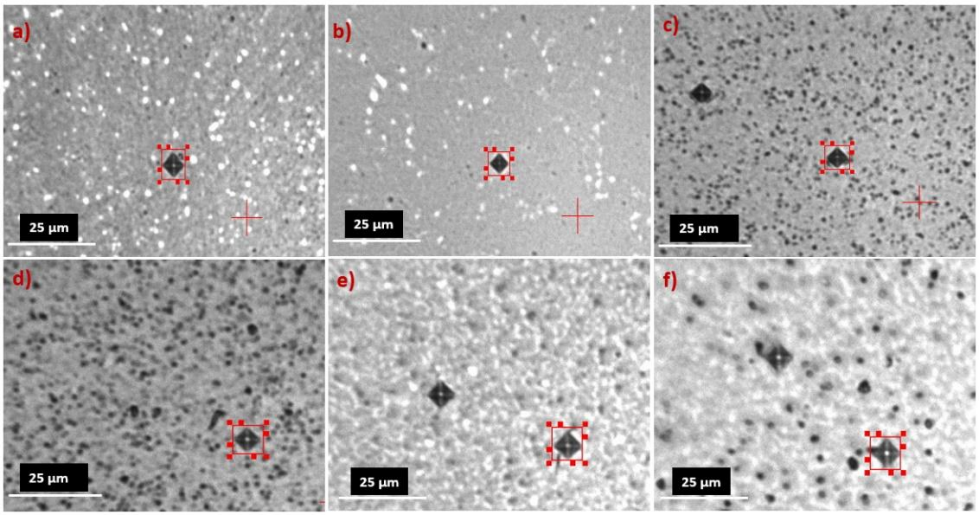


Figure 5.27: Vickers hardness analysis images of a) CaAgP, b) $CaAg_{0.95}P$, c) $CaAg_{0.90}P$, d) $CaAg_{0.85}P$, e) $Ca_{0.95}Ag_{0.90}P$, f) $CaAg_{0.90}P$-Annealing.

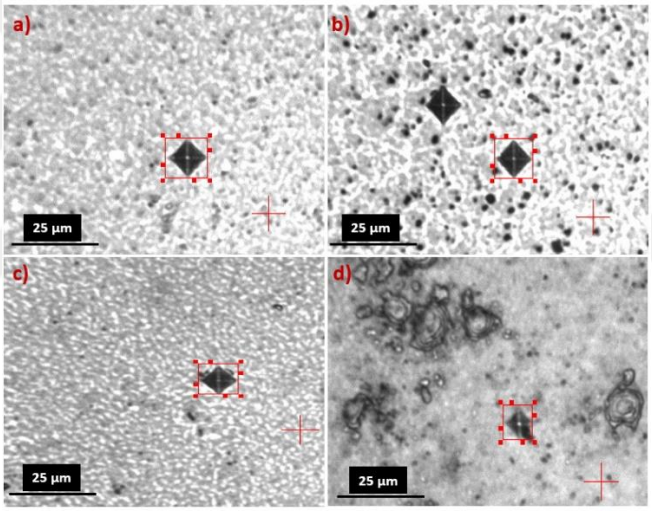


Figure 5.28: Vickers hardness analysis images of a) $Ca_{0.95}Ag_{0.90}P$-$B_{0.05}$, b) $CaAg_{0.90}P$-$B_{0.1}$, c) $CaAg_{0.90}P$-$B_{0.05}$, d) $Ca_{0.95}Ag_{0.90}P$-$Na_{0.05}$.

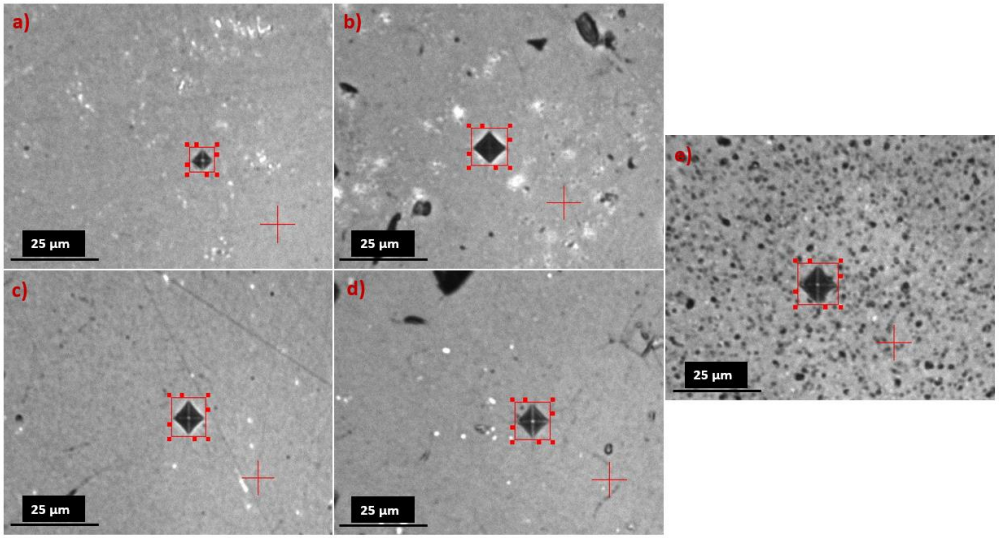


Figure 5.29: Vickers hardness analysis images of a) $CaAg_{0.90}P\text{-}Zn_{0.1}$, b) $CaAg_{0.90}P\text{-}Zn_{0.1}$ Annealing, c) $Ca_{0.95}Ag_{0.90}P\text{-}La_{0.05}$, d) $Ca_{0.95}Ag_{0.90}P\text{-}La_{0.05}$ Annealing, e) $CaAg_{0.90}P\text{-}Sn_{0.05}$.

When analyzing the impact of doping elements on hardness, the sample doped with 0.05 at.% of nano boron exhibited the maximum hardness level within the Ca-Ag-P system. The sodium doping, however, dramatically reduced the hardness value compared to the undoped and intrinsic doping samples. The hardness values are not comparable to the literature due to their absence in any prior research.

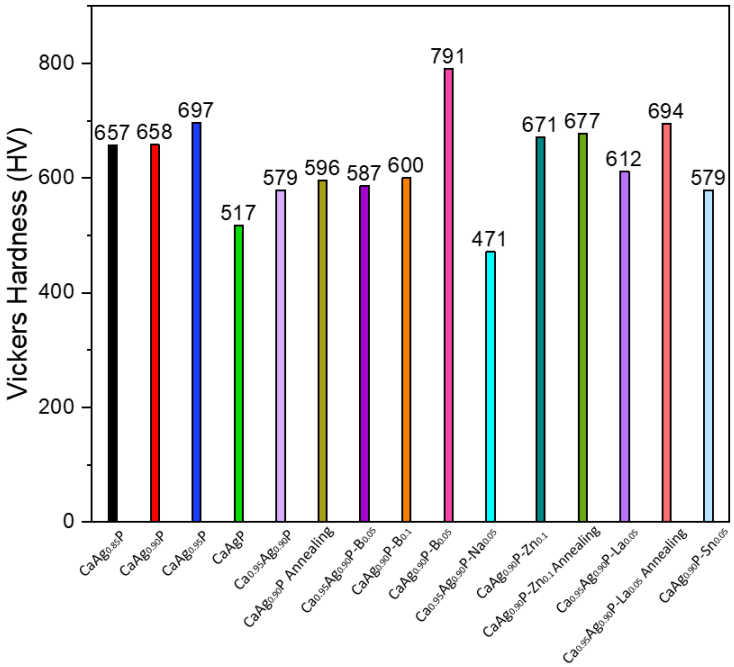


Figure 5.30: Vickers hardness values of all CaAgP samples.

## *5.2 Results of CaCuP Ternary Phosphide Phase*

### *5.2.1 Preparation*

The elements and dopants used to prepare the CaCuP compound are given in Chapter 4. CaCuP powder form was prepared by mixing the initial pieces of calcium and powder of copper and red phosphorus. The powders of zinc, pieces of lanthanum, and Nano boron at 0.1 at.% and 0.05 at.% were mixed as doping elements and then synthesized using a high-energy ball mill. The same experimental procedure was used for starting the CaCuP compound as described during CaAgP compounds and in its dopants experiments. All different compounds were prepared by changing the Cu and Ca content. The final black powder was extracted from the vial inside the glovebox. Following that, the powder was sintered using spark plasma sintering (SPS) to produce dense and strong bulk materials.

Since it has the most suitable XRD data, the sintering process was first applied to the CaCuP compound. The powders were put into a graphite die with a 10 mm inner diameter which was covered in graphite foils in a glove box separately to prepare them for spark plasma sintering. The obtained powder samples were sintered for 10 minutes at 800°C and 50 MPa pressure using the spark plasma sintering method. After this process, the pellets were removed from the graphite die and polished with 600, 800, 1000, and 1200 grit $SiO_2$ sandpapers. The thermoelectric measurements were then carried out following the XRD peaks examined.

After SPS, some polished samples were placed in glass and quartz tubes and then put into the furnace for heat treatment as in the case of CaAgP samples. Quartz wools were placed in the alumina crucible to prevent the tube from breaking during the process. The pellets were heat treated at 600 degrees for 4 days, as these were the most optimum values. When the heat treatment period was over, the quartz/glass tubes were removed from the furnace and the pellets were sanded again with sandpaper. The preparation conditions for all CaCuP samples, whether doped or undoped, including the use of spark plasma sintering (SPS) and annealing processes, are provided in Table 5.2.

Table 5.2 Preparation conditions of CaCuP ternary phosphide samples.

| Sample Name | Composition | Excess Addition | Ball Milling Time | SPS Temperature (°C) | Sps Time (minute) | Heat Treatment Temperature (°C) | Heat Treatment Duration (day) | Density ($g/cm^3$) |
|---|---|---|---|---|---|---|---|---|
| MA01 | CaCuP | - | 4h | 800 | 10 | - | - | 4.0 |
| MA24 | $CaCuP\text{-}B_{0.1}$ | 0.1 at. % nB | 4h | 800 | 10 | - | - | 3.92 |
| MA46 | $Ca_{0.90}CuP\text{-}La_{0.1}$ | 0.1 at. % La | 4h | 800 | 10 | - | - | 4,14 |
| MA47 | $Ca_{0.95}CuP\text{-}La_{0.05}$ | 0.05 at. % La | 4h | 800 | 10 | - | - | 4,06 |
| MA48 | $CaCu_{0.90}P\text{-}Zn_{0.1}$ | 0.1 at. % Zn | 4h | 800 | 10 | - | - | 3,87 |
| MA49 | $CaCu_{0.95}P\text{-}Zn_{0.05}$ | 0.05 at. % Zn | 4h | 800 | 10 | - | - | 3,89 |
| MA54 | $Ca_{0.90}CuP\text{-}La_{0.1}$ Annealing | 0.1 at. % La | 4h | 800 | 10 | 600 | 4 | 4,13 |
| MA55 | $Ca_{0.95}CuP\text{-}La_{0.05}$ Annealing | 0.05 at. % La | 4h | 800 | 10 | 600 | 4 | 4,02 |
| MA56 | $CaCu_{0.90}P\text{-}Zn_{0.1}$ Annealing | 0.1 at. % Zn | 4h | 800 | 10 | 600 | 4 | 3.85 |
| MA57 | $CaCu_{0.95}P\text{-}Zn_{0.05}$ Annealing | 0.05 at. % Zn | 4h | 800 | 10 | 600 | 4 | 3.88 |

| | | | | | | | | |
|---|---|---|---|---|---|---|---|---|
| MA62 | $Ca_{1.05}Cu_{0.95}P$-$Zn_{0.05}$ | 0.05 at. % Zn | 4h | 800 | 10 | - | - | 3.85 |
| MA63 | $CaCuP$-$Zn_{0.05}$ | 0.05 at. % Zn | 4h | 800 | 10 | - | - | 3.95 |
| MA64 | $Ca_{1.05}Cu_{0.95}P$-$Zn_{0.05}$ Annealing | 0.05 at. % Zn | 4h | 800 | 10 | 600 | - | 3.78 |
| MA65 | $Ca_{1.05}CuP$ | - | 4h | 800 | 10 | - | - | 3.73 |
| MA66 | $Ca_{1.05}CuP$ Annealing | - | 4h | 800 | 10 | 600 | 4 | 3.75 |

### *5.2.2 Crystal Structure Characterization*

XRD data for powders with all doped and undoped samples can be seen in Figure 5.31. All the main peaks from the hexagonal CaCuP structure (space group $P6_3/mmc$) matched the synthesized powder samples' XRD patterns well. However, the XRD pattern of all doping samples except the $Ca_{0.95}CuP\text{-}La_{0.05}$ and CaCuP compounds show a small amount of the secondary phase $Ca_3P_2$.

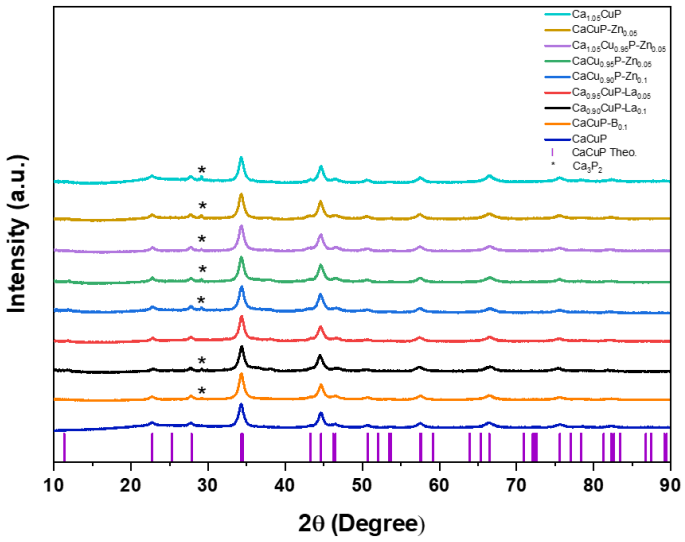


Figure 5.31: XRD patterns of CaCuP and different dopant powders.

Figure 5.32 demonstrates the XRD peaks for both undoped and nano boron-doped samples after sintering. Both samples match the theoretical peaks.

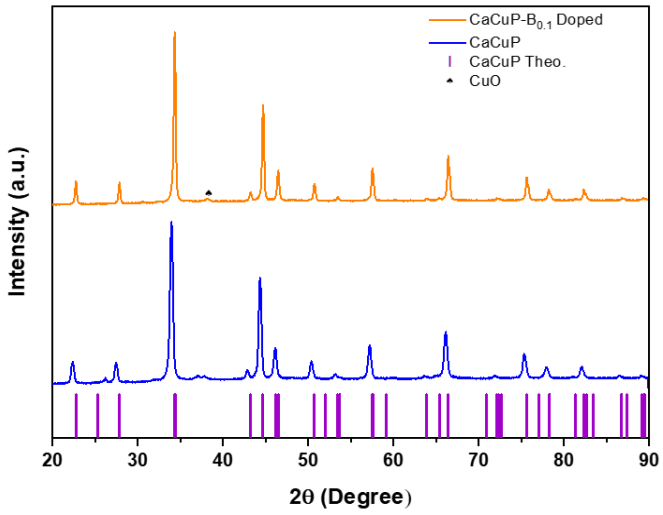


Figure 5.32: XRD patterns of CaCuP and CaCuP-$B_{0.1}$ pellets after SPS.

Figure 5.33 demonstrates the XRD peaks for both La-doped samples after sintering and annealing. Both samples match the theoretical peaks, but Ca, P elements, and CuO and $Cu_3P$ phases also appear on the XRD plot.

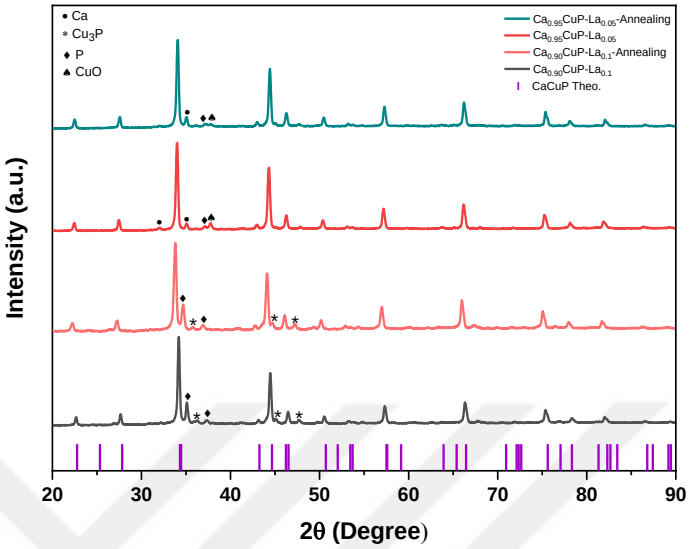


Figure 5.33: XRD patterns of $Ca_{0.95}CuP\text{-}La_{0.05}$ and $Ca_{0.90}CuP\text{-}La_{0.1}$ pellets after SPS and Annealing.

Figure 5.34 displays the XRD results of $Zn_{0.05}$ and $Zn_{0.1}$ doped materials in both SPS and annealed samples. The theoretical CaCuP peaks match, but the phosphorus element and CuO phase are seen in all samples. Figure 5.35 displays the XRD data of the $CaCuP\text{-}Zn_{0.05}$ and $Ca_{1.05}Cu_{0.95}P\text{-}Zn_{0.05}$ samples following SPS and annealing. While a second CaO phase is detected in the $Ca_{1.05}Cu_{0.95}P\text{-}Zn_{0.05}$ sample, phosphorus, and CuO phases are observed in the $CaCuP\text{-}Zn_{0.05}$ sample.

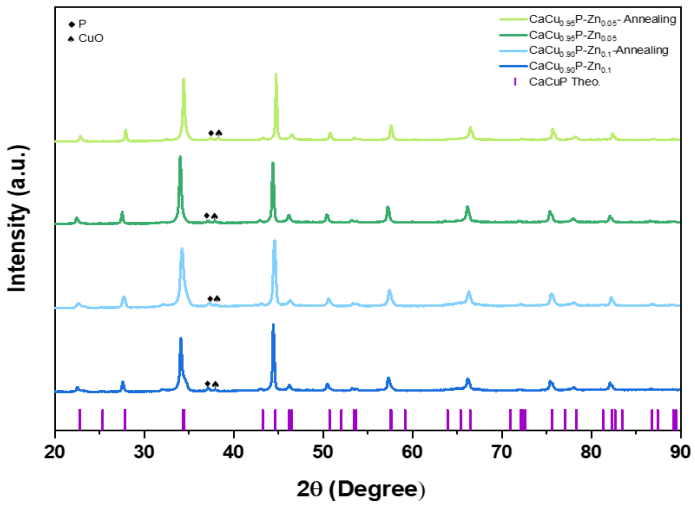


Figure 5.34: XRD patterns of $CaCu_{0.95}P\text{-}Zn_{0.05}$ and $CaCu_{0.90}P\text{-}Zn_{0.1}$ pellets after SPS and Annealing.

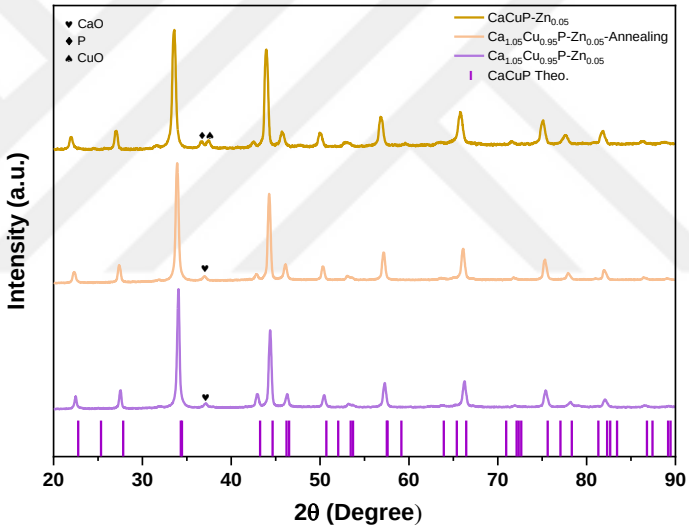


Figure 5.35: XRD patterns of $CaCuP\text{-}Zn_{0.05}$ and $Ca_{1.05}Cu_{0.95}P\text{-}Zn_{0.05}$ pellets after SPS and Annealing.

Figure 5.36 indicates the XRD results of the undoped CaCuP and intrinsic doping $Ca_{1.05}CuP$ samples. CaO is identified as the secondary phase in samples synthesized with excess calcium, also the samples match the theoretical peaks. Furthermore, phosphorus is detected in the annealed sample in addition to CaO phase.

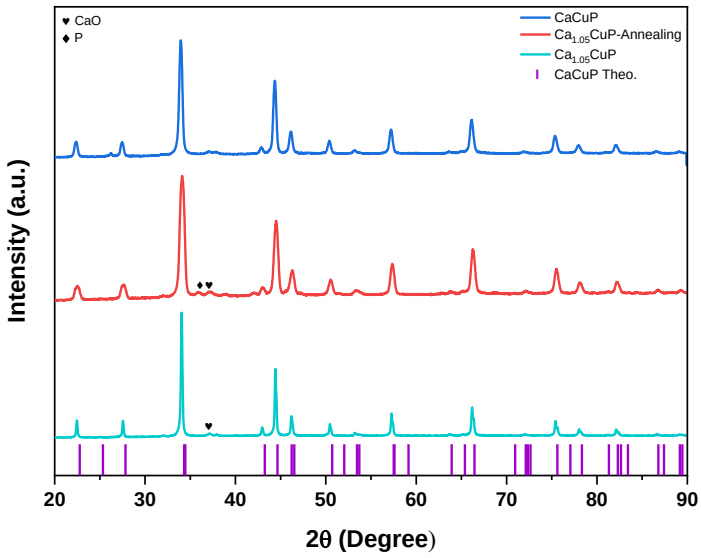


Figure 5.36: XRD patterns of CaCuP after sintering and $Ca_{1.05}CuP$ pellets after sintering and annealing.

### *5.2.3 Chemical and Microstructure Characterization*

Figure 5.37 demonstrates the results of an EDX analysis performed on pellet samples to verify material homogeneity. As it is seen from the EDS elemental mapping P (phosphorus), Cu (copper), and Ca (calcium) are distributed almost homogeneously. There were also some Ca deficiencies, some Cu excess, and possibly some phosphides on the elemental mapping images.

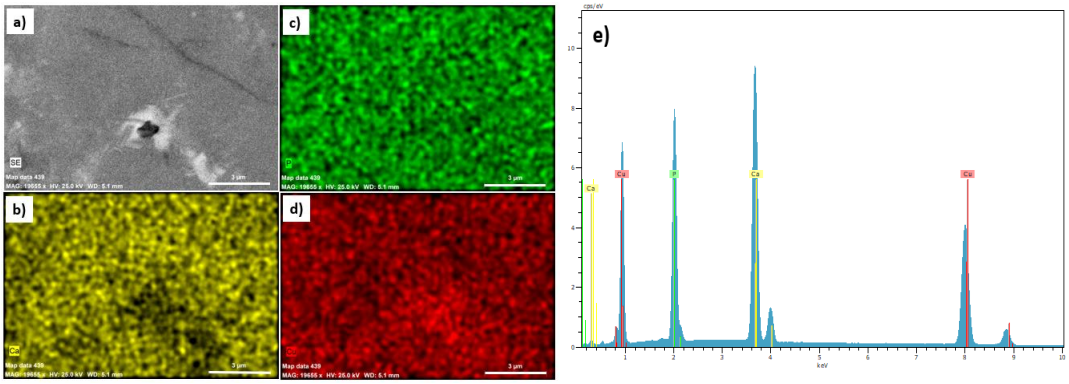


Figure 5.37: a) SEM image of sample CaCuP , elemental mapping of b) Ca , c) P , d) Cu , and e) EDS spectra of CaCuP.

Figure 5.38 illustrates SEM pictures of nano B-doped sample. The porous microstructure is visible in the black areas of the SEM images. Figure 5.39 demonstrates

the results of an EDX study carried out on a pellet-doped sample in order to confirm material homogeneity. According to the EDS elemental mapping, P (phosphorus), Cu (copper), and Ca (calcium) are dispersed quite uniformly. However, it was observed that phosphorus elements precipitated in some dark areas and created inhomogeneous regions.

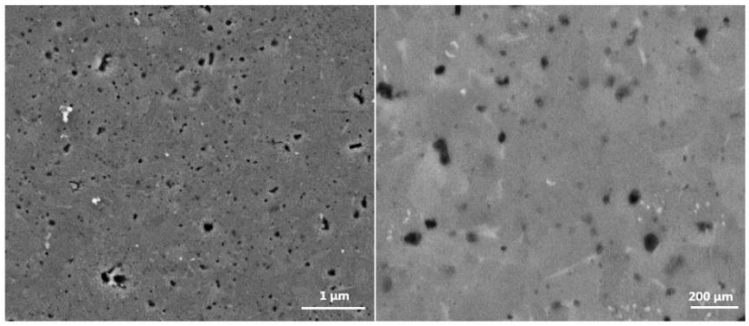


Figure 5.38: SEM images of CaCuP-$B_{0.1}$ sample in different magnifications.

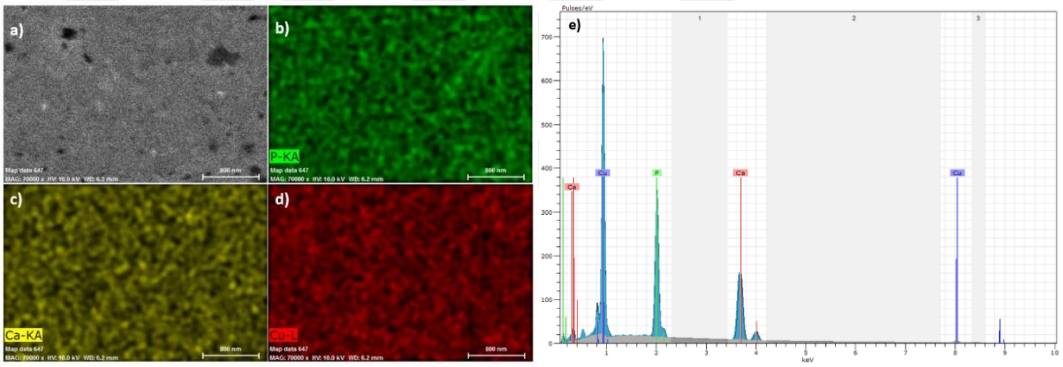


Figure 5.39: a) SEM image of nano boron doping sample CaCuP-$B_{0.1}$, elemental mapping of b) P, c) Ca , d) Cu , and e) EDS spectra of CaCuP-$B_{0.1}$.

Figure 5.40 illustrates SEM pictures of doping samples of $Ca_{0.95}$CuP-$La_{0.05}$ and after its annealing. The porous microstructure is seen in the dark regions of the SEM pictures and annealing resulted in a reduction of the pore structure in the sample. Lanthanum element is detected in the brightly colored areas, as seen in Figure 5.41a. Moreover, The EDS elemental mapping shows that phosphorus (P), copper (Cu), and calcium (Ca) are uniformly distributed in the main phase.

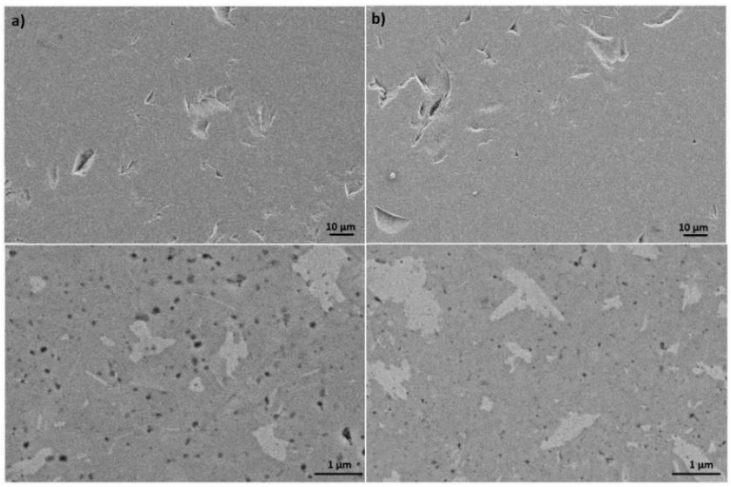


Figure 5.40: SEM images of (a) $Ca_{0.95}CuP\text{-}La_{0.05}$ sample with a magnified image, (b) SEM images of $Ca_{0.95}CuP\text{-}La_{0.05}$ Annealing sample with a magnified image.

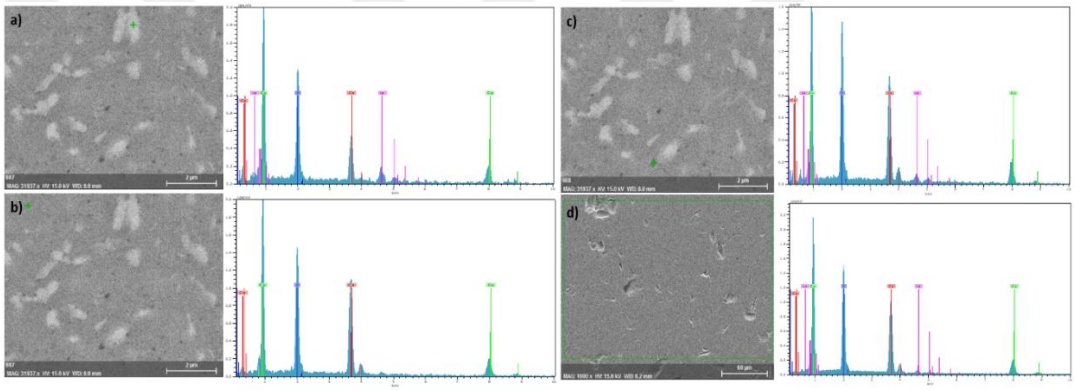


Figure 5.41: SEM image and EDS spectra of sample $Ca_{0.95}CuP\text{-}La_{0.05}$ for each element.

As is seen from the EDS elemental mapping in Figure 5.42, P (phosphorus), Cu (copper), and Ca (calcium) are distributed almost homogeneously. There are also some Ca deficiencies, possibly some Cu and some La excess in bright regions on the elemental mapping images.

SEM images of the $CaCu_{0.95}P\text{-}Zn_{0.05}$ sample after SPS and annealing are displayed in Figure 5.43. It is seen that the number of pores in the sample decreases following annealing. Figures 5.44 and 5.45 display EDS pictures of the samples analyzed following Zn-doped SPS and annealing. Both samples contain the elements Ca, Cu, P, and Zn. The elements are distributed equally in the EDS sample obtained after SPS. While the Zn element is not visible in the brighter regions of the sample examined after annealing, this

element is found in the main phase. While the Zn element is not visible in the bright regions of the sample examined after annealing, this element is found in the main phase.

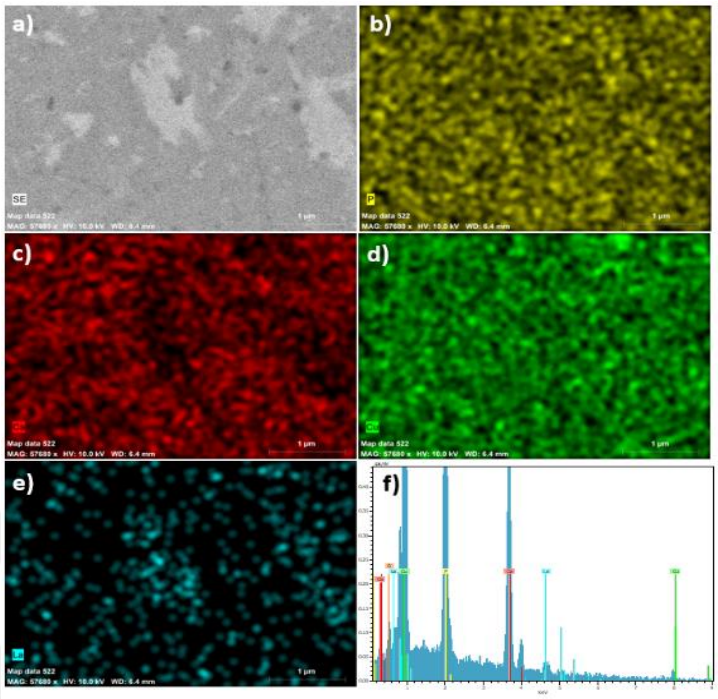


Figure 5.42: a) SEM image of La doping sample $Ca_{0.95}CuP\text{-}La_{0.05}$ Annealing, elemental mapping of b) P, c) Ca , d) Cu , e) La, and f) EDS spectra of $Ca_{0.95}CuP\text{-}La_{0.05}$ Annealing.

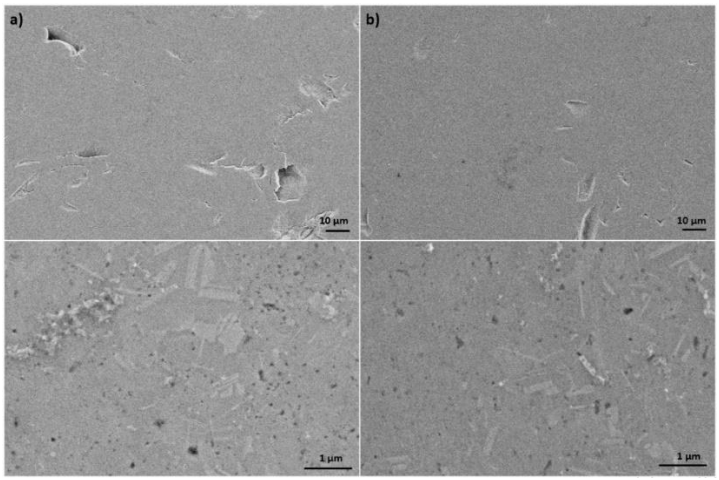


Figure 5.43: SEM images of (a) $CaCu_{0.95}P\text{-}Zn_{0.05}$ sample with a magnified image, (b) SEM images of $CaCu_{0.95}P\text{-}Zn_{0.05}$ Annealing sample with a magnified image.

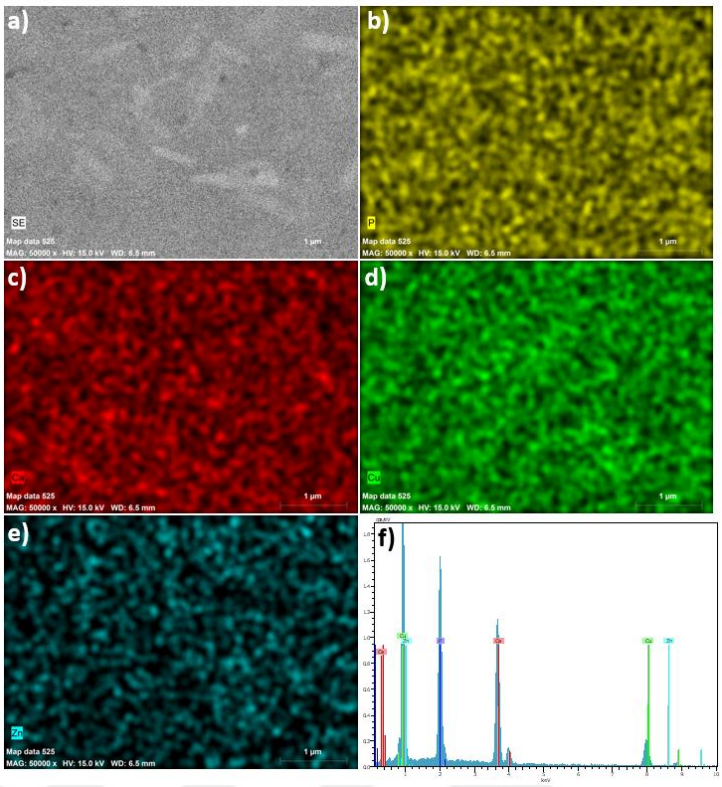


Figure 5.44: a) SEM image of Zn doping sample $CaCu_{0.95}P\text{-}Zn_{0.05}$, elemental mapping of b) P, c) Ca , d) Cu , e) Zn, and f) EDS spectra of $CaCu_{0.95}P\text{-}Zn_{0.05}$.

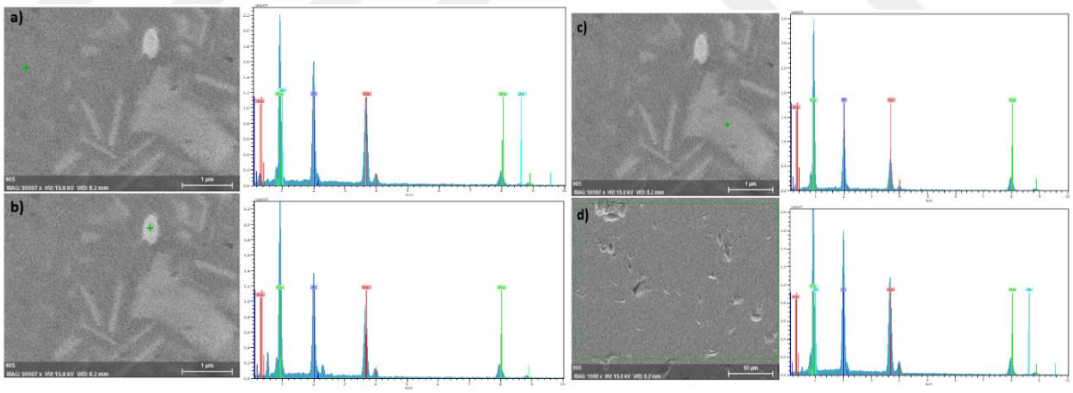


Figure 5.45: SEM image and EDS spectra of sample $CaCu_{0.95}P\text{-}Zn_{0.05}$ Annealing for each element.

Figure 5.46 illustrates the SEM pictures of the $Ca_{1.05}Cu_{0.95}P\text{-}Zn_{0.05}$ sample analyzed after SPS and annealing. Although the number of pores is low after SPS, their size increases after annealing. In addition, an alteration is observed in the sample's microstructure upon annealing. The SEM and EDS pictures in Figure 5.47 show the detection of the Zn element in the dark-colored small regions, indicating the presence of

secondary phases in the bright-colored regions. After annealing, Zn accumulation is detected in the brighter regions of the sample, as illustrated in Figure 5.48-a.

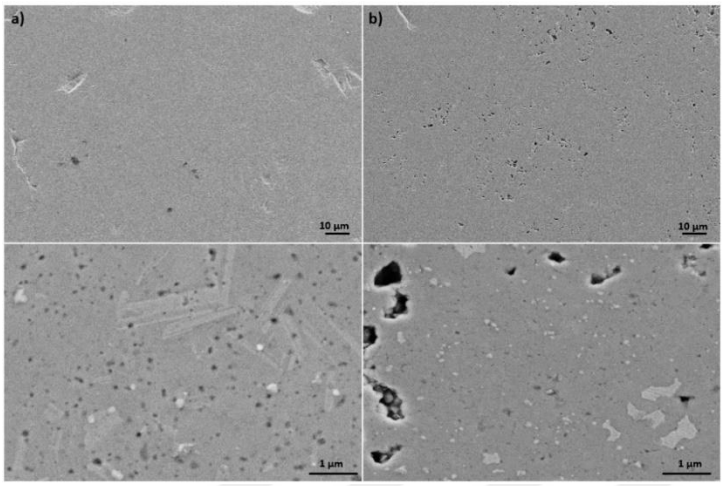


Figure 5.46: SEM images of (a) $Ca_{1.05}Cu_{0.95}P\text{-}Zn_{0.05}$ sample with a magnified image, (b) SEM images of $Ca_{1.05}Cu_{0.95}P\text{-}Zn_{0.05}$ Annealing sample with a magnified image.

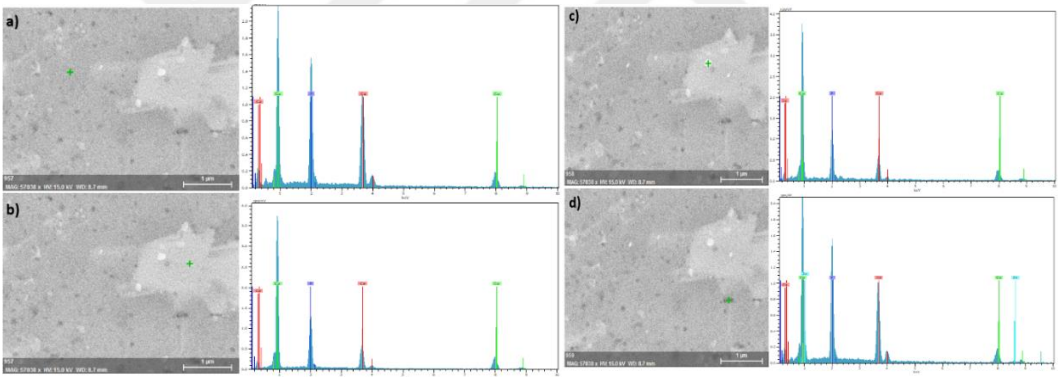


Figure 5.47: SEM image and EDS spectra of sample $Ca_{1.05}Cu_{0.95}P\text{-}Zn_{0.05}$ for each element.

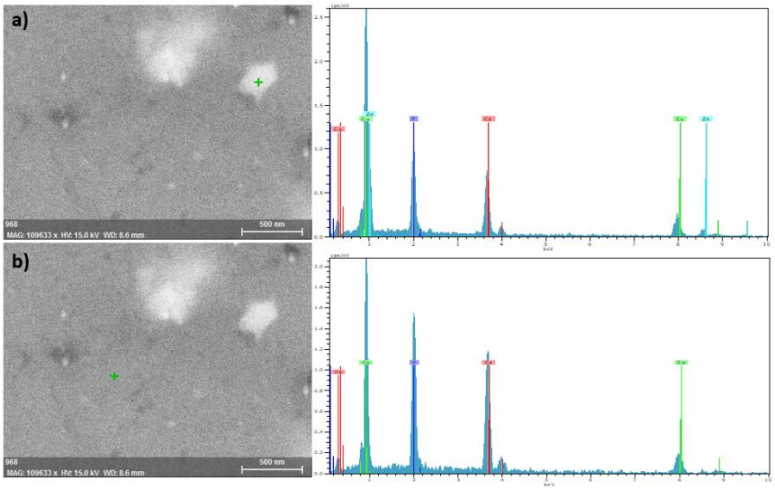


Figure 5.48: SEM image and EDS spectra of sample $Ca_{1.05}Cu_{0.95}P$-$Zn_{0.05}$ Annealing for each element.

In Figure 5.49, SEM images are given after SPS and annealing of the sample synthesized without doping and with increased calcium content by mass. The copper concentration is visible in the light-colored regions of the sample analyzed after SPS and annealing, as shown in the EDS analysis in Figures 5.50 and 5.51. Phosphorus is concentrated in small, dark regions, while calcium, copper, and phosphorus are present in the main structure. Large dark regions are considered to be porous structures.

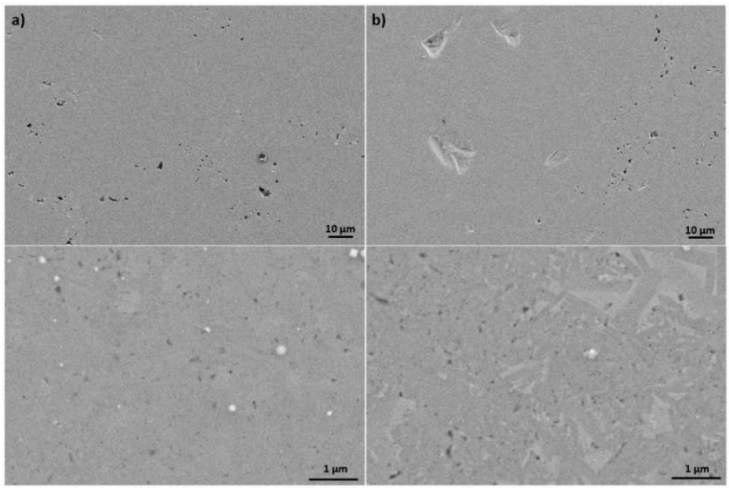


Figure 5.49: SEM images of (a) $Ca_{1.05}CuP$ sample with a magnified image, (b) SEM images of $Ca_{1.05}CuP$ Annealing sample with a magnified image.

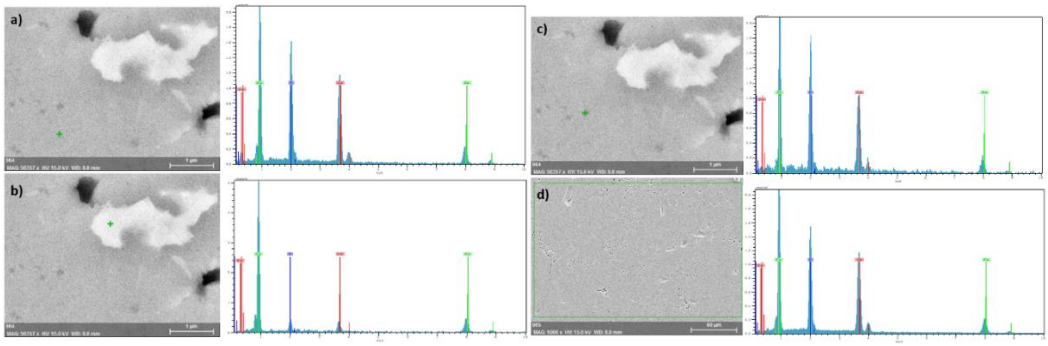


Figure 5.50: SEM image and EDS spectra of sample $Ca_{1.05}CuP$ for each element.

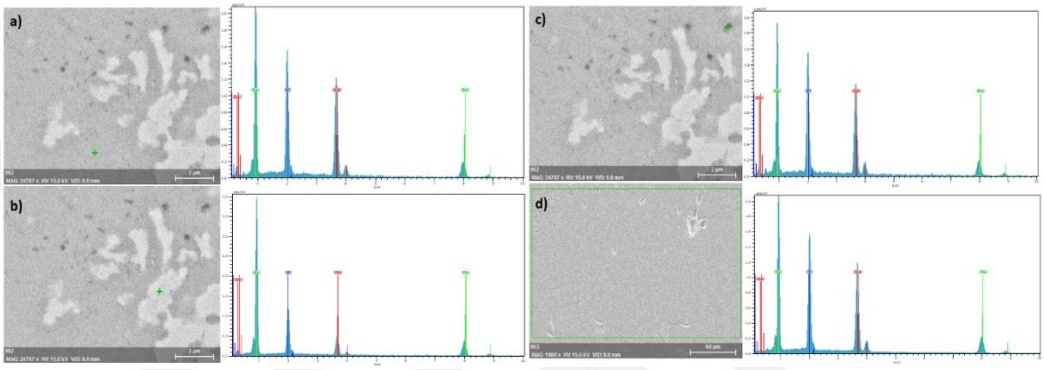


Figure 5.51:. SEM image and EDS spectra of sample $Ca_{1.05}CuP$ Annealing for each element.

### *5.2.4 Transport Property Analysis*

The material's transport properties were measured to calculate the zT values and analyze the thermoelectric efficiency. Figure 5.52 demonstrates the measurements of all thermoelectric characteristics, including doped and undoped CaCuP compounds, up to a temperature of 823 K. As seen in Figure (5.52a), the resistivity values of all samples increase with temperature, which is consistent with the heavily doped semiconducting nature of the material. As a result of doping with different elements, there was a significant increase in the resistivity value. A slightly higher resistivity is seen for doped samples, which shows a decrease in carrier (Hall) mobility, potentially because of impurity phases. Additionally, heat treatment was applied to some compositions to examine the effect of heat treatment on thermoelectric characteristics, as it was suggested by Kanno et al. that increasing grain size can affect thermoelectric properties [64]. As seen in Figure 5.52a, lower electrical resistivity was observed in heat-treated samples. This behavior could be related to the charge transfer that is mainly influenced

by grain boundaries. Grains and grain boundaries behave like different phases in a material. This causes a change in the electronic structure of the material at the grain boundaries, leading to the formation of a potential barrier. As a result, the electrical resistivity increases at the grain boundaries [65]. According to this view, it is expected that the heat treatment result in larger grains and fewer grain boundaries, which would reduce electrical resistivity as confirmed by annealed samples. The Seebeck coefficient is positive in both samples and increases with temperature, indicating that the materials are p-type and the holes play a carrier role. Following the implementation of doping experiments, a significant enhancement in the Seebeck value has been achieved. In addition, changing the intrinsic Ca doping in the compound also showed a positive development in terms of the Seebeck coefficient. As described in Equation 2.5, the Seebeck coefficient increases with the decrease of carrier concentration. Therefore, the increase of Seebeck coefficients can be explained in terms of doping amounts in the structure. While thermal conductivity generally decreases with temperature, only four samples that were doped with La and Zn elements demonstrated a lower conductivity behavior due to alloy scattering. The increase in zT values is seen in the $Ca_{1.05}Cu_{0.95}P$-$Zn_{0.05}$ annealed sample and the $Ca_{1.05}CuP$ sample with which the zT values reach 0.45 and 0.43 at 823 K, respectively. After these two samples, the CaCuP sample has the third highest zT value with a value of 0.37 at 823 K. Considering previous studies published in the literature, the zT value for the CaCuP compound reached 0.5 at 800 K [33]. In a different study by the same author, the CaCuP compound was synthesized in different stoichiometries by the intrinsic doping method, and the best zT value was found to be 0.6 at 873 K and 0.5 at 800 K for the $CaCu_{1.02}P$ compound. In addition, in the same study, the CaCuP compound was synthesized by doping method with the As element in different stoichiometries, but no improvement was observed in zT values, on the contrary, there was a decline [51]. Although the zT values we obtained in our study cannot reach the values in literature studies, we have succeeded in increasing zT by improving the Seebeck value and decreasing thermal conductivity values, thanks to intrinsic and extrinsic doping methods. In general, reducing the intrinsically high concentration of p-type carriers in this specific materials system is challenging. Nevertheless, the analysis indicates that phosphide materials based on CaCuP display significant potential in thermoelectric efficiency.

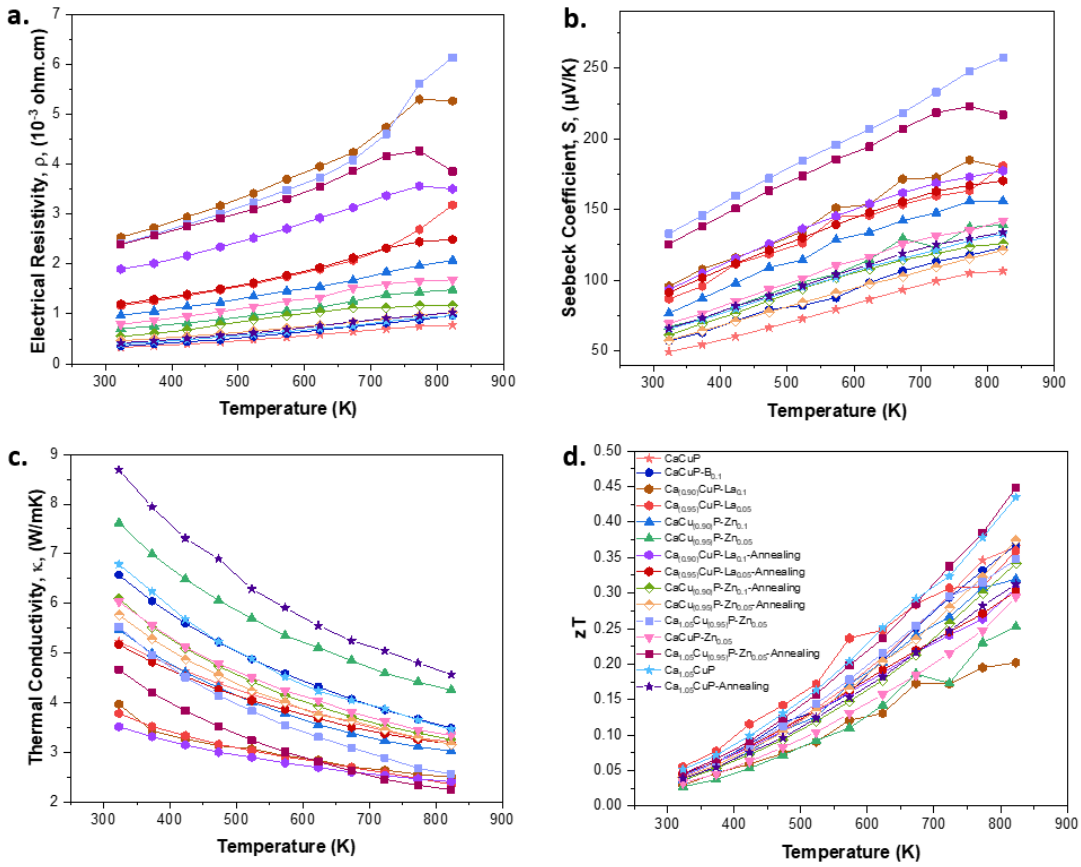


Figure 5.52: a) Electrical Resistivity, b) Seebeck coefficient, c) Thermal conductivity, d) zT values of different dopants of CaCuP samples.

### *5.2.5 Mechanical Property Measurement*

The hardness measurements of the samples synthesized by the internal and external doping methods with various elements were done for CaCuP. The hardness of the materials was measured using the Shimadzu HMV-G Series Micro Vickers Hardness Tester. During the measurement, two different loads were applied to the materials: 0.01 HV (98.07 mN) and 0.025 HV (245.2 mN). The hardness of the materials was determined by measuring 10 different points on all surfaces and calculating the arithmetic mean of these values. The mechanical properties of promising samples in terms of thermoelectric properties were examined. Figures 5.53 and 5.54 indicate the marks and diagonals left by the applied loads on the surface of the samples. Figure 5.55 presents the average Vickers hardness values for undoped, intrinsic doped, and doping samples of CaCuP.

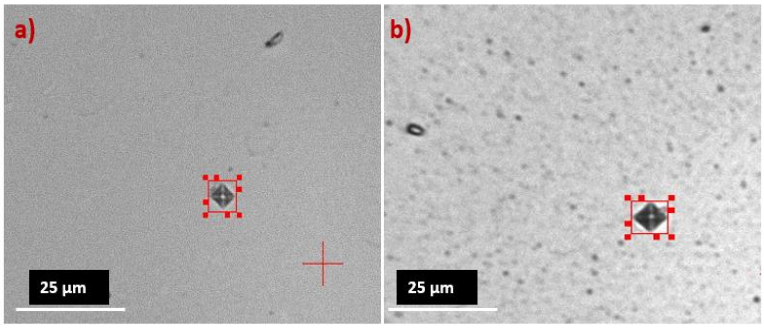


Figure 5.53: Vickers hardness analysis images of a) CaCuP, b) CaCuP-$B_{0.1}$.

The hardness value of CaCuP samples has been observed to be greatly raised by the addition of nanoboron. Upon comparing the hardness values of the synthesized samples, it was found that the Zn-doped $Ca_{1.05}Cu_{0.95}P$-$Zn_{0.05}$ and CaCuP-$Zn_{0.05}$ samples exhibited an increase in hardness. In addition, the hardness values of the other samples are lower than the hardness values of the undoped CaCuP sample. The hardness values cannot be compared to those in the literature because they have not been previously studied. Undoubtedly, the results obtained in this thesis will significantly enhance the utilization of CaCuP in thermoelectric generators due to its high zT values at elevated temperatures and improved mechanical properties.

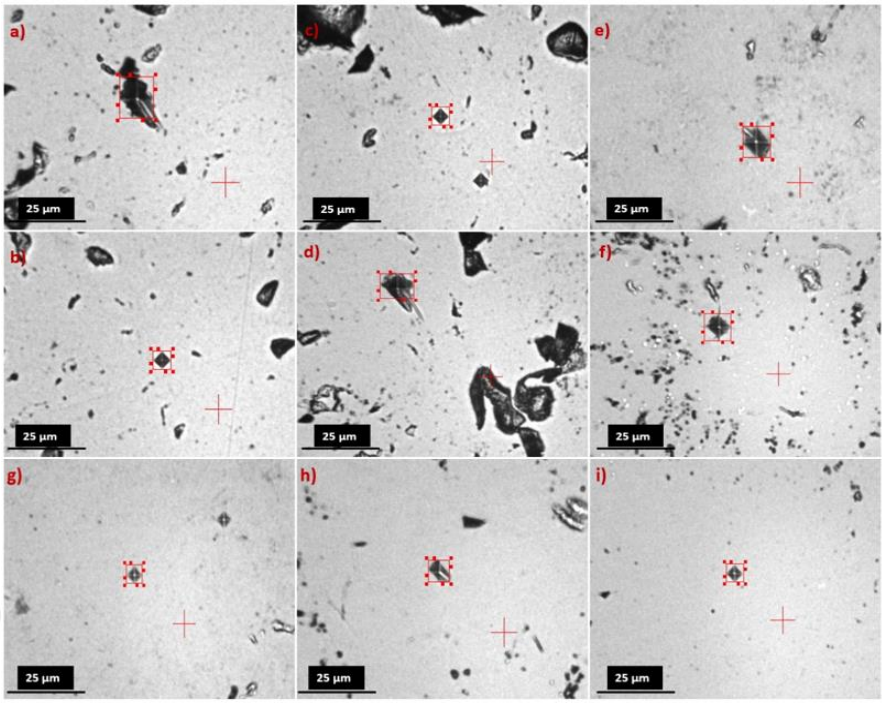


Figure 5.54: Vickers hardness analysis images of a) $Ca_{0.95}CuP\text{-}L_{0.05}$, b) $Ca_{0.95}CuP\text{-}L_{0.05}$ Annealing, c) $CaCu_{0.95}P\text{-}Zn_{0.05}$, d) $CaCu_{0.95}P\text{-}Zn_{0.05}$ Annealing, e) $Ca_{1.05}Cu_{0.95}P\text{-}Zn_{0.05}$, f) $Ca_{1.05}Cu_{0.95}P\text{-}Zn_{0.05}$ Annealing, g) $CaCuP\text{-}Zn_{0.05}$, h) $Ca_{1.05}CuP$, i) $Ca_{1.05}CuP$ Annealing.

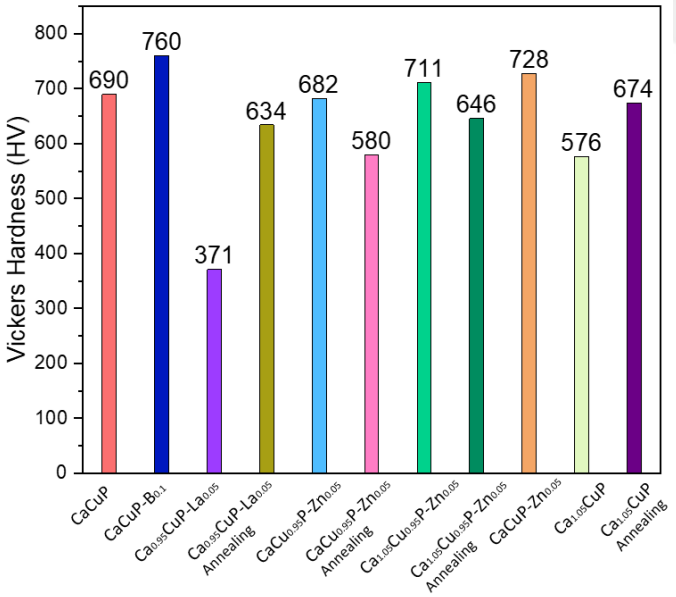


Figure 5.55: Vickers hardness values of CaCuP undoped and doped samples.

## *5.3 Results of Theoretical Calculations*

### *5.3.1 Thermoelectric Modelling Calculations*

Figure 5.56a shows that sample $CaAg_{0.90}P$ has a peak of density-of-states effective mass around 523 K, whereas specimen CaCuP does not. In Figure 5.56b, sample $CaAg_{0.90}P$ has a peculiar increase in nondegenerate mobility as the measurement temperature increases, which means that the interaction between carrier-phonon decreases as the temperature increases. On the other hand, sample CaCuP does not change much with temperature. At temperatures close to room temperature, the nondegenerate mobility of a phosphide thermoelectric material can be predicted to be between 130 and 850 $cm^2/Vs$, which is considered relatively high and both samples are within this value range [30]. Figure 5.56c defines that the weighted mobility of sample CaCuP decreases as the measurement temperature increases. The weighted mobility of most good thermoelectric materials decreases with temperature because electrons are scattered by phonons [21]. In the case of $CaAg_{0.90}P$, there is a peak around 523 K, which means that a theoretical maximum power factor can be implemented at this temperature if carrier concentration is well-tuned.

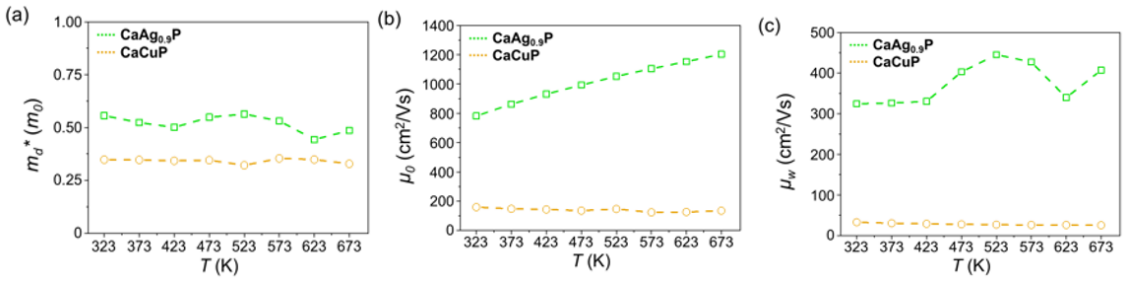


Figure 5.56: a) Temperature dependent-Density-of-states effective mass of $CaAg_{0.90}P$ and CaCuP computed by Single Parabolic Band model, b) Temperature dependent-Nondegenerate mobility of $CaAg_{0.90}P$ and CaCuP computed by Single Parabolic Band model, c) Temperature dependent-Weighted mobility of $CaAg_{0.90}P$ and CaCuP computed by Single Parabolic Band model.

In Figure 5.57c, in the case of lattice thermal conductivity, both specimens show a gradual decrease with temperature, which means that bipolar thermal conductivity due to the influence of bipolar conduction does not affect significantly even if the temperature increases [43]. Figure 5.57d displays that in the case of electronic thermal conductivity,

both specimens remain constant without being greatly affected by the measurement temperature, which is common in other thermoelectric materials.

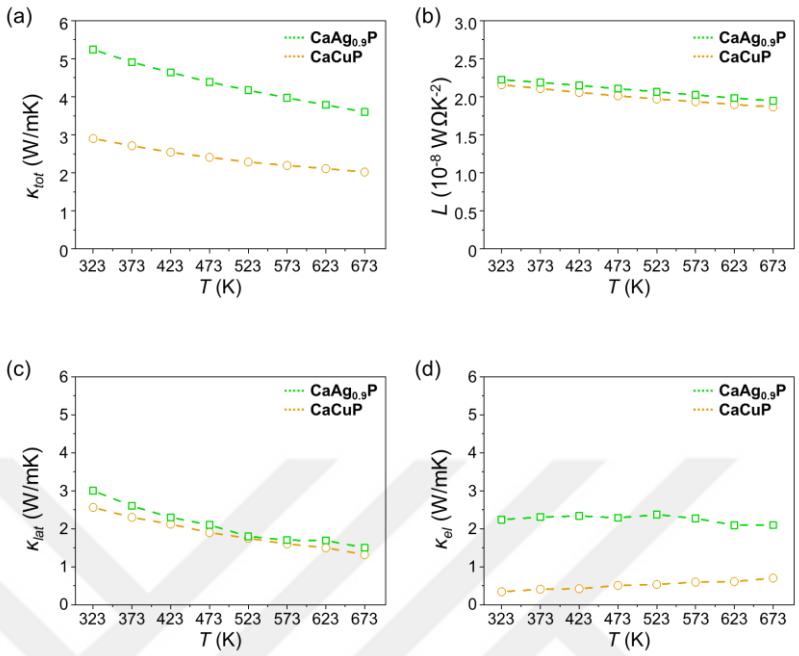


Figure 5.57: (a) Temperature dependent-Thermal conductivity of $CaAg_{0.90}P$ and CaCuP, (b) Temperature dependent-Lorenz number of $CaAg_{0.90}P$ and CaCuP computed by Single Parabolic Band model, (c) Temperature dependent-Lattice thermal conductivity of $CaAg_{0.90}P$ and CaCuP computed by Single Parabolic Band model (Thermal conductivity substitute by electronic thermal conductivity.), (d) Temperature dependent-Electronic thermal conductivity $CaAg_{0.90}P$ and CaCuP computed using Wiedemann-Franz Law ($\kappa_{el} = L\sigma T$).

Figures 5.58 (a-b-c-d) mean that fitting using the SPB model was successful as the pisarenko plot according to the hall carrier concentration matched the theoretically calculated line. In the case of the $CaAg_{0.90}P$ sample, the power factor of 0.33 $mW/mK^2$ at 323 K and power factor of 0.74 $mW/mK^2$ at 673 K can be achieved through carrier concentration tuning. For the CaCuP sample, it was calculated that a power factor of 1.70 $mW/mK^2$ could be achieved at 323 K and a power factor of 1.84 $mW/mK^2$ at 673 K. In both samples, the direction of reducing carrier concentration is the direction of achieving optimal carrier concentration. Figure 5.58 (c-d) represents the Hall mobility of $CaAg_{0.90}P$ and CaCuP with positive values, indicating that the dominated charge carriers were holes. The thermal excitation of conducting carriers causes $n_H$ to increase as the temperature rises slightly for both samples. The Hall mobility value of the CaCuP sample decreases slightly with increasing temperature, implying that the main scattering sources were

acoustic phonons [66]. While the value is less than 100 $cm^2V^{-1}s^{-1}$ for $CaAg_{0.90}P$ at room temperature, it is greater than 100 $cm^2V^{-1}s^{-1}$ for CaCuP. This value is larger than that of a normal metal such as Na and Cu, which is ~50 $cm^2V^{-1}s^{-1}$ at room temperature but is much smaller than that of Dirac semimetals such as $Cd_3As_2$. Electron scattering in the polycrystalline sample at grain boundaries is most likely the cause [45].

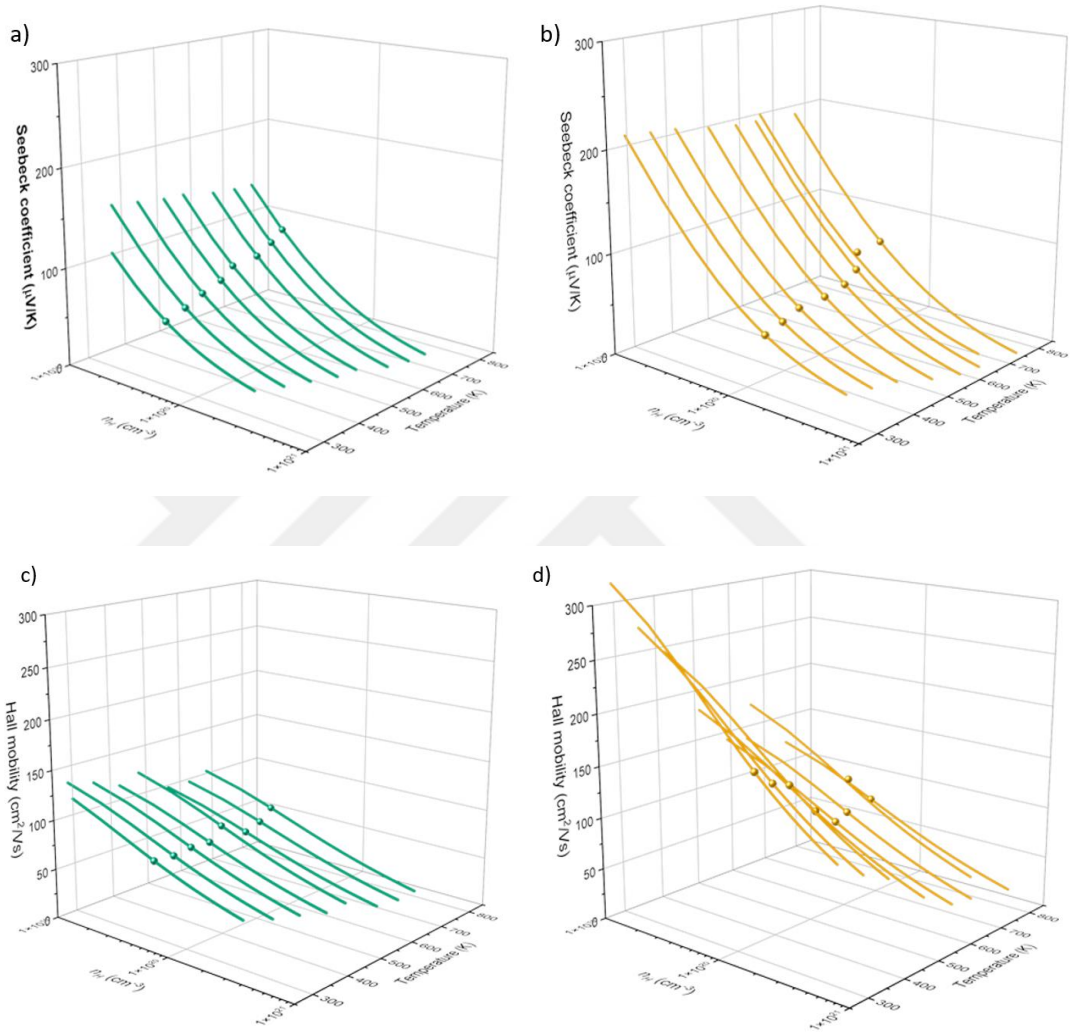

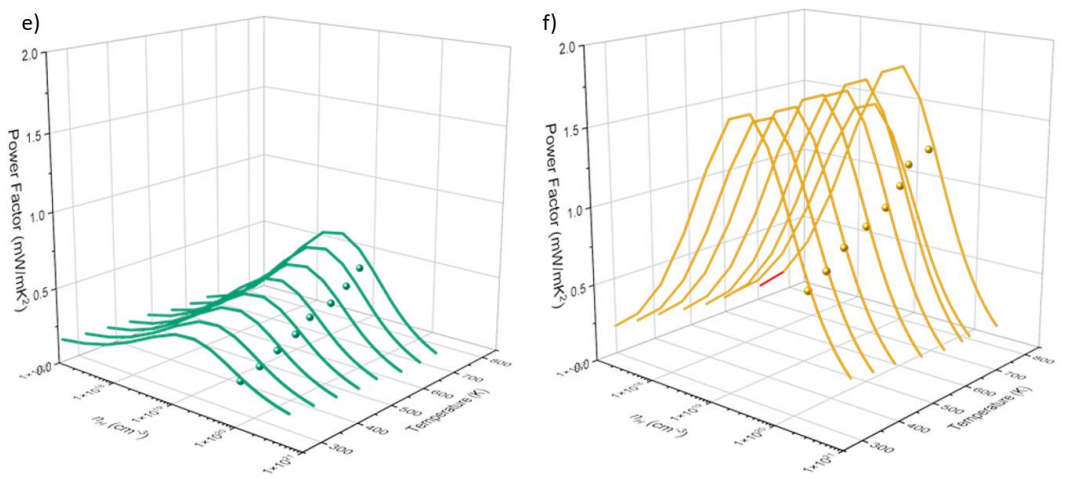


Figure 5.58: (a) Temperature-Seebeck pisarenko 3D plot of $CaAg_{0.90}P$ (Experimentally measured value of green round symbol and theoretically computed value of green line using Single Parabolic Band model), (b) Temperature-Seebeck pisarenko 3D plot of CaCuP (Experimentally measured value of orange round symbol and theoretically computed value of orange line using Single Parabolic Band model), (c) Mobility pisarenko plot of $CaAg_{0.90}P$ (Experimentally measured value of green round symbol and theoretically computed value of green line using Single Parabolic Band model), (d) Mobility pisarenko plot of CaCuP (Experimentally measured value of orange round symbol and theoretically computed value of orange line using Single Parabolic Band model), (e) Hall carrier concentration-Temperature-Power Factor 3D plot of $CaAg_{0.90}P$ (Experimentally measured value of green round symbol and theoretically computed value of green line using Single Parabolic Band model), (f) Hall carrier concentration-Temperature-Power Factor 3D plot of CaCuP (Experimentally measured value of orange round symbol and theoretically computed value of orange line using Single Parabolic Band model).

Figure 5.59a describes that the B-factor is a parameter that is proportional to the theoretically achievable maximum zT, and since both samples exhibit a B-factor that increases with temperature, it means that the theoretically achievable zT increases with temperature. Additionally, PbTe, one of the most traditional thermoelectric materials, has a B value of 0.7 at 800 Kelvin [67]. Although the CaAgP and CaCuP materials obtained in this study do not have values very close to these, they are still promising in terms of commercialization. These phenomena are also shown in Figures 5.60b and 5.60c. In the case of the $CaAg_{0.90}P$ sample, zT of 0.04 at 323 K and zT of 0.33 at 673 K can be achieved through carrier concentration tuning (For 323 K, hall carrier concentration of $8.20 \times 10^{18}$ and for 673 K, $1.07 \times 10^{19}$). For the CaCuP sample, it was calculated that zT of 0.17 at 323 K and zT of 0.61 at 673 K can be achieved through carrier concentration tuning (For 323 K, hall carrier concentration of $7.83 \times 10^{18}$, for 673K, $1.92 \times 10^{19}$). The

theoretically calculated maximum zT of $CaAg_{0.90}P$ and CaCuP samples are 0.33 and 0.61, respectively, compared to 0.189 and 0.252 at 673 K, which is a maximum increase of 240%.

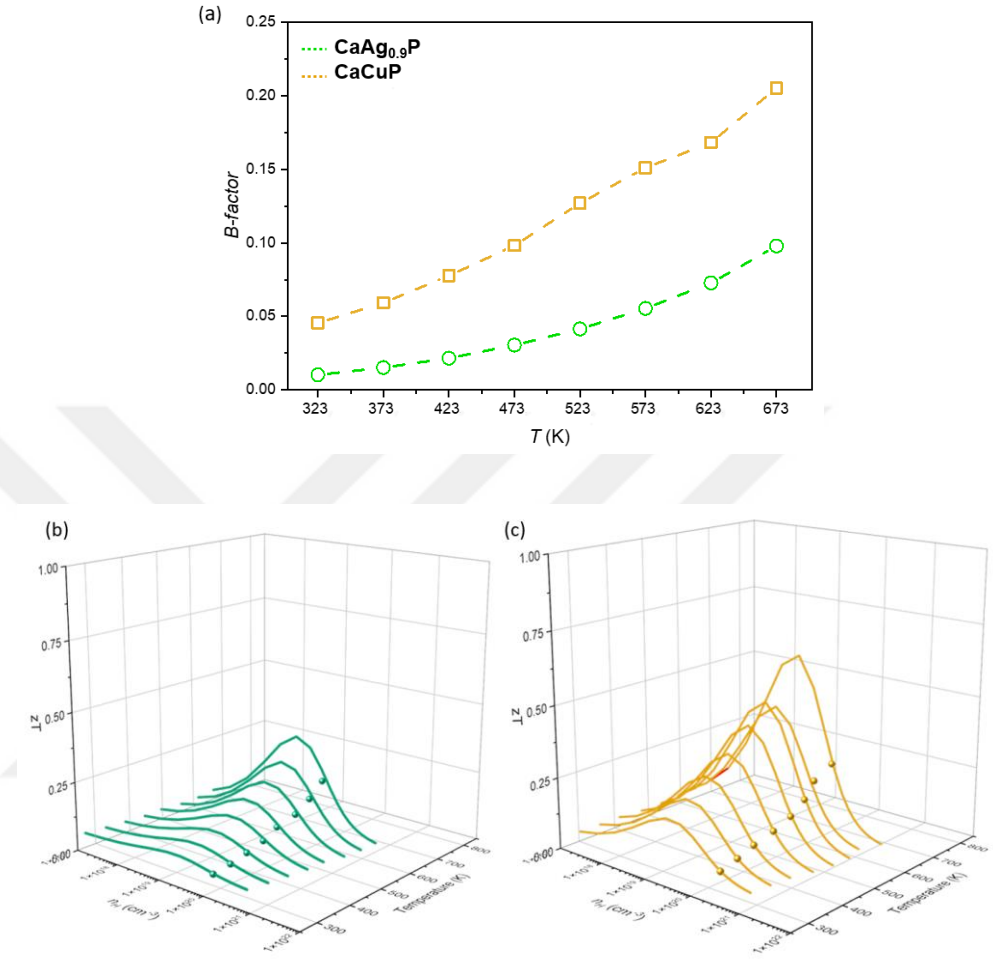


Figure 5.59: (a) Temperature-dependent B-factor of $CaAg_{0.90}P$ and CaCuP, (b) Hall carrier concentration-Temperature-zT 3D plot of $CaAg_{0.90}P$ (Experimentally measured value of green round symbol and theoretically computed value of green line using Single Parabolic Band model), (c) Hall carrier concentration-Temperature-zT 3D plot of CaCuP (Experimentally measured value of orange round symbol and theoretically computed value of orange line using Single Parabolic Band model).

### *5.3.2 Band Factors and Dielectric Constant Measurements*

In this part, band factors including the DOS effective mass, estimation of zT values, thermoelectric properties, and the dielectric constant of undoped CaAgP and CaCuP samples, as well as CaAgP samples doped with three different elements, were measured. Detailed graphs of these calculations are given below. Band factors such as density-of-

states effective mass, non-degenerate mobility, weighted mobility, and B-factor are shown in Figure 5.60.

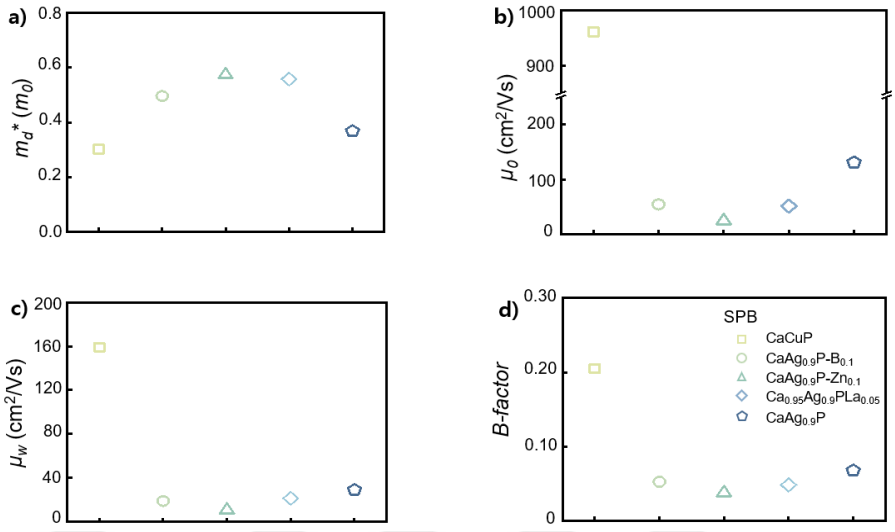


Figure 5.60: Ternary phosphides CaCuP, $CaAg_{0.90}P$, $CaAg_{0.90}P$-$B_{0.1}$, $CaAg_{0.90}P$-$Zn_{0.1}$, $Ca_{0.95}Ag_{0.90}P$-$La_{0.05}$ a) Density-of-states effective mass, b) Non-degenerate mobility, c) Weighted mobility, and d) B-factor.

The theoretical thermoelectric performance (S, σ, $S^2\sigma$, zT) according to the $n_H$ of the composition calculated based on the above band factors is shown in Figure 5.61. Based on Figures 5.60 and 5.61, it can be seen that the theoretically derived zT of CaCuP can be about 4 to 5 times higher than that of CaAgP at 300 K and that the $n_H$ must be reduced to about $10^{18}$ to $10^{19}$ $cm^{-3}$ to derive the maximum zT.

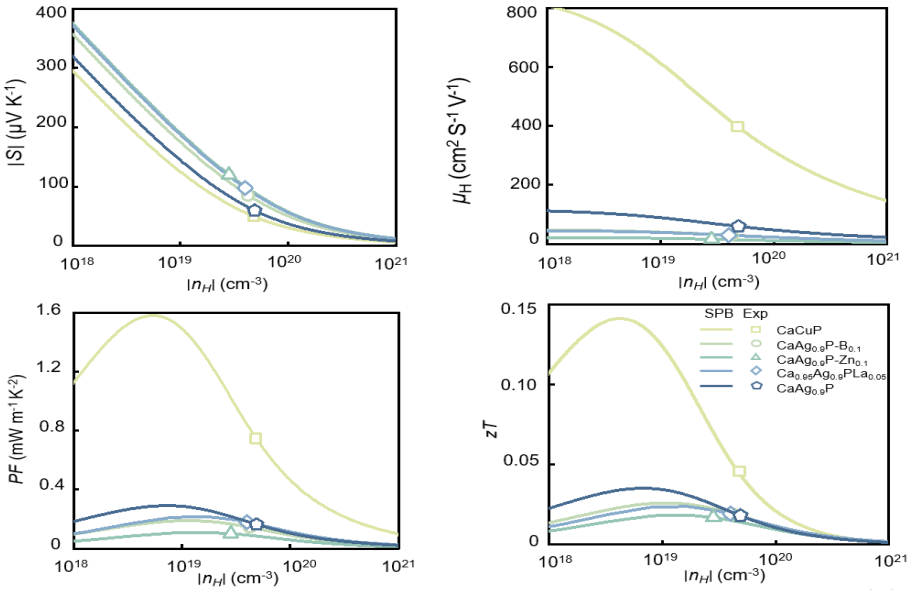


Figure 5.61: $n_H$ dependent theoretical thermoelectric performance of ternary phosphides CaCuP, $CaAg_{0.90}P$, $CaAg_{0.90}P\text{-}B_{0.1}$, $CaAg_{0.90}P\text{-}Zn_{0.1}$, $Ca_{0.95}Ag_{0.90}P\text{-}La_{0.05}$.

Figure 5.62 shows the total thermal conductivity, Lorenz number, thermal conductivity electron contribution, and thermal conductivity lattice contributions according to the temperature of the ternary phosphide CaCuP, $CaAg_{0.90}P$, $CaAg_{0.90}P\text{-}B_{0.1}$, $CaAg_{0.90}P\text{-}Zn_{0.1}$, and $Ca_{0.95}Ag_{0.90}P\text{-}La_{0.05}$. All compositions decreased the overall thermal conductivity as the temperature increased. In the case of CaCuP, the electromagnetic filtration of the thermal conductivity did not change significantly even when the temperature increased.

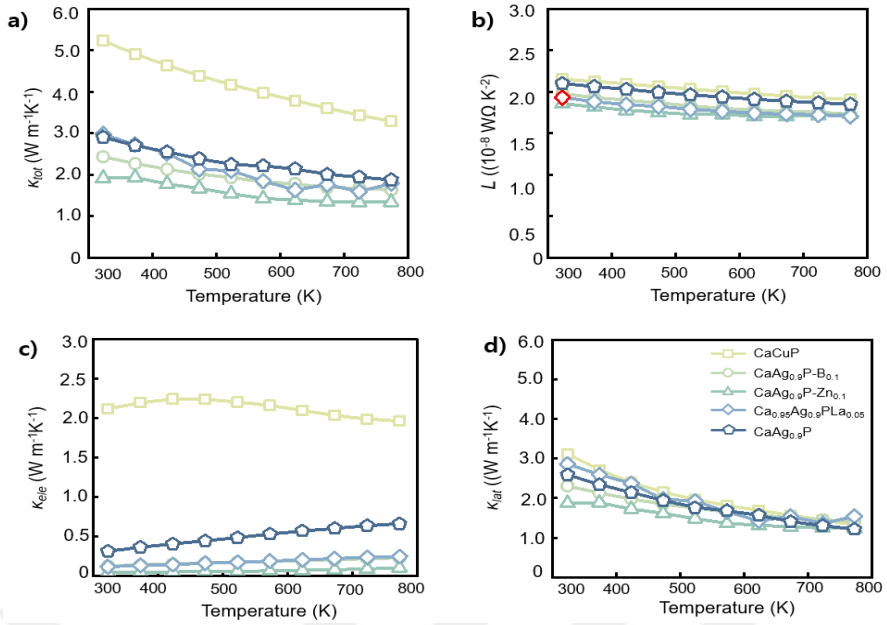


Figure 5.62: Ternary phosphides CaCuP, $CaAg_{0.90}P$, $CaAg_{0.90}P\text{-}B_{0.1}$, $CaAg_{0.90}P\text{-}Zn_{0.1}$, $Ca_{0.95}Ag_{0.90}P\text{-}La_{0.05}$ a) Total thermal conductivity (κ), b) Lorenz number (L), c) Thermal conductivity electromagnetic filtration ($\kappa_{ele}$), d) Thermal conductivity lattice contribution ($\kappa_{lat}$).

The permittivity of a substance represented as a ratio with the electric permittivity of a vacuum is known as the relative permittivity or dielectric constant. A dielectric is a material that does not conduct electricity, and the dielectric constant of an insulator measures its capacity to store electrical energy in an electric field. It depends on the wavelength of the light [68]. To look into the physical connection between thermoelectric and dielectric properties, the impedance of the five samples in Figure 5.62 was used to measure their dielectric constant. Figure 5.63 shows the dielectric constant that was found by dividing the band factor $\mu_0$ by $\kappa_{lat}$ ($\mu_0/\kappa_{lat}$). The dielectric constant decreases as $\mu_0/\kappa_{lat}$ increases in all ternary phosphide compositions. This is the fact that the lattice contribution between electron-phonon interactions and thermal conductivity decreases; that is, the dielectric constant decreases as the thermoelectric performance becomes excellent. This physical relationship has been proposed but has not been experimentally identified, proving that a relatively simple measurement of the dielectric constant can be used to increase thermoelectric performance in the design of thermoelectric materials.

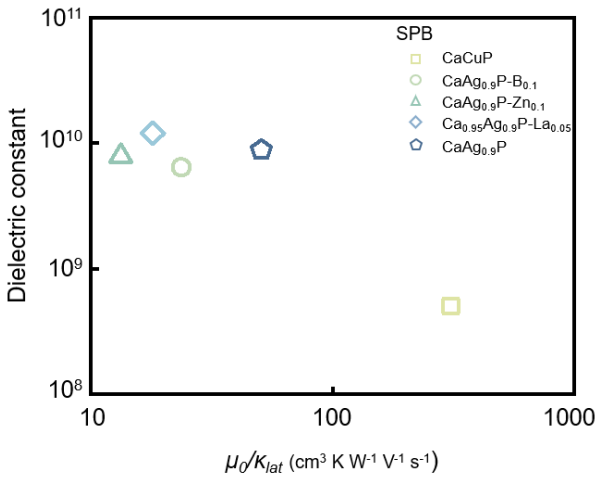


Figure 5.63: The dielectric constant of CaCuP, $CaAg_{0.90}P$, $CaAg_{0.90}P\text{-}B_{0.1}$, $CaAg_{0.90}P\text{-}Zn_{0.1}$, $Ca_{0.95}Ag_{0.90}P\text{-}La_{0.05}$.

# Chapter 6:
# CONCLUSION

The thesis researched the thermoelectric properties of ternary phase phosphides, which were found to be promising thermoelectrical materials by the high-throughput computational screening of the electronic properties [30]. CaAgP ternary phosphide material has attracted attention due to its band structure [46]. In polycrystalline thin films, CaCuP has attracted some interest as a promising transparent optical conductor with good Hall mobilities, $\mu_H$, ~45 $cm^2\ V^{-1}\ s^{-1}$ at 300 K [69]. In addition, it has the most excellent electrical characteristics of this class of materials, with the highest recorded power factors ($\alpha^2\sigma$) [33]. Thus the thesis focused on synthesizing stable phosphides of CaAgP and CaCuP materials. This was achieved by utilizing high-energy ball-milling and SPS techniques to optimize stoichiometry, determine the processing methods, and adjust the parameters of the high-energy ball-milling process time and SPS parameters. The main objective is to produce stable powders and pellets. After samples were synthesized successfully, to examine the effect of doping elements on thermoelectric properties, both groups of materials were doped with various elements such as La, Zn, Sn, B, and Na. Furthermore, intrinsic doping was achieved by altering the quantities of the fundamental elements in the material according to stoichiometric ratios, and the resulting impacts were analyzed.

Although the La-doped sample excelled the undoped sample in terms of zT values over a wide temperature range, the $CaAg_{0.90}P$ sample, which was doped intrinsically, exhibited the greatest zT value of around 0.33 at a temperature of 823 K. The doped CaAgP samples exhibited high electrical resistivity. To solve this issue, the annealing process was applied to reduce the electrical resistivity by introducing grain growth and reducing grain boundary densities. All Seebeck values exhibit positive values, indicating a p-type nature, and demonstrate a rising trend with increasing temperature. On the other hand, the addition of boron, zinc, and lanthanum caused a decrease in the thermal conductivity of the samples without affecting their carrier concentration. Whereas significant alterations to the zT values of CaAgP samples were not applicable, it was important to examine the impact of doping elements on the electrical resistivity, Seebeck coefficient, and thermal conductivity values. Significant improvements in terms of thermoelectric parameters have been achieved for the CaCuP material. As a result of

studies on CaCuP, the highest zT value of 0.37 was increased to 0.45 at 823 Kelvin for the material that was doped with 0.05 at. % Zn and annealed, thus increasing the thermoelectric performance coefficient by 24%. Furthermore, due to the stoichiometric increase in the amount of Ca in the $Ca_{1.05}CuP$ sample, the zT value achieved one of the highest values recorded at a temperature of 823 K, becoming a value of 0.43. The CaCuP samples demonstrated a substantial improvement in zT values, Seebeck coefficients, and thermal conductivity values. When the mechanical properties were examined, it was seen that the mechanical properties were improved by adding 0.05 nano boron at a stoichiometric ratio for CaAgP compounds. In CaCuP compounds, an examination of the mechanical properties showed that the addition of nanoboron and zinc at a stoichiometric ratio resulted in their mechanical enhancement.

It should be emphasized that the detailed experimental studies carried out for ternary phosphides, supported by computational methods, contributed greatly to the success of our studies. The studies' experimental and theoretical research has significantly contributed to the development of final products in the field of thermoelectric materials. In addition, the electronic properties of materials obtained at high temperatures using SPB modeling with the contributions of the South Korean team allowed us to model electronic transport using equations that are solutions of the Boltzmann transport equations. Based on Hall carrier concentration data, the effective mass of DOS was estimated. The theoretical zT value as a function of Hall carrier concentration was obtained from the calculated DOS effective mass, band factors, and measured lattice thermal conductivity. This information will be useful in future studies to develop strategies to further optimize the thermoelectric properties of the studied phases in terms of Hall carrier concentration. As we have shown in this research, in the future, it is aimed to use thermoelectrically optimized materials with improved mechanical properties in the production of modules with high commercialization potential.

# BIBLIOGRAPHY

1. Rull-Bravo, M., et al., *Skutterudites as thermoelectric materials: revisited.* Rsc Advances, 2015. **5**(52): p. 41653-41667.

2. Twaha, S., et al., A comprehensive review of thermoelectric technology: Materials, applications, modelling and performance improvement. Renewable and sustainable energy reviews, 2016. **65**: p. 698-726.

3. Freer, R. and A.V. Powell, *Realising the potential of thermoelectric technology: A Roadmap.* Journal of Materials Chemistry C, 2020. **8**(2): p. 441-463.

4. Snyder, G.J. and A.H. Snyder, *Figure of merit ZT of a thermoelectric device defined from materials properties.* Energy & Environmental Science, 2017. **10**(11): p. 2280-2283.

5. He, J. and T.M. Tritt, Advances in thermoelectric materials research: Looking back and moving forward. Science, 2017. **357**(6358): p. eaak9997.

6. Papapetrou, M., et al., Industrial waste heat: Estimation of the technically available resource in the EU per industrial sector, temperature level and country. Applied Thermal Engineering, 2018. **138**: p. 207-216.

7. Snyder, G.J. and E.S. Toberer, *Complex thermoelectric materials.* Nature materials, 2008. **7**(2): p. 105-114.

8. Constantinescu, G., et al., Prospects for electrical performance tuning in Ca3Co4O9 materials by metallic Fe and Ni particles additions. Materials, 2021. **14**(4): p. 980.

9. Shi, X., L. Chen, and C. Uher, *Recent advances in high-performance bulk thermoelectric materials.* International Materials Reviews, 2016. **61**(6): p. 379-415.

10. Elsheikh, M.H., et al., A review on thermoelectric renewable energy: Principle parameters that affect their performance. Renewable and sustainable energy reviews, 2014. **30**: p. 337-355.

11. Ge, Z.-H., et al., Low-cost, abundant binary sulfides as promising thermoelectric materials. Materials Today, 2016. **19**(4): p. 227-239.

12. Tritt, T.M., Thermoelectric materials: Principles, structure, properties, and applications. 2002.

13. Vaqueiro, P. and A.V. Powell, *Recent developments in nanostructured materials for high-performance thermoelectrics.* Journal of Materials Chemistry, 2010. **20**(43): p. 9577-9584.

14. Szczech, J.R., J.M. Higgins, and S. Jin, *Enhancement of the thermoelectric properties in nanoscale and nanostructured materials.* Journal of Materials Chemistry, 2011. **21**(12): p. 4037-4055.

15. DiSalvo, F.J., *Thermoelectric cooling and power generation.* Science, 1999. **285**(5428): p. 703-706.

16. Bux, S.K., J.-P. Fleurial, and R.B. Kaner, *Nanostructured materials for thermoelectric applications.* Chemical Communications, 2010. **46**(44): p. 8311-8324.

17. Kim, H.S., et al., *Relationship between thermoelectric figure of merit and energy conversion efficiency.* Proceedings of the National Academy of Sciences, 2015. **112**(27): p. 8205-8210.

18. Fleurial, J.-P., Thermoelectric power generation materials: Technology and application opportunities. Jom, 2009. **61**(4): p. 79-85.

19. Zhang, X., et al., *Electronic quality factor for thermoelectrics.* Science advances, 2020. **6**(46): p. eabc0726.

20. Pei, Y., H. Wang, and G.J. Snyder, *Band engineering of thermoelectric materials.* Advanced materials, 2012. **24**(46): p. 6125-6135.

21. Snyder, G.J., et al., *Weighted mobility.* Advanced Materials, 2020. **32**(25): p. 2001537.

22. Han, C., Z. Li, and S. Dou, *Recent progress in thermoelectric materials.* Chinese science bulletin, 2014. **59**: p. 2073-2091.

23. Abdel-Motaleb, I.M. and S.M. Qadri, *Thermoelectric devices: principles and future trends.* arXiv preprint arXiv:1704.07742, 2017.

24. Minnich, A., et al., Bulk nanostructured thermoelectric materials: current research and future prospects. Energy & Environmental Science, 2009. **2**(5): p. 466-479.

25. Zhang, X. and L.-D. Zhao, *Thermoelectric materials: Energy conversion between heat and electricity.* Journal of Materiomics, 2015. **1**(2): p. 92-105.

26. Sootsman, J.R., D.Y. Chung, and M.G. Kanatzidis, *New and old concepts in thermoelectric materials.* Angewandte Chemie International Edition, 2009. **48**(46): p. 8616-8639.

27. Chen, Z.-G., et al., *Nanostructured thermoelectric materials: Current research and future challenge.* Progress in Natural Science: Materials International, 2012. **22**(6): p. 535-549.

28. Li, S.S. and S.S. Li, *Scattering mechanisms and carrier mobilities in semiconductors.* Semiconductor Physical Electronics, 1993: p. 183-211.

29. Corbridge, D.E.C., Phosphorus: chemistry, biochemistry and technology. 2013: CRC press.

30. Pöhls, J.-H., et al., *Metal phosphides as potential thermoelectric materials.* Journal of Materials Chemistry C, 2017. **5**(47): p. 12441-12456.

31. Quinn, R.J. and J.-W.G. Bos, *Recent progress in phosphide materials for thermoelectric conversion.* Journal of Materials Chemistry A, 2023. **11**(16): p. 8453-8469.

32. Earnshaw, A. and N.N. Greenwood, *Chemistry of the Elements*. Vol. 60. 1997: Butterworth-Heinemann Oxford.

33. Quinn, R.J., et al., *New sustainable ternary copper phosphide thermoelectrics.* Chemical Communications, 2022. **58**(84): p. 11811-11814.

34. Djied, A., et al., Structural phase transition, mechanical and optoelectronic properties of the tetragonal NaZnP: Ab-initio study. Computational materials science, 2014. **84**: p. 396-403.

35. Martinez, A.D., et al., *Solar energy conversion properties and defect physics of ZnSiP 2.* Energy & Environmental Science, 2016. **9**(3): p. 1031-1041.

36. Watcharapasorn, A., et al., *Preparation and thermoelectric properties of some phosphide skutterudite compounds.* Journal of Applied Physics, 1999. **86**(11): p. 6213-6217.

37. Zaikina, J.V., et al., *Highly disordered crystal structure and thermoelectric properties of Sn3P4.* Chemistry of Materials, 2008. **20**(7): p. 2476-2483.

38. Zhang, J., et al., *High thermoelectric performance can be achieved in black phosphorus.* Journal of Materials Chemistry C, 2016. **4**(5): p. 991-998.

39. Yi, T., et al., Phase characterization, thermal stability, high-temperature transport properties, and electronic structure of rare-earth Zintl phosphides Eu3M2P4 (M= Ga, In). Inorganic chemistry, 2013. **52**(7): p. 3787-3794.

40. Dolyniuk, J.-A., et al., Twisted Kelvin cells and truncated octahedral cages in the crystal structures of unconventional clathrates, AM2P4 (A= Sr, Ba; M= Cu, Ni). Chemistry of Materials, 2015. **27**(12): p. 4476-4484.

41. Zaikina, J.V., et al., Bulk and Surface Structure and High-Temperature Thermoelectric Properties of Inverse Clathrate-III in the Si-P-Te System. Chemistry–A European Journal, 2010. **16**(42): p. 12582-12589.

42. Nuss, J.r., et al., Phosphide–tetrahedrite Ag6Ge10P12: thermoelectric performance of a long-forgotten silver-cluster compound. Chemistry of Materials, 2017. **29**(16): p. 6956-6965.

43. Quinn, R.J. and J.-W.G. Bos, Promising thermoelectric performance in CaAgP with intrinsic Ag vacancies. Applied Physics Letters, 2022. **120**(7).

44. Mewis, A., CaAgP und CaAgAs-Zwei Verbindungen mit Fe2P-Struktur/CaAgP and CaAgAs-Two Compounds with the Fe2P-Structure. Zeitschrift für Naturforschung B, 1979. **34**(1): p. 14-17.

45. Okamoto, Y., et al., Low Carrier Density Metal Realized in Candidate Line-Node Dirac Semimetals CaAgP and CaAgAs. Journal of the Physical Society of Japan, 2016. **85**: p. 123701.

46. Xu, N., et al., Trivial topological phase of CaAgP and the topological nodal-line transition in CaAg (P 1− x A s x). Physical Review B, 2018. **97**(16): p. 161111.

47. Jong, U.-G., et al., Theoretical insight into potential thermoelectric performance of ternary metal phosphide CaAgP. Applied Physics Letters, 2023. **122**(13).

48. Dhawan, R., et al., *Electronic and Thermoelectric Transport Properties of CaAgP from First Principles.* The Journal of Physical Chemistry C, 2023. **127**(23): p. 10922-10928.

49. Mewis, A., ABX-Verbindungen mit Ni2In-Struktur Darstellung und Struktur der Verbindungen CaCuP (As), SrCuP (As), SrAgP (As) und EuCuAs/ABX Compounds with the Structure Ni2In Preparation and Crystal Structure of CaCuP (As), SrCuP (As), SrAgP (As), and EuCuAs. Zeitschrift für Naturforschung B, 1978. **33**(9): p. 983-986.

50. Williamson, B.A., et al., *Engineering valence band dispersion for high mobility p-type semiconductors.* Chemistry of Materials, 2017. **29**(6): p. 2402-2413.

51. Quinn, R.J., R. Biswas, and J.-W.G. Bos, *Alloying and doping control in the layered metal phosphide thermoelectric CaCuP.* ACS Applied Electronic Materials, 2023.

52. Han, F., et al., Quantized thermoelectric Hall effect induces giant power factor in a topological semimetal. Nature communications, 2020. **11**(1): p. 6167.

53. Zolriasatein, A., et al., Comparative study of SPEX and planetary milling methods for the fabrication of complex metallic alloy nanoparticles. Micro & Nano Letters, 2018. **13**(4): p. 448-451.

54. Guillon, O., et al., Field-assisted sintering technology/spark plasma sintering: mechanisms, materials, and technology developments. Advanced Engineering Materials, 2014. **16**(7): p. 830-849.

55. Suárez, M., et al., Challenges and opportunities for spark plasma sintering: a key technology for a new generation of materials. Sintering applications, 2013. **13**: p. 319-342.

56. Cavaliere, P., Spark plasma sintering of materials: advances in processing and applications. 2019: Springer.

57. Epp, J., X-ray diffraction (XRD) techniques for materials characterization, in Materials characterization using nondestructive evaluation (NDE) methods. 2016, Elsevier. p. 81-124.

58. Vernon-Parry, K.D., *Scanning electron microscopy: an introduction.* III-Vs review, 2000. **13**(4): p. 40-44.

59. Inkson, B.J., Scanning electron microscopy (SEM) and transmission electron microscopy (TEM) for materials characterization, in Materials characterization using nondestructive evaluation (NDE) methods. 2016, Elsevier. p. 17-43.

60. Abdullah, A. and A. Mohammed. Scanning electron microscopy (SEM): A review. in Proceedings of 2018 International Conference on Hydraulics and Pneumatics-HERVEX. 2019. Băile Govora Romania.

61. Kim, W., *Strategies for engineering phonon transport in thermoelectrics.* Journal of Materials Chemistry C, 2015. **3**(40): p. 10336-10348.

62. Ma, Z., et al., *Review of experimental approaches for improving zT of thermoelectric materials.* Materials Science in Semiconductor Processing, 2021. **121**: p. 105303.

63. Wang, X., Y. Yang, and L. Zhu, Effect of grain sizes and shapes on phonon thermal conductivity of bulk thermoelectric materials. Journal of Applied Physics, 2011. **110**(2).

64. Kanno, T., et al., Enhancement of average thermoelectric figure of merit by increasing the grain-size of Mg3. 2Sb1. 5Bi0. 49Te0. 01. Applied Physics Letters, 2018. **112**(3).

65. Kuo, J.J., et al., *Grain boundary dominated charge transport in Mg 3 Sb 2-based compounds.* Energy & Environmental Science, 2018. **11**(2): p. 429-434.

66. Toberer, E.S., A. Zevalkink, and G.J. Snyder, *Phonon engineering through crystal chemistry.* Journal of Materials Chemistry, 2011. **21**(40): p. 15843-15852.

67. Wang, H., et al., *Material design considerations based on thermoelectric quality factor.* Thermoelectric Nanomaterials: Materials Design and Applications, 2013: p. 3-32.

68. Mistrik, J., et al., *Optical properties of electronic materials: fundamentals and characterization.* Springer handbook of electronic and photonic materials, 2017: p. 1-1.

69. Willis, J., et al., Prediction and realisation of high mobility and degenerate p-type conductivity in CaCuP thin films. Chemical Science, 2022. **13**(20): p. 5872-5883.